MONTE CARLO MODELING OF CARRIER DYNAMICS IN PHOTOCONDUCTIVE TERAHERTZ SOURCES

A Dissertation
Presented to
The Academic Faculty

by

Dae Sin Kim

In Partial Fulfillment
of the Requirements for the Degree
Doctor of Philosophy in the
School of Electrical and Computer Engineering

Georgia Institute of Technology
August 2006

MONTE CARLO MODELING OF CARRIER DYNAMICS IN PHOTOCONDUCTIVE TERAHERTZ SOURCES

Approved by:

Dr. David S. Citrin, Advisor
School of Electrical and Computer Engineering
Georgia Institute of Technology

Dr. Shyh-Chiang Shen
School of Electrical and Computer Engineering
Georgia Institute of Technology

Dr. Stephen E. Ralph
School of Electrical and Computer Engineering
Georgia Institute of Technology

Dr. Douglas R. Denison
Signature Technology Laboratory
Georgia Tech Research Institute

Dr. Gregory D. Durgin
School of Electrical and Computer Engineering
Georgia Institute of Technology

Date Approved: May 31, 2006

ACKNOWLEDGEMENTS

I am deeply indebted to my advisor, Dr. David S. Citrin, for giving me the opportunity to work in this area, for his precious advice, continuous encouragement and full support, for the time and energy he devoted in discussing my research.

I am also very grateful to Drs. Stephen E. Ralph and Douglas R. Denison for their assistance and valuable discussion in my research and for serving on my committee. I would like to express my sincere appreciation to Drs. Gregory D. Durgin and Shyh-Chiang Shen for their kindness and willingness to serve on my committee. I would also like to extend my sincere thanks to all our group members who have helped me.

Finally, I would like to thank my wife, Eun Ae Lee and my son, Sehyun Kim, most heartily for their patience, encouragement, and understanding during the course of this work.

TABLE OF CONTENTS

LIST OF TABLES

LIST OF FIGURES

SUMMARY

Carrier dynamics in GaAs-based photoconductive terahertz (THz) sources is investigated using Monte Carlo techniques to optimize the emitted THz transients. A self-consistent Monte Carlo-Poisson solver is developed for the spatio-temporal carrier transport properties. The screening contributions to the THz radiation associated with the Coulomb and radiation fields are obtained self-consistently by incorporating the three-dimensional Maxwell equations into the solver. In addition, the enhancement of THz emission by a large trap-enhance field (TEF) near the anode in semi-insulating (SI) photoconductors is investigated.

The transport properties of the photoexcited carriers in photoconductive THz sources depend markedly on the initial spatial distribution of those carriers. Thus, considerable control of the emitted THz spectrum can be attained by judiciously choosing the optical excitation spot shape on the photoconductor, since the carrier dynamics that provide the source of the THz radiation are strongly affected by the ensuing screenings. The screening contributions due to the Coulomb and radiation parts of the electromagnetic field acting back on the carrier dynamics are distinguished. The dominant component of the screening field crosses over at an excitation aperture size with full width at half maximum (FWHM) of ~100 μm for a range of reasonable excitation levels. In addition, the key mechanisms responsible for the TEF near the anode of SI photoconductors are elucidated in detail. For a given optical excitation power, an enhancement of THz radiation power can be obtained using a maximally broadened

excitation aperture in the TEF area elongated along the anode due to the reduction in the Coulomb and radiation screening of the TEF.

CHAPTER 1

INTRODUCTION

1. 1 Terahertz Radiation

Terahertz (THz) radiation (electromagnetic radiation in the frequency range from 0.3 to 20 THz) is a largely unexplored frontier area for research in science and engineering in part because reliable sources of high quality THz radiation have been scarce. In recent years researchers have become increasingly interested in exploiting THz radiation for numerous technological applications including spectroscopy, sensing, and imaging [1-3]. The so-called THz gap lies above the high-frequency range of electronics, but below the range of the traditional fields of optics as shown in Figure 1. 1. The fact that the THz frequency range lies in the transition region between electronics and photonics has led to creative ways in source development. Many groups have made great efforts to develop THz radiation sources in both continuous-wave and pulsed form.

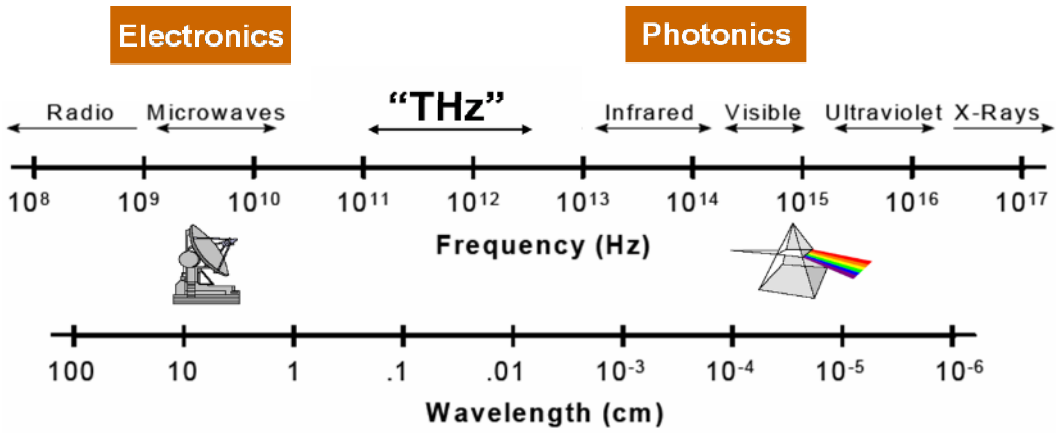

Figure 1. 1 THz radiation in the electromagnetic spectrum.

In particular, pulsed sources used in THz time domain spectroscopy (TDS) has generated a great deal of interest, and sparked a rapid growth in the field of THz science and technology.

In THz-TDS, picosecond pulses of THz radiation are used to probe different materials. The radiation has several distinct advantages over other forms of spectroscopy [4-6]: many materials are transparent to THz, THz radiation is safe for biological tissues because it is non-ionizing unlike X-rays, and images formed with THz radiation can have relatively good resolution (less than 1 mm). Also, many interesting materials have unique spectral fingerprints in the THz range, which means that THz radiation can be used to identify them. The emerging field of TDS typically relies on broadband short-pulse THz sources employing photoconductive switches, since the broad bandwidths correspond to short coherence lengths, which are required for high resolution imaging or tomography and sensing [7-9]. This broadband technique is also widely used to obtain linear spectroscopic information, such as complex dielectric constants or the conductivity of materials to fully understand the behavior with very broad spectral coverage. As implied in the title of the dissertation, we shall be dealing with ultrafast carrier dynamics in GaAs-based photoconductive THz sources to optimize the emitted THz transients using Monte Carlo techniques. These will be detailed in the ensuing chapters of the dissertation.

1.2 Photoconductive Switches

Photoconductive switches are very important devices for the generation of broadband THz pulses with high electric-field intensities suitable for spectroscopic,

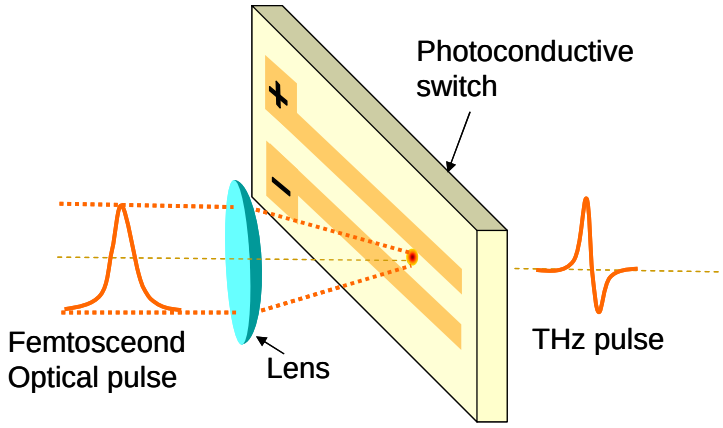

Figure 1. 2 Schematic of the photoconductive THz emitter.

sensing, and imaging purposes [10,11]. These devices were first proposed by Auston et al. and subsequently studied by many groups [12-14]. The photoconductive switch has two parallel metallic contacts deposited on the surface of a semiconductor as shown in Figure 1.2. THz pulses are typically produced by conduction between two electrodes patterned on a low temperature gallium arsenide (LT-GaAs), semi-insulating (SI-) GaAs, or other semiconductor (including InP) substrate. A dc bias is placed across the photoconductive switch, and an ultrashort pump-laser pulse (<100 fs) is focused in the gap in the photoconductive switch. Absorption of a ~100 fs laser (often a titanium sapphire laser (Ti-Sapphire laser)) pulse whose center frequency exceeds the bandgap of the semiconductor substrate generates carriers there between the electrodes. The mechanism underlying the THz radiation is to quickly create photoexcited carriers between the externally biased contacts using an ultrafast laser pulse. The charge carriers are then quickly accelerated to the opposite electrodes by the bias field and lead to the formation of an electrical dipole due to the difference of mobility between electrons and holes. This acceleration of the charge carriers by the external electric field generates an

electromagnetic transient. That is, the bias–laser pulse combination allows these charge carriers to rapidly jump the gap, and the resulting fast temporal change in a transient current can generate a pulse of electromagnetic radiation in the THz frequency range. The performance of THz generation depends on the temporal shape of photoinduced current from charge acceleration. The far-field radiation $E_{rad}(t)$ from the current distribution $J_s(t)$ ($\propto v$, v is drift velocity of the carrier) on the propagating axis of the radiation can be expressed by [15]

$$E_{rad}(t) \cong -\frac{A}{4\pi\varepsilon_0 c^2 r}\frac{dJ_s(t)}{dt} \propto a\,, \tag{1.1}$$

where A is the area of the emitter carrying the current distribution and a is acceleration of the carriers. Since the THz radiation in the far field is proportional to the time derivative of the current density, the emitted THz transient depends crucially on the carrier drift velocity. As a result, the THz radiation field has a field shape proportional to the acceleration of the photoexcited carriers. Very short THz pulses (typically ~2 ps) are

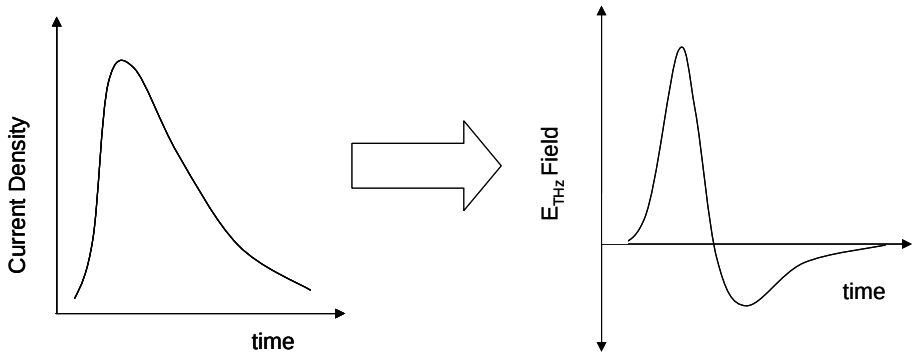

Figure 1. 3 Waveform of the THz radiation field. This pulse shape is proportional to the time derivative of the current density.

produced due to the rapid rise of the photo-induced current in the gap and in short-lifetime materials such as LT-GaAs, and the fall of the photocurrent as shown in Figure 1.3. This current may persist for only a few hundred femtoseconds or up to several nanoseconds, depending on the material of which the substrate is composed. This potoconductive switch puts out a train of pulses, whose repetition frequency is the same as that of the femtosecond pump laser. Pulse widths are on the order of 100 fs, with average powers below a few hundred nW and a frequency spread of > 500 GHz. The pulse bandwidth is typically centered at about 1 to 2 THz. The details of the spectrum can vary significantly, however, depending on the design of the switch and pump-laser power, pulse width and shape, and configuration.

1.3 Motivation

1.3.1 Power Saturation from Screening Effects

Ultrafast broadband THz transients generated by femtosecond optical pulses incident upon biased photoconductors are commonly employed for table-top THz sources. While this technique is approaching routine, the THz output power is quite low (typically a few hundred nW) and the optical-to-THz conversion efficiency disappointingly small (<0.01 %) [16,17]. In order to extend the use of these sources to enhance spectroscopy, sensing, and imaging with more high brightness, a significant increase of THz radiation in power is required. But when the charges separate, they create an electric field that counteracts the external bias, thus reducing the effective field, so the THz output strength is saturated as shown in Figure 1.4. Therefore a great deal of effort has been made to

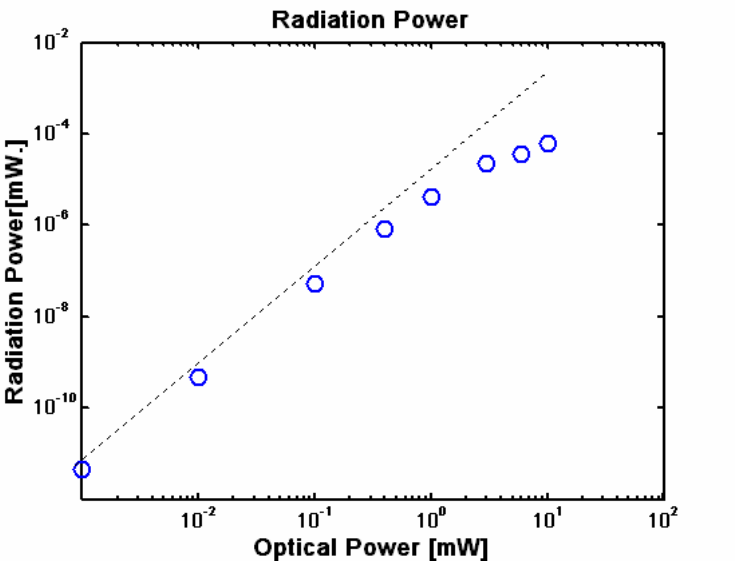

Figure 1. 4 THz radiation power vs incident optical power without screening (dashed line) and with screening (circle) [18].

understand the physical mechanisms that limit the radiation power and to increase the power of emitted THz radiation, such as using large aperture emitters for avoidance of saturation effects. One of the key limitations of power saturation is the screening of the bias field by the photogenerated carriers [15,19]. In many cases, however, these have been ignored, and to improve device performance, the systematic exploration of screening effects to extract the maximum THz spectral power density in the frequency range of interest is needed. The origins of this screening are the Coulomb field (due to photexcited space charge) and the radiation field (back action of the emitted THz transient on the device) [15,20-22].

1.3.2 Previous Work

A great effort has been made to improve the performance of such THz sources, with considerable attention paid to optimization bandwidth and boosting the THz power as well as the optical-to-THz conversion efficiency, e.g. with multiple-optical pulse excitations [23], and using semi-insulating or low temperature grown material [11], photoconducting dipole antennas and antenna arrays [24,25], asymmetric excitation [26,27], optical excitation pulse shaping [28], and large-aperture photoconductors [12,29]. In order to improve the performance of THz sources as in the previous work, an understanding of the carrier dynamics in photoconductive switches is of major importance. Several theoretical studies with the charge transport treated using rate equations based on the Drude-Lorentz model have been performed to understand different aspects of the process of THz emission by photoconductive switches [30-32]. In these studies, however, the presence of the subsidiary valleys in the band structure and the effects of spatial carrier distribution have not been fully considered at the same time. The performance of THz generation depends on the temporal shape of the photoinduced current pulses and this shape is determined in part by transient velocity overshoot and the screening due to the optically excited electron and hole distributions. Thus we need transport properties and relaxation processes of photoexcited carrieres with the effect of spatial distribution.

1.3.3 High Field Transport and Ultrafast Phenomena

For submicron devices to enable the development of compact THz systems with high radiation power, even a few tenths of a volt of applied voltage may cause field

strength of tens of kV/cm. The energy distribution of the electrons under these conditions may be quite different from what occurs at low fields. Under high-field conditions transient non-equilibrium effects, such as velocity overshoot and ballistic transport occur [33,34] on subpicosecond time scales. During the transient response, the distribution functions of the carriers is highly nonlinear in the applied field; carrier densities and other parameters, such that the transport properties must be studied by more sophisticated means, such as Monte Carlo techniques.

Hot electron conditions also occur when a laser beam is incident on a semiconductor sample, even in the absence of any external fields. In this case, a drastic alteration of the electron energy distribution is present shortly after excitation of the carriers to higher energy levels. However, the carriers soon relax to the equilibrium state through scattering processes. These energy and momentum relaxations processes are determined by the nature of the scattering, which is on the subpicosecond scale. When an external bias is also present, two processes can be identified following excitation of photocarriers: the carrier heating process in which carriers gain energy from the field and the carrier relaxation process in which they lose energy to the lattice via carrier-phonon interactions. This condition forms the basis for time resolved measurements of the transient photoresponse of the system [35,36]. Thus, there is an increasing need of modeling of high-field transport and ultrafast phenomena in compact photoconductive THz sources in which nonlinearity is important. These time and space dependent phenomena in photoexcited carrier problems are the most applicable areas for Monte Carlo techniques we choose.

1.4 Overview of Dissertation

The dissertation is organized in such a way that the main theory and methodology as well as application results are discussed in the main chapters. Chapter 1 has discussed THz radiation by a photoconductive switch, its application and challenges, and the motivation for the approach to solving these problems. Chapter 2 reviews the theoretical background for semiclassical transport including the Boltzmann transport equation, energy band structure and the scattering mechanisms incorporated into our model. In Chapter 3, we illustrate the basic ingredients and detail the numerical algorithms of the ensemble Monte Carlo coupled with a Poisson solver. We show the device models in this simulator in this chapter. In Chapter 4, the model developed in the previous chapter is applied to study the photoexcitation and THz response of photoconductive THz sources. In this chapter, we investigate the spatially resolved carrier dynamics and Coulomb and radiation fields in photoconductive THz sources. In addition, we detail the mechanisms responsible for the large TEF near the anode of SI-GaAs based photoconductors and show how the combination of illumination geometry, deep traps, and the applied bias field affects and controls the transient response. Finally in Chapter 5, we conclude giving a summary of the major results of this work.

CHAPTER 2

SEMICLASSICAL TRANSPORT THEORY

The concept of semiclassical transport theory is based on the assumption that a single carrier distribution function f (**k**, **r**, t) may be used to compute the statistical expectation value of macroscopic quantity. In this concept, the carriers are treated as independent classical particles. These particles are subject to the action of external fields and scattering mechanisms. The carriers experience a sequence of free flight scattering events in which they are accelerated by the field during their free fights, which are governed by classical laws of motion determined from band structures and interrupted by collisions, which are determined by the type of scattering event according to the scattering probabilities. The evolution of a carrier distribution function allows us to calculate any quantity A from ensemble average over momentum space k and real space r

$$\langle A(t) \rangle = \int dr \int dk A(\mathbf{k}, \mathbf{r}, t) f(\mathbf{k}, \mathbf{r}, t) . \tag{2.1}$$

The basis of semiclassical transport theory is the Boltzmann transport equations. To understand the spatio-temporal response of carriers on subpicosecond timescale, we use the Boltzmann transport equations from which the carrier distributions can be obtained.

2.1 The Boltzmann Transport Equation

The motion of the photoexcited carriers in a photoconductor is influenced by external fields, temperature gradients, density gradients, and scattering from impurities,

phonons, and other carriers [37,38]. All these factors have to be balanced against each other to give the transport properties of the carriers. The electrical properties can be obtained by calculating the distribution function f (**k**, **r**, t), which is proportional to the probability of finding a carrier in the state **k**, at time t and location **r**, from the Boltzmann transport equation

$$\frac{\partial f_{\mathbf{k}}}{\partial t} = -\left[\frac{\mathbf{F}}{\hbar}\nabla_{\mathbf{k}} f_{\mathbf{k}} + \frac{1}{\hbar}\nabla_{\mathbf{k}} E \cdot \nabla_r f_{\mathbf{k}}\right] + \int d\mathbf{k}\left\{f_{\mathbf{k}'}\left[1 - f_{\mathbf{k}}\right]\Gamma_{\mathbf{k}'\mathbf{k}} - f_{\mathbf{k}}\left[1 - f_{\mathbf{k}'}\right]\Gamma_{\mathbf{k}\mathbf{k}'}\right\}, \tag{2.2}$$

where $\hbar$ is the Plank constant divided by 2π and **F** is electric field. The left hand side of Eq. (2.2) describes the temporal variation of the distribution function. The first term on the right hand side of Eq. (2.2) is the force term, which describes changes in the distribution function due to applied fields, while the second term governs spatial variations (diffusion) in the system due to concentration or temperature gradient. The first bracket is the transport term (band structure limited), while the second bracket is the collision term (scattering limited). The first term inside the second bracket describes the scattering into state **k** (in-scattering) and the second one represents scattering out of state **k** (out-scattering). The transition rates $\Gamma_{\mathbf{k}\mathbf{k}'}$ and $\Gamma_{\mathbf{k}'\mathbf{k}}$ for the scattering between states **k** and **k**′ are calculated using first-order time-dependent perturbation theory, which leads to the so called Fermi's Golden Rule. (Details of the scattering mechanisms are discussed in Sec. 2.4.)

There are three main assumptions in applying the Boltzmann transport equation (BTE): effective mass theory and the band model hold, scattering rates are independent of the electric field, and collisions are instantaneous in both time and space. The approaches to solving the BTE are sketched in Figure 2.1. Each approach has its own advantage and

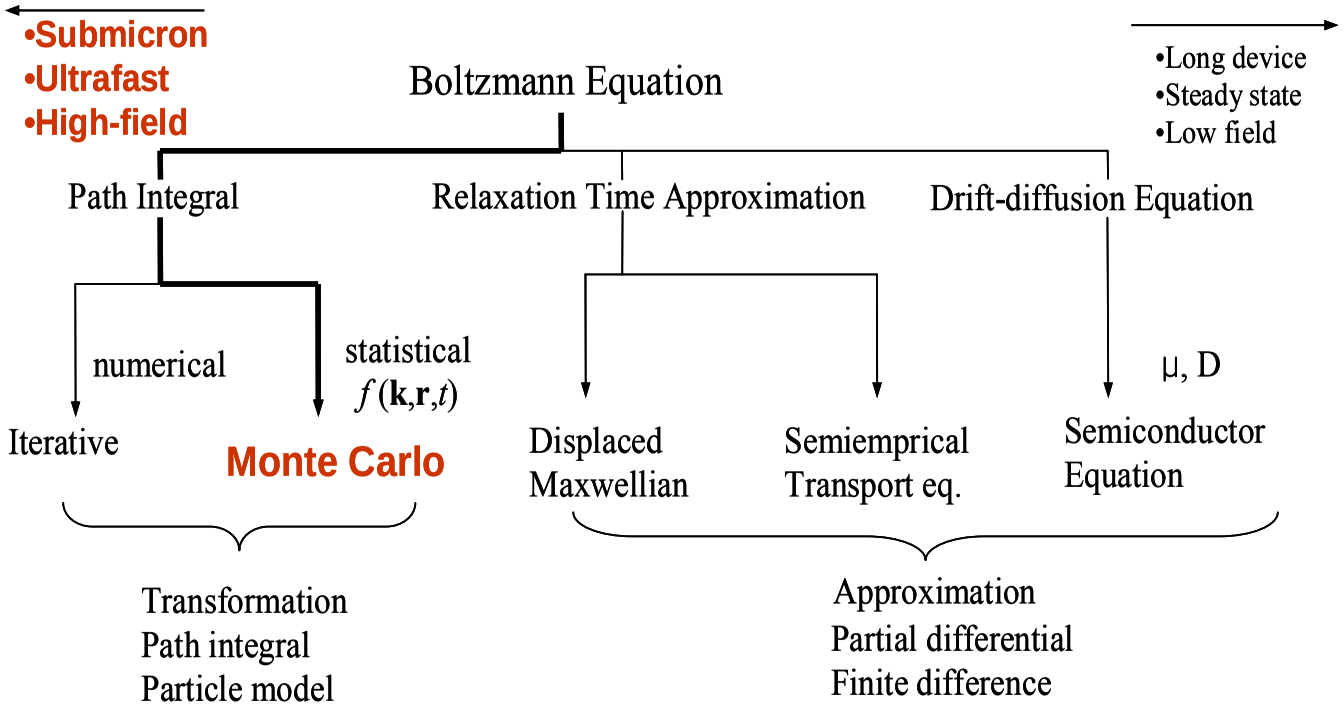

Figure 2. 1 The approaches to Boltzmann transport equation.

disadvantage, as well as its range of validity. The drift-diffusion approach is routinely used for long devices in low-field and steady-state conditions. However, the conditions for its validity restrict the application to submicron devices in which transient and nonequilibrium transport are important. Employing the Relaxation Time Approximation (sometime called hydrodynamic) which is based on higher moments of the BTE can improve the drift-diffusion model. When highly nonequilibrium conditions prevail, such as occur in photocarrier relaxation processes or transport by multi-dimensional carriers, these nonlinear transport processes depend sensitively on the shape of the distribution function, and the relaxation time approximation may also be inadequate. For a full description of BTE by numerical solutions, Monte Carlo methods have been successful due to the simplicity of their implementation, and the direct interpretation of various phenomena, including spatial-temporal effects, high-field transport, and ultrafast phenomena.

2.2 Monte Carlo Method

The Monte Carlo method is a random sampling technique that involves deliberate use of random numbers in a calculation that has the structure of a stochastic process [39]. We use probabilistic Monte Carlo methods for the solution of nonprobabilistic problems, as in the following simple example.

Mathematically, the calculation of π is equivalent to finding the area of a circle of diameter 1,

$$\pi = \int_0^1 \sqrt{1-x^2}\,dx \times 4\,. \tag{2.3}$$

The Monte Carlo approach to the solution is to generate random pairs (x,y) using uniformly distributed random numbers $r \in [0,1]$ and count the fraction that lies inside the circle. The estimated value of the integral of Eq. (2.3) is then given by

$$\pi = \frac{\#\text{ of particles inside arc}}{\#\text{ of total particles}} \times 4 . \tag{2.4}$$

The simulated values approach the true value as the number of sampling points becomes large,; Monte Carlo methods are often the only effective means of evaluating integrals. Monte Carlo methods can be classified into two versions according to its implementation: single-particle Monte Carlo, which traces the motion of one electron for a sufficient long time and ensemble Monte Carlo, which follows the history of an ensemble of particles in parallel for a sequence of very short time intervals (typically 5×10^{-15} to 10^{-12} s) instead of following the history of a single particle for a long period of time typically (typically 10 to 100 ps). Both transient and steady-state transport variables can be obtained from an ensemble Monte Carlo simulation. (Details of the ensemble Monte Carol are discussed in Sec. 3.1.)

The Monte Carlo technique is one of the most efficient ways to solve the Boltzmann transport equation since no *a priori* presumption of the carrier distribution function is needed, which implies that an exact numerical solution to the Boltzmann transport equation can be obtained [39]. It has an impressive ability to deal with band and scattering details due to its ability to evaluate multi-dimensional integrals, providing direct spatial and temporal microscopic information about the system with high resolution. The Monte Carlo method, however, has its own disadvantages, such as its CPU intensiveness originating mainly from its microscopic description of the transport

physics and specification of a large number of parameters for band structure, scattering rates, etc. The details of the energy band structure used in this work and the scattering mechanism relevant for GaAs material are discussed in the rest of this chapter.

2.3 Band Structure

The band structure and the scattering rate are the basic ingredients in a Monte Carlo method, and particularly, the energy-wavevector relationship (energy band structure) of carriers determines their dynamical properties under the influence of an external force. Figure 2.2 show the region of GaAs band structure that is important in transport, with the details of the degenerate minima of the Γ, L, X, and maxima of the heavy-hole and light-hole bands. In high-field transport calculations, as it is always the case in normal device operation, carriers can have very high kinetic energy, i.e. values of **k** are far from the minima of the conduction band. In this region, the energy deviates

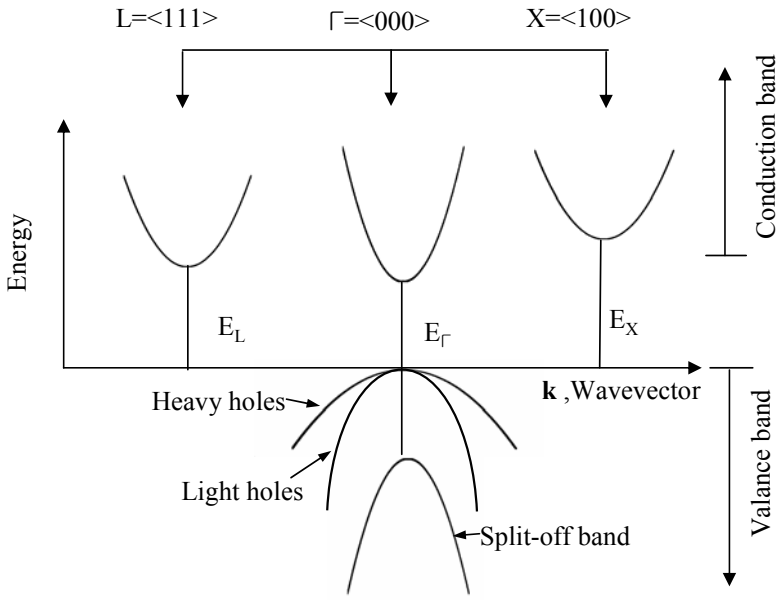

Figure 2. 2 Energy band structure of GaAs.

from the simple quadratic expressions of a parabolic band structure, and nonparabolicity occurs. In this case the E-**k** relationship as expressed by

$$E(1+\alpha E)=\gamma(k)=\frac{\hbar^2 k^2}{2m},\ \text{or}\quad E(\mathbf{k})=\frac{-1+\sqrt{1+4\alpha\gamma}}{2\alpha}, \tag{2.5}$$

gives a more appropriate description of the actual band structure. The α is a nonparbolicity factor defined as [40]

$$\alpha=\frac{1}{E_g}(1-\frac{m^*}{m_0})^2, \tag{2.6}$$

where E_g is the energy gap, m^* and m_0 are the effective electron mass at the bottom of the band and the free electron mass, respectively.

Once the band structure is known, the velocity associated with a state **k** can be calculated from the expression

$$\mathbf{v}(\mathbf{k})=\frac{1}{\hbar}\nabla_{\mathbf{k}}E(\mathbf{k}), \tag{2.7}$$

and in the case of a nonparabolic band, the velocity is given by

$$\mathbf{v}=\frac{\hbar\mathbf{k}}{m^*(1+2\alpha E)}=\frac{\hbar\mathbf{k}}{m^*\sqrt{1+4\alpha\gamma(k)}}\ . \tag{2.8}$$

The conduction band model of GaAs for photoconductive switches consists of spherical and non-parabolic Γ, L and X valleys. For the valence band structure, we include warping of the heavy and light hole band and a spherical parabolic split-off band, because

photoexcitation experiments in GaAs generate electrons from all three valence bands [39], and one can see electrons with anisotropic momentum distributions from the heavy and light hole bands [42]. For the warped bands, the E-k relationship is given by

$$E(\mathbf{k}) = \frac{|A|\hbar^2 k^2}{2m_0}(1 \pm g(\theta,\phi)), \tag{2.9}$$

where

$$g(\theta,\phi) = [(B/A)^2 + (C/A)^2(\sin^2\theta\cos^2\theta + \sin^4\theta\cos^2\phi\sin^2\phi)]^{1/2}. \tag{2.10}$$

In Eq. (2.10), the positive (negative) sign corresponds to the light (heavy) hole band, θ and ϕ are the polar and azimuthal angles of **k** with respect to the crystallographic axes respectively. A, B and C are the inverse valence band parameters [43].

2.4 Scattering Mechanisms

Scattering mechanisms describe the microscopic nature of electronic transport that governs the behavior of the carrier dynamics. They are typically determined using the Fermi's Golden rule, the effective mass, and the Born approximations. The dynamics of the electronic interactions is assumed to be independent of the applied field, and the collisions are assumed to occur instantaneously. Also, in the Born approximation, the scattering processes only consist of a transition between two definite momentum states. For the transition of an electron between different Bloch states in a crystal we have to make the assumption that the crystal has to be separated into the electron (hole) of

interest an the rest of the crystal. We will carry out the scattering rates with a first order and time-dependent perturbation approach.

2.4.1 Fundamental Transition Rate

The expression for the transition probability per unit time from a state **k** to a state **k**′ is induced by a perturbation Hamiltonian. The Hamiltonian may be decomposed as

$$H = H_0 + V_s\,,\ (H_0 + V_s)\psi = i\hbar\frac{\partial\psi}{\partial t} \tag{2.11}$$

where H_0 is the time independent Hamiltonian, $V_s(r,t)$ is a small random potential as shown in Figure 2.3.

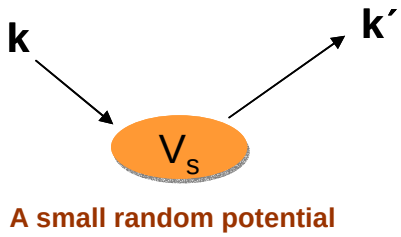

Figure 2. 3 A small random potential.

Meanwhile, if we suppose $t = -\infty$, the system starts in eigenfunction ψ_k of H_0 as

$$H_0\psi_k = E_k\psi_k\,,\ \ \psi_k(r,t) = \psi_k(r)e^{-iE_kt/\hbar} \quad . \tag{2.12}$$

An arbitrary state $\Psi(r,t)$ at time t can be specified by a linear combination of eigenstates

$$\Psi(r,t) = \sum_k c_k(t)\psi_k(r)e^{-iE_kt/\hbar} \quad , \tag{2.13}$$

where $c_k(t)$ is the probability amplitude of finding the system in state $\psi_k(t)$ at time t.

In the limit at $t\rightarrow\infty$, the probability of finding the particle in another state $\mathbf{k}'$ is

$$P_{kk'} = \lim_{t\to\infty}\left|c_{k'}(t)\right|^2 . \tag{2.14}$$

If $V_s << H_0$, the perturbed Hamiltonian H is very close to the unperturbed Hamiltonian H_0 then it is a good approximation to expand the solution in terms of unperturbed eigenstates. Thus, $\Psi(r,t)$ is also a solution of the perturbed Schrödinger Equation

$$\left[H_0 + V_s\right]\sum_k c_k(t)\psi_k(r)e^{-iE_k t/\hbar} = i\hbar\frac{\partial}{\partial t}\sum_k c_k(t)\psi_k(r)e^{-iE_k t/\hbar} \quad . \tag{2.15}$$

The H_0 coefficients cancel with the phase factor on right hand side to yield

$$V_s\sum_k c_k(t)\psi_k(r)e^{-iE_k t/\hbar} = i\hbar\sum_k \frac{\partial c_k(t)}{\partial t}\psi_k(r)e^{-iE_k t/\hbar} \quad . \tag{2.16}$$

Taking the inner product of both sides with $\psi_{k'}(r)e^{-iE_{k'}t/\hbar}$ gives

$$i\hbar\frac{\partial c_{k'}(t)}{\partial t} = \sum_k c_k(t)\left\langle k'\middle|V_s\middle|k\right\rangle e^{-i\left(E_{k'}-E_k\right)t/\hbar} \quad , \tag{2.17}$$

where the matrix element (using Dirac notation) is defined as

$$\left\langle k'\middle|V_s\middle|k\right\rangle = \int dr\,\psi^*_{k'}V_s\psi_k \quad . \tag{2.18}$$

We assume that at time $t=0$ the system is in a definite eigenstate ψ_k so that $\Psi(0)=\psi_k$. This implies that $c_k(0)=\delta_{kk'}$. Thus, from Eq. (2.17) the dominant term is

$$i\hbar \frac{\partial c_{k'}(t)}{\partial t} = \langle k' | V_s | k \rangle e^{-i(E_{k'} - E_k)t/\hbar} . \tag{2.19}$$

We can integrate this differential equation to find

$$c_{k'}(t) = \frac{1}{i\hbar} \int_0^t dt' \langle k' | V_s | k \rangle e^{-i(E_{k'} - E_k)t/\hbar} \quad . \tag{2.20}$$

If a perturbing potential V oscillates periodically with frequency ω, we can express it as a harmonic function:

$$V_s(r,t) = V_s(r) e^{\mp i\omega t} \quad . \tag{2.21}$$

This corresponds to interaction with lattice vibrations or with optical excitation. Substituting then we obtain

$$c_{k'}(t) = \frac{1}{i\hbar} \langle k' | V_s | k \rangle \int_0^t dt' e^{-iW_{kk'}t'}, \;\; W_{kk'} = (E_{k'} - E_k \mp \hbar\omega)/\hbar , \tag{2.22}$$

and integrating we have

$$c_{k'}(t) = \frac{1}{i\hbar} V_{kk'} e^{-iW_{kk'}t/2} \left(\frac{\sin(W_{kk'}t)}{W_{kk'}t} \right) t \quad . \tag{2.23}$$

If we want to find the transition rate from initial state **k** to final state **k′**, we just use the probability per unit time in Eq. (2.24). Therefore, the transition rate is

$$\Gamma_{kk'} = \frac{1}{t} \lim_{t \to \infty} |c_{k'}(t)|^2 = \frac{2\pi}{\hbar} |V_{kk'}|^2 \delta(E_{k'} - E_k \mp \hbar\omega) \quad . \tag{2.24}$$

This formula is called Fermi's Golden Rule and the δ-function in this formula is an expression of energy conservation. Assumptions made are there are no multiple scattering events and the contribution of other *c*'s is neglected.

The transition rate for scattering from a state **k** to a state **k′**, due to a perturbation with Hamiltonian H′, is given in first order by Fermi's Golden Rule from Eq. (2.24)

$$\Gamma_{\mathbf{k}\mathbf{k}'} = \frac{2\pi}{\hbar}\left|\left\langle \mathbf{k}\middle|H'\middle|\mathbf{k}'\right\rangle\right|^2 \delta(E_{k'} - E_k \mp \hbar\omega)\,, \tag{2.25}$$

where the squared matrix element contains the momentum conservation, while the delta-function expresses the conservation of energy during the scattering process. $E_{\mathbf{k}}$ and $E_{\mathbf{k}'}$ are the corresponding kinetic energy to the states and $\hbar\omega$ is the phonon energy. This squared matrix element can be factorized as follows

$$\left|\left\langle \mathbf{k}\middle|H'\middle|\mathbf{k}'\right\rangle\right|^2 = \left|V(\mathbf{q})\right|^2 G(\mathbf{k},\mathbf{k}')\,, \tag{2.26}$$

where $V(\mathbf{q})$ contains the dependence upon $\mathbf{q} = \mathbf{k} - \mathbf{k}'$, and depends on the momentum transfer depends on the nature of scattering. G is the overlap factor.

The overlap factor $G = 1$ for parabolic bands. However G is less than unity where nonparabolicity is significant, and can be expressed as

$$G(\mathbf{k},\mathbf{k}') = \frac{\left\{\left[1+\alpha E(\mathbf{k})\right]^{1/2}\left[1+\alpha E(\mathbf{k}')\right]^{1/2} + \alpha\left[E(\mathbf{k})E(\mathbf{k}')\right]^{1/2}\cos\theta\right\}^2}{\left[1+\alpha E(\mathbf{k})\right]^{1/2}\left[1+\alpha E(\mathbf{k}')\right]^{1/2}}\,. \tag{2.27}$$

The overlap effect is usually ignored in calculating the scattering rates in the three conduction valleys because G is very close to one. On the other hand, for intraband

transition within the heavy- or light-hole bands, the overlap factor is approximately given by [44]

$$G(\mathbf{k},\mathbf{k}') = \frac{1}{4}(1+3\cos^2\theta)\,, \tag{2.28}$$

while for interband transitions it can be expressed as

$$G(\mathbf{k},\mathbf{k}') = \frac{3}{4}\sin^2\theta\,, \tag{2.29}$$

where θ is the angle between **k** and **k′.**

The total scattering rate out of state **k** for a given mechanism is obtained by integrating Eq. (2.25) over all possible final states **k′**

$$\Gamma(k) = \frac{\mathrm{V}}{8\pi^3}\int dk'\int d\phi\int d\theta\Gamma_{\mathbf{kk}'}k'^2\sin\theta\,, \tag{2.30}$$

where V is the volume of the crystal, and ϕ is the azimuthal angle. The total scattering rate depends on the particular form of the squared matrix element of each scattering mechanism as well as the band structure. In the Monte Carlo method, it determines the scattering process, the time of free flight, and the final state at the end of the flight.

2.4.2 Scattering Rates

The electronic transitions in semiconductors are mostly caused by phonons, defects, and other carriers: The interaction of phonons with charge carriers is due to deformation potential interaction for both acoustic and optical phonons, or due to

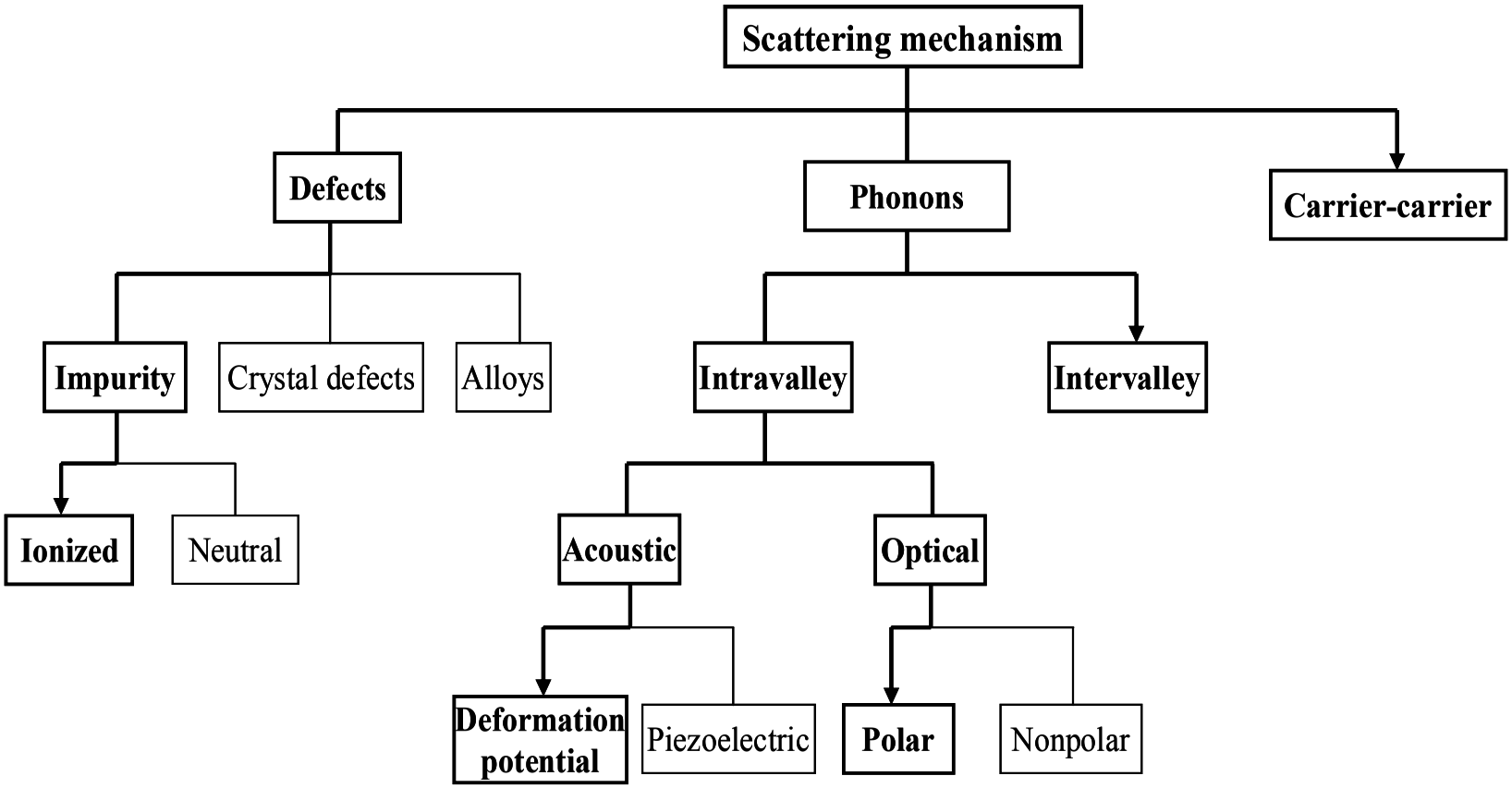

Figure 2. 4 Scattering mechanisms; bold-face indicating those mechanisms implemented in our simulation.

piezoelectric interaction for the acoustic phonons, and polar interaction for optical phonons, typically in polar materials. Defects can arise from impurities and dislocation, etc. Carrier-carrier interactions are important at higher carrier concentrations. On the other hand, the scattering mechanisms can be classified as intravalley or intervalley, if both initial and final states of the carrier lie in the same or different valley, respectively.

Figure 2.4 illustrates the major scattering mechanisms [39] with bold-face scattering mechanisms taken into account for our simulation; acoustic-phonon scattering, ionized-impurity scattering, intervalley scattering, carrier-carrier scattering and screened carrier-phonon scattering [39-43,45,46]. We calculate the screening length self-consistently, which affects the scattering rates of the ionized impurity, carrier-carrier, and screened carrier-phonon interactions using the evolving built-in distribution function [46].

2.4.2.1 Total Electron Scattering Rates

We present the salient results of the scattering rates, which have been implemented in our simulation with brief discussions. Usually, the total scattering rate is expressed as a function of energy.

(a) *Ionized impurities scattering*

This mechanism is elastic in nature and cannot control the transport by itself in the presence of an external field. It is more efficient in terms of both scattering rate and scattering angle when the average energy of the electron is low. The scattering angle becomes smaller as the average electron energy gets higher and hence, it plays a negligible role in high-field transport. Here is the Brooks-Herring (BH) model, which assumes an exponential screening factor for the scattering potential

$$V(r) = \frac{Ze^2}{4\pi\varepsilon\varepsilon_0 r}\exp(-\beta r), \tag{2.31}$$

where ε is the dielectric constant of the material, ε_0 is the free-space permittivity, and Z is the number of charge units at the impurity. β is the inverse screening length given by the Debye-Huckel model

$$\beta = \left[\frac{ne^2}{\varepsilon\varepsilon_0 k_B T}\right]^{1/2}, \tag{2.32}$$

where n is the carrier density, which can be approximated by N_I, the impurity concentration, k_B is the Boltzmann constant and T is the lattice temperature. The square of the matrix element is given by

$$|V(q)|^2 = \frac{N_I Z^2 e^4}{(4\pi\varepsilon r)^2 (q^2+\beta^2)^2}. \tag{2.33}$$

The integrated scattering rate in a nonparabolic band structure is given by

$$\Gamma(E) = \frac{ne^4}{32\pi(\varepsilon\varepsilon_0)^2(2m^*)^{1/2}} \frac{1}{C(k)[1+C(k)]} \frac{1+2\alpha E}{E^{3/2}(1+\alpha E)^{3/2}},$$

$$C(k) = \left(\frac{\beta}{2k}\right)^2. \tag{2.34}$$

The angular dependence expressed in terms of a random number r is given by

$$\cos\theta = 1 + \frac{2(r-1)}{1+r/C(k)}, \tag{2.35}$$

where θ is the angle between **k** and **k′**.

(b) ***Intravalley – polar optical phonon scattering***

Polar optical phonon scattering is an important mechanism in polar materials such as GaAs in intravalley transitions. Its strength decreases rapidly as q gets larger which is the case for intervalley transitions as shown in the square of matrix elements,

$$|V(q)|^2 = \frac{\hbar e^2 \omega_0}{2\mathrm{V} q^2 \varepsilon_0}\left[\frac{1}{\varepsilon_\infty} - \frac{1}{\varepsilon_s}\right] \times \begin{bmatrix} N_o & \text{(absorption)} \\ N_o + 1 & \text{(emission)} \end{bmatrix}. \tag{2.36}$$

The integrated scattering rate in a nonparabolic band structure due to the polar optical phonons is given by

$$\Gamma(E) = \frac{e^2 \omega_0 m^{*1/2}}{4\sqrt{2}\hbar\pi\varepsilon_0}\left[\frac{1}{\varepsilon_\infty} - \frac{1}{\varepsilon_s}\right] \frac{(1+2\alpha E')}{\gamma^{1/2}(E)} F_o(E,E') \times \begin{bmatrix} N_o & \text{(absorption)} \\ N_o + 1 & \text{(emission)} \end{bmatrix}, \tag{2.37}$$

where

$$E' = \begin{cases} E + \hbar\omega_0 & \text{(absorption)} \\ E - \hbar\omega_0 & \text{(emission)} \end{cases},$$

$$F_o(E,E') = \frac{1}{C}\left[A \ln\left|\frac{\gamma^{1/2}(E) + \gamma^{1/2}(E')}{\gamma^{1/2}(E) - \gamma^{1/2}(E')}\right| + B \right],$$

$$A = \left\{2(1+\alpha E)(1+\alpha E') + \alpha\left[\gamma(E) + \gamma(E')\right]\right\}^2 ,$$

$$B = -2\alpha\gamma^{1/2}(E)\gamma^{1/2}(E')\left\{4(1+\alpha E)(1+\alpha E') + \alpha\left[\gamma(E) + \gamma(E')\right]\right\}$$

$$C = 4(1+\alpha E)(1+\alpha E')(1+2\alpha E)(1+2\alpha E')$$

$$N_0 = \left[\exp(\hbar\omega_o / k_B T) - 1\right]^{-1}. \tag{2.38}$$

ε_∞ and ε_s are the high and low frequency dielectric constants respectively. N_0 is the polar optical phonon occupation number and ω_o is the optical phonon frequency. This mechanism is strongly anisotropic. The angular dependence can be expressed using random numbers, $r \in (0,1)$ as

$$\cos\theta = \frac{1+2\sqrt{EE'}(\sqrt{E}-\sqrt{E'})^{-2} - \left[1+4\sqrt{EE'}(\sqrt{E}-\sqrt{E'})^{-2}\right]^r}{2\sqrt{EE'}(\sqrt{E}-\sqrt{E'})^{-2}}. \tag{2.39}$$

(c) *Intervalley scattering*

Intervalley scattering including equivalent or nonequivalent valleys becomes a dominant mechanism at high fields when the electron average energy is higher than the separation between the central and upper valley. These transitions between different valleys involve a large amount of moment transfer. The squared matrix element is given by

$$|V(q)|^2 = \frac{\hbar \Xi_{if}^{\ 2}}{2\rho\omega_{if}} \times \begin{bmatrix} N_{if} & \text{(absorption)} \\ N_{if}+1 & \text{(emission)} \end{bmatrix}, \tag{2.40}$$

The intervalley scattering rate in a nonparabolic band structure is given by

$$\Gamma(E) = \frac{Z_f m_f^{*3/2} \Xi_{if}^{\ 2}}{\sqrt{2}\pi\hbar^3\rho\omega_{if}} \gamma_f^{\ 1/2}(E')(1+2\alpha_f E')F_{if}(E,E') \times \begin{bmatrix} N_{if} & \text{(absorption)} \\ N_{if}+1 & \text{(emission)} \end{bmatrix}, \tag{2.41}$$

where

$$E' = \begin{cases} E_i - \Delta E_{if} + \hbar\omega_{if} & \text{(absorption)} \\ E_i - \Delta E_{if} - \hbar\omega_{if} & \text{(emission)} \end{cases},$$

$$F_{if}(E,E') = \frac{(1+\alpha_i E)(1+\alpha_j E')}{(1+2\alpha_i E)(1+2\alpha_j E')},$$

$$N_{if} = \left[\exp(\hbar\omega_{if}/k_B T) - 1\right]^{-1}. \tag{2.42}$$

Ξ_{if} is the intervalley deformation potential, Z_f is the number of valleys of type, ω_{if} is the intervalley phonon frequency, ΔE_{if} is the energy difference between the minima and N_{if} is the intervalley phonon occupation number. Intervalley scattering processes are isotropic, so we can obtain the polar and azimuthal angles from two random numbers, r_1 and r_2 $\in(0,1)$ due to the energy conserving sphere:

$$\cos\theta = 1 - 2r_1, \qquad \phi = 2\pi r_2. \tag{2.43}$$

To study the fast transitions properly using Ensemble Monte Carlo we need to calculate the screening length self-consistently using the evolving built-in distribution function. The square of the inverse screening length β^2 is proportional to the ensemble average of *B(E)* and is given by

$$\beta^2 = \frac{ne^2}{\varepsilon\varepsilon_0}\frac{1}{N}\sum_{i=1}^{N} B(E_i), \tag{2.44}$$

where N is the number of carriers in the ensemble. The *B(E)* depends on the band model and is given by

$$B(E) = \frac{2\alpha}{1+2\alpha E} + \frac{1+2\alpha E}{2E(1+\alpha E)}, \tag{2.45}$$

for nonparabolic bands.

(d) ***Intravalley – acoustic phonon scattering with deformation-potential interaction.***

Acoustic phonon scattering is quasi-elastic process in high fields and temperature, and is less important than other mechanisms since the acoustic phonon energy is relatively small. The energy change in acoustic phonon scattering is negligible but for nonlinear transport problems in low fields, the small energy dissipation is needed to establish a smooth distribution function. The square of the matrix element is given by

$$|V(q)|^2 = \frac{\hbar \Xi^2 q}{2\rho s} \times \begin{bmatrix} N_o & \text{(absorption)} \\ N_o + 1 & \text{(emission)} \end{bmatrix}, \tag{2.46}$$

and the total scattering rate is

$$\Gamma(E) = \frac{(2m^*)^{3/2} k_B T_0 \Xi_a^2}{2\pi\hbar^4 s^2 \rho} \gamma^{1/2}(E)(1+2\alpha E) F_a(E), \tag{2.47}$$

where

$$F_a(E) = \frac{(1+\alpha E)^2 + \frac{1}{3}(\alpha E)^2}{(1+2\alpha E)^2}, \tag{2.48}$$

ρ is the density of crystal, T_0 is the lattice temperature, Ξ_a is called the acoustic deformation potential and s is the acoustic wave velocity. For nonparabolic bands this scattering is anisotropic, and we can obtain the angular dependence using random numbers, $r \in (0,1)$ as follows :

$$\cos\theta = \frac{[(1+2\alpha E)^3(1-r)+r]^{1/3} - (1+\alpha E)}{\alpha E}, \tag{2.49}$$

(e) ***Screened electron-phonon scattering***

The electron-electron interaction modifies the electron-phonon interaction by screening these interactions. The scattering rate is given by

$$\Gamma(E) = A\frac{\gamma(E')}{\gamma^{1/2}(E)}\left[\ln\left[\frac{u}{z}\right] - E_\beta\left[\frac{1}{z} - \frac{1}{u}\right]\right]\times\begin{bmatrix} N_o & \text{(absorption)} \\ N_o + 1 & \text{(emission)}\end{bmatrix}, \tag{2.50}$$

where

$$A = \frac{e^2\omega_0 m^{*1/2}}{8\sqrt{2}\hbar\pi\varepsilon_0}\left[\frac{1}{\varepsilon_\infty} - \frac{1}{\varepsilon_s}\right],$$

$$u = \left[\gamma^{1/2}(E) + \gamma^{1/2}(E')\right]^2 + E_\beta,$$

$$z = \left[\gamma^{1/2}(E) - \gamma^{1/2}(E')\right]^2 + E_\beta,$$

$$E_\beta = \frac{\hbar^2\beta^2}{2m},$$

$$E' = \begin{cases} E + \hbar\omega_0 & \text{(absorption)} \\ E - \hbar\omega_0 & \text{(emission)}\end{cases}. \tag{2.51}$$

The angular dependence of the scattering is determined from [46]

$$p(\cos\theta) = \frac{|\mathbf{k}|^2 + |\mathbf{k}'|^2 + 2|\mathbf{k}||\mathbf{k}'|\cos\theta}{\left[|\mathbf{k}|^2 + |\mathbf{k}'|^2 - 2|\mathbf{k}||\mathbf{k}'|\cos\theta + \beta^2\right]^2}. \tag{2.52}$$

(f) ***Electron-electron (e-e) scattering.***

The carrier-carrier interaction is very important at high carrier densities and inclusion of this mechanism makes the Boltzmann transport equation nonlinear. We only

present the salient results of the carrier-carrier scattering rates. The e-e scattering rate is given by

$$\Gamma_{ee}(\mathbf{k_0}) = \frac{ne^4}{2\pi\varepsilon^2\hbar^3\beta^2}\frac{1}{N_e}\sum_k \frac{\mu g}{(g^2+\beta^2)}, \tag{2.53}$$

where

$$\mu = \frac{m_0 m}{m_0 + m}, \quad \mathbf{g} = 2\mu\left(\frac{\mathbf{k}}{m} - \frac{\mathbf{k_0}}{m_0}\right). \tag{2.54}$$

N_e is the number of electrons in the ensemble and the sum is over all the k vectors of the ensemble carriers. **g** is the relative wavevector, m_0 and $\mathbf{k_0}$ are the effective mass and wavevector of the Monte Carlo electron, and m and **k** are the effective mass and wavevector of the counterpart electron.

The angular dependence as obtained using random numbers r is given by

$$\cos\theta = 1 - \frac{2r}{1 + g^2(1-r)/\beta^2}, \tag{2.55}$$

where θ is the angle between **g** and **g′**. The final states of the two interacting electrons after e-e scattering are given by

$$\mathbf{k_0'} = \mathbf{k_0} - \frac{1}{2}(\mathbf{g'} - \mathbf{g}),$$

$$\mathbf{k'} = \mathbf{k} + \frac{1}{2}(\mathbf{g'} - \mathbf{g}). \tag{2.56}$$

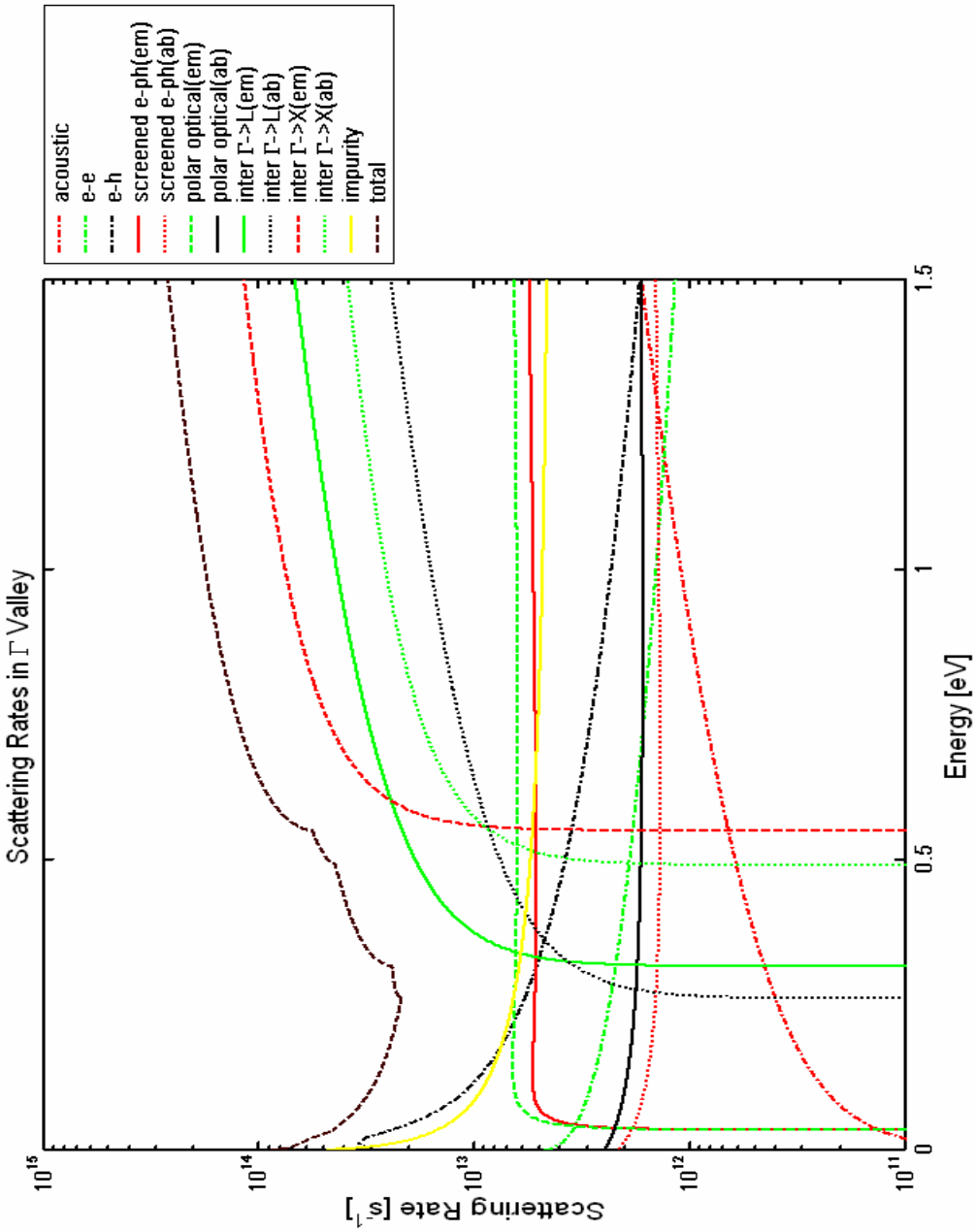

Figure 2.5 Scattering rates vs energy in GaAs at room temperature in the Γ valley.

(g) *Electron-hole(e-h) scattering*

The e-h scattering rate is given by

$$\Gamma_{eh}(\mathbf{k_0}) = \frac{ne^4}{2\pi\varepsilon^2\hbar^3\beta^2}\frac{1}{N_h}\sum_k \frac{\mu g}{(g^2+\beta^2)}, \tag{2.57}$$

where

$$\mu = \frac{m_0 m_h}{m_0 + m_h}, \qquad \mathbf{g} = 2\mu\left(\frac{\mathbf{k}}{m_h} - \frac{\mathbf{k_0}}{m_0}\right). \tag{2.58}$$

N_h is the number of holes in the ensemble and the sum is over all the **k** vector of the ensemble carriers. The angular dependence is given in the same way as for the e-e interaction (see Eq. (2. 55)).

The various types of scattering rates discussed above are calculated for GaAs at room temperature, and scattering rates in the Γ valley are plotted in Figure 2.5. For e-e, e-h interaction process, we assumed a Maxwellian distribution for illustrative purposes.

2.4.2.2 Total Hole Scattering Rates

We only present the salient results of the total hole scattering rates, which have been implemented in our simulation with brief discussions.

(a) *Screened hole-phonon scattering.*

The intraband scattering rate is

$$\Gamma_{ii}(E) = A\Psi(E)G_{ii}(E)E^{-1/2} \times \begin{bmatrix} N_o & \text{(absorption)} \\ N_o + 1 & \text{(emission)} \end{bmatrix}, \tag{2.59}$$

where

$$\Psi(E) = \ln\left(\frac{\left[E^{1/2} + E'^{1/2}\right]^2 + E_\beta}{\left[E^{1/2} - E'^{1/2}\right]^2 + E_\beta}\right),$$

$$G_{ii} = \frac{1}{4}\left\{1 + 3\Phi\left(\Phi - \frac{2}{\Psi}\right) + 6(\Phi - \phi)\left(\Phi - \left(1 + \frac{\Phi^2}{\Phi^2 - 1}\right)\Psi^{-1}\right)\right\},$$

$$\Phi(E) = \frac{E + E' + E_\beta}{2(EE')^{1/2}},$$

$$\phi(E) = \frac{E + E'}{2(EE')^{1/2}}. \tag{2.60}$$

The index i=1 for heavy holes and 2 for light holes.

For interband scattering from band i to band j the scattering rate is

$$\Gamma_{ij}(E) = A_{ij}\Psi_{ij}(E)G_{ij}(E)E^{-1/2} \times \begin{bmatrix} N_o & \text{(absorption)} \\ N_o + 1 & \text{(emission)} \end{bmatrix}, \tag{2.61}$$

where

$$A_{ij} = \frac{e^2\omega_0}{8\sqrt{2}\hbar\pi\varepsilon_0}\frac{m_j^{1/2}}{m_i^{1/2}}\left[\frac{1}{\varepsilon_\infty} - \frac{1}{\varepsilon_s}\right],$$

$$\Psi_{ij}(E) = \ln\left(\frac{\left[E^{1/2} + \left(\frac{m_j}{m_i}E'\right)^{1/2}\right]^2 + E_\beta}{\left[E^{1/2} - \left(\frac{m_j}{m_i}E'\right)^{1/2}\right]^2 + E_\beta}\right),$$

$$G_{ij} = \frac{3}{4}\left\{1 - \Phi_{ij}\left(\Phi_{ij} - \frac{2}{\Psi_{ij}}\right) - 2(\Phi_{ij} - \phi_{ij})\left(\Phi_{ij} - 2\Psi_{ij}^{-1}\right)\right\},$$

$$\Phi_{ij}(E) = \frac{E + \frac{m_j}{m_i}E' + E_\beta}{2(E\frac{m_j}{m_i}E')^{1/2}} \ ,$$

$$\phi_{ij}(E) = \frac{E + \frac{m_j}{m_i}E'}{2(E\frac{m_j}{m_i}E')^{1/2}} \ . \tag{2.62}$$

The angular dependence for intraband scattering processes takes the following form

$$p_{ii}(\cos\theta) = \frac{\left[|\mathbf{k}|^2 + |\mathbf{k}'|^2 + 2|\mathbf{k}||\mathbf{k}'|\cos\theta\right](1+3\cos^2\theta)}{\left[|\mathbf{k}|^2 + |\mathbf{k}'|^2 - 2|\mathbf{k}||\mathbf{k}'|\cos\theta + \beta^2\right]^2}. \tag{2.63}$$

Similarly for interband scattering processes the angular dependence is

$$p_{ij}(\cos\theta) = \frac{\left[|\mathbf{k}|^2 + |\mathbf{k}'|^2 + 2|\mathbf{k}||\mathbf{k}'|\cos\theta\right](1-2\cos^2\theta)}{\left[|\mathbf{k}|^2 + |\mathbf{k}'|^2 - 2|\mathbf{k}||\mathbf{k}'|\cos\theta + \beta^2\right]^2}. \tag{2.64}$$

In order to generate the angles after scattering the rejection technique [39] is used.

(b) ***Non polar optical phonon scattering with deformation potential interaction***

The scattering rate for intraband processes is given by

$$\Gamma_{ii}(E) = \frac{(2m_i)^{3/2}\Xi^2}{4\pi\rho\hbar^3\omega_0}\overline{G}_{ii}E'^{1/2} \times \begin{bmatrix} N_o & \text{(absorption)} \\ N_o + 1 & \text{(emission)} \end{bmatrix}, \tag{2.65}$$

while the interband scattering rates are

$$\Gamma_{ij}(E) = \frac{(2m_j)^{3/2}\Xi^2}{4\pi\rho\hbar^3\omega_0}\overline{G}_{ij}E'^{1/2} \times \begin{bmatrix} N_o & \text{(absorption)} \\ N_o + 1 & \text{(emission)} \end{bmatrix}, \tag{2.66}$$

where Ξ is deformation potential.

We can assume $\overline{G}_{ii} = \overline{G}_{ij} = 1/2$ since the matrix element has no angular dependence [39]. Consequently, the angles after scattering are selected using random numbers according to Eq. (2.43).

(c) ***Ionized impurity scattering***

The scattering rate is given by

$$\Gamma(E) = \frac{ne^4}{2\sqrt{2}\pi\varepsilon^2 E_\beta m^{1/2}} \frac{E^{1/2}}{(1+4\varepsilon/E_\beta)} G(E), \tag{2.67}$$

where

$$G(E) = \frac{1}{4}\left\{1 + \frac{3}{4}\frac{XY^2}{(E/E_\beta)^2}\left(\frac{1}{X} + \frac{1}{Y^2} + \frac{\ln\left[X^{-1}\right]}{2Y(E/E_\beta)}\right)\right\},$$

$$X = 1 + 4E/E_\beta,$$

$$Y = 1 + 2E/E_\beta. \tag{2.68}$$

The angular dependence is obtained from

$$P(\theta) = \frac{(1+3\cos^2\theta)\sin\theta}{\left[4k^2\sin^2\theta/2 + \beta^2\right]^2}. \tag{2.69}$$

(d) *Hole-hole (h-h) scattering*

The h-h scattering rate is given by

$$\Gamma_{hh}(\mathbf{k_0}) = \frac{ne^4}{2\pi\varepsilon^2\hbar^3\beta^2}\frac{1}{N_h}\sum_k \frac{\mu g}{(g^2+\beta^2)}, \tag{2.70}$$

where

$$\mu = \frac{m_0 m}{m_0 + m}, \qquad \mathbf{g} = 2\mu\left(\frac{\mathbf{k}}{m} - \frac{\mathbf{k_0}}{m_0}\right). \tag{2.71}$$

N_h is the number of holes in the ensemble and the sum is over all the k vectors of the ensemble carrier, **g** is the relative wavevector, m_0 and $\mathbf{k_0}$ are the effective mass and wavevector of the Monte Carlo hole, and m and **k** are the effective mass and wavevector of the counterpart hole. The angular dependence is given in the same way as for the e-e interaction (see Eq. (2. 55)).

(e) *Hole-electron (h-e) scattering*

The h-e scattering rate is given by

$$\Gamma_{he}(\mathbf{k_0}) = \frac{ne^4}{2\pi\varepsilon^2\hbar^3\beta^2}\frac{1}{N_e}\sum_k \frac{\mu g}{(g^2+\beta^2)}, \tag{2.72}$$

where

$$\mu = \frac{m_0 m_e}{m_0 + m_e} \quad \mathbf{g} = 2\mu\left(\frac{\mathbf{k}}{m_e} - \frac{\mathbf{k_0}}{m_0}\right), \tag{2.73}$$

N_e is the number of electrons in the ensemble and the sum is over all the **k** vector of the ensemble carriers. The angular dependence is given in the same way as for the e-e interaction (see Eq. (2. 55)).

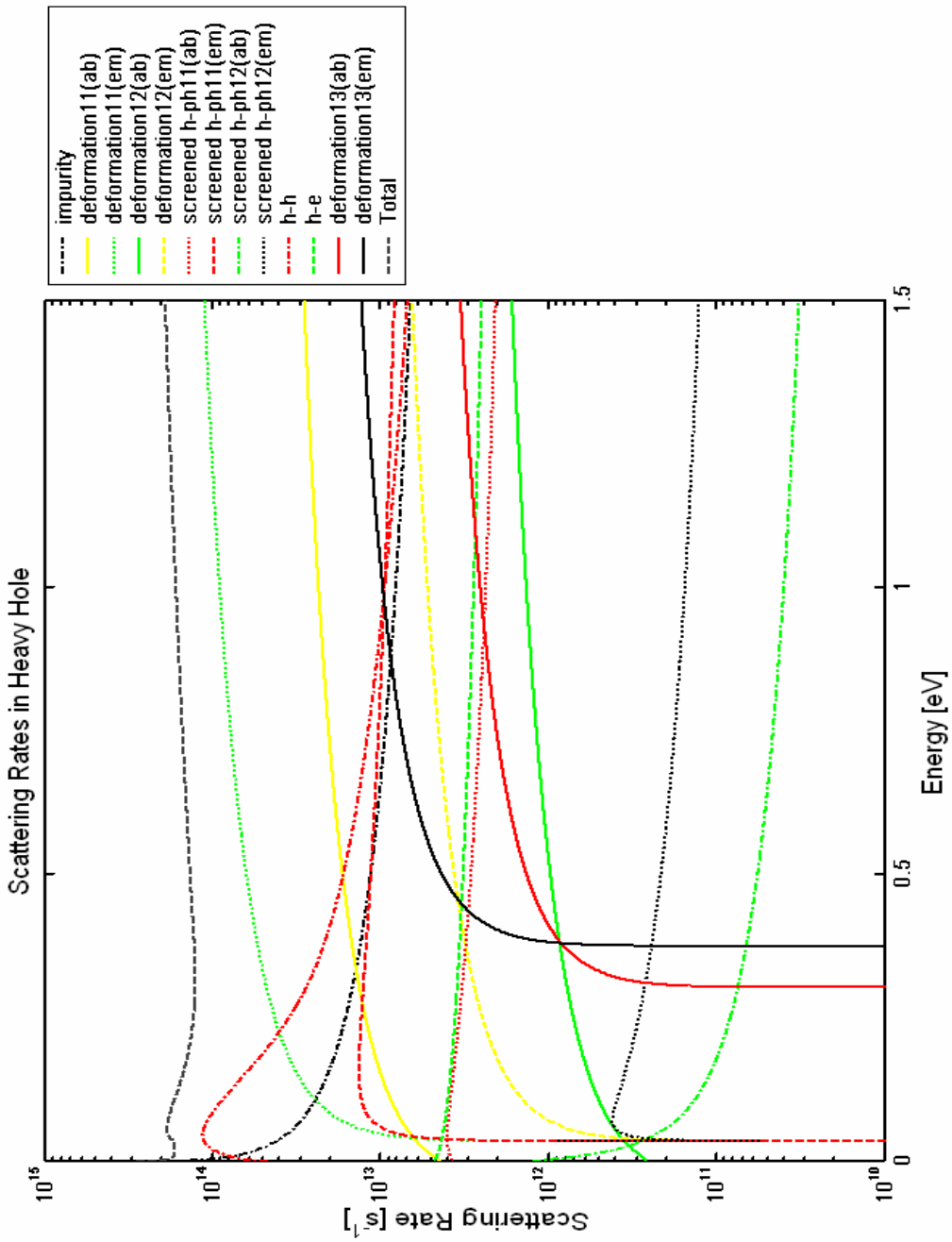

Figure 2.6 Scattering rates vs energy in GaAs at room temperature in the heavy hole band.

Various type of scattering rates discussed above are calculated for GaAs at room temperature, and scattering rates for the heavy hole band are plotted in Figure 2.6. For the h-h, h-e interaction processes, we assumed a Maxwellian distribution for illustrative purpose. The material properties of GaAs and the valley dependent material parameters for the electron and hole transports are shown in Tables 2.1 and 2.2 respectively.

Since ionized impurity, polar optical phonon, and acoustic phonon scattering are anisotropic processes, the final state $\mathbf{k}'$ after scattering is specified in terms of the scattering angle θ with respect to the initial state $\mathbf{k}$. Thus, a coordinate transformation is performed to obtain the final state with respect to the fixed direction, where k_x is assumed to be parallel to the direction of the bias field $\mathbf{E}$. The coordinate transformation is presented in Appendix A.

Table 2.1 Material properties of GaAs.

Parameters	GaAs	Units
Density of crystal (ρ)	5.37	g/cm^3
High frequency dielectric constant(ε_∞)	10.92	-
Low frequency dielectric constant(ε_s)	12.90	-
Longitudinal acoustic velocity(s)	5240	m/s
Optical phonon energy ($\hbar\omega_o$)	36	meV

Table 2.2 Valley dependent material parameters for GaAs carrier transport at 300 K.

Parameters	Γ(000)	L(111)	X(100)	Units
Effective mass ratio	0.063	0.222	0.58	m^*/m
Acoustic deformation potential(Ξ_a)	7	9.20	9.27	eV
Number of equivalent valleys(Z)	1	4	3	-
Intervalley deformation potential(Ξ_{if})				10^9eV/cm
Γ	0	1	1	
L	1	1	0.5	
X	1	0.5	0.7	
Intervalley Phonon energy ($\hbar\omega_{if}$)				meV
Γ	0	27.8	29.9	
L	27.8	29	29.3	
X	29.9	29.3	29.9	
Band gaps	1.43	1.73	1.9	eV
Nonparabolicity(α)	0.61	0.461	0.204	eV^{-1}
Valley separation (from Γ)	0	0.29	0.522	eV

CHAPTER 3

MONTE CARLO POISSON SOLVER

3.1 The Ensemble Monte Carlo Method

The Monte Carlo method is a way of simulating a system with random numbers generating numerically probability distributions to calculate the structure of a stochastic process. A single particle Monte Carlo method is suitable for the investigation of steady-state and homogeneous phenomena, because the motion of one particle for a sufficiently long time can provide information about the behavior of all particles, i.e. the time average is equal to the ensemble average. Meanwhile the ensemble Monte Carlo method is more useful and widely used for the calculation of non-stationary and transient transport that occur under non-uniform electric fields because this method follows the trajectory of an ensemble of particles in parallel for a sequence of short time intervals. Both transient and steady-state transport variables can be obtained from an ensemble Monte Carlo simulation. In the next subsections we describe the three main stages in a typical structure of Monte Carlo method, such as free flight time, selection of scattering process, and final state. Then we explain ensemble averaging schemes and we give representative simulation results for bulk GaAs.

3.1.1 Free Flight Time

Electrons are subject to the action of external forces due to electric fields according to Eq. (3.1) and drift freely until they are scattered by the lattice vibrations, impurities and other carriers.

$$\hbar\dot{\mathbf{k}} = -e\mathbf{E}, \tag{3.1}$$

The duration of this free flight between successive scattering events is called the free flight time and the electron wave vector **k** changes continuously during the duration of the free flight. The probability that an electron will drift freely for time t and then be scattered is given by

$$P(t) = \Gamma(\boldsymbol{k}(t))\exp\left(-\int_0^t \Gamma(\boldsymbol{k}(t'))dt'\right). \tag{3.2}$$

The free flight time t_f is then obtained by integrating Eq. (3.2) using a uniformly distributed random number r between 0 and 1 as

$$r = 1 - \exp\left(-\int_0^{t_f} \Gamma(\mathbf{k}(t'))dt\right). \tag{3.3}$$

However, due to the complexity of the integral at the exponent, it is impractical to generate free flights using Eq. (3.3). To overcome this problem, an additional fictitious self scattering is introduced to make the total scattering rate constant over the energy. The constant total scattering rate Γ is then given by

$$\Gamma(\mathbf{k}(t)) + \Gamma_{self} = \Gamma, \tag{3.4}$$

where Γ_{self} is the self scattering rate that does not affect the state of the particle at all. Using Eq. (3.4), we can obtain t_f in terms of the random number r by inverting Eq. (3.3) as

$$t_f = -\frac{\ln(1-r)}{\Gamma} = \frac{\ln r}{\Gamma} \tag{3.5}$$

3.1.2 Selecting the Scattering Process

Once the free flight time is determined, the scattering mechanism responsible for terminating a free flight and determining a new state should be selected at the end of the free flight. For the selection we have to consider in detail each scattering mechanism Γ_1, Γ_2, through Γ_n, evaluated using the particle energy at the end of the free flight. The scattering mechanism is selected by generating a second uniform random number r.

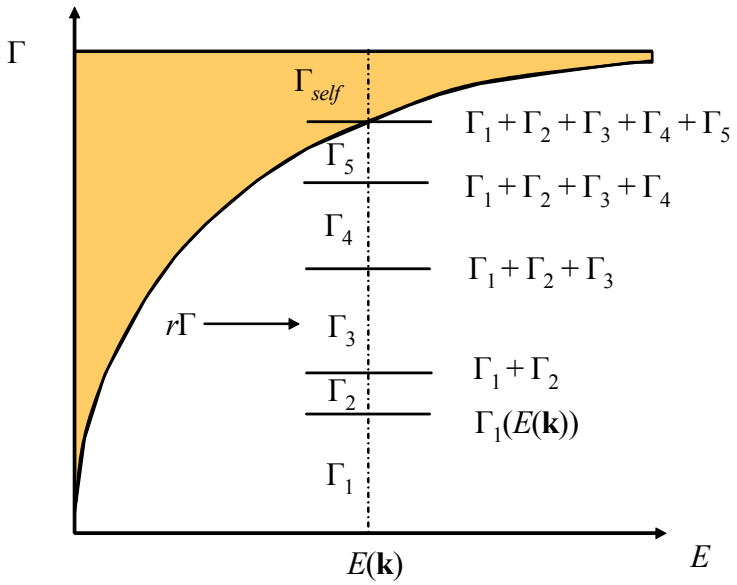

Figure 3. 1 The geometrical representation of scattering scheme.

If Γ is the total scattering rate, then we should compare $r\Gamma$ successively with the cumulative sums of the scattering rates. If $r\Gamma \leq \Gamma_1(\mathbf{k})$, then scattering mechanism Γ_1 is selected. If $\Gamma_1(\mathbf{k}) < r\Gamma \leq \Gamma_1(\mathbf{k}) + \Gamma_2(\mathbf{k})$, then scattering mechanism Γ_2 is selected. And so if $\Gamma_1(\mathbf{k}) + \Gamma_2(\mathbf{k}) + \ldots \Gamma_{n-1} < r\Gamma \leq \Gamma_1(\mathbf{k}) + \ldots \Gamma_n(\mathbf{k})$ then scattering mechanism Γ_n is selected as shown in Figure 3.1 [39].

3.1.3 The Final State after Scattering

Regarding the choice of the electron state after scattering, we have to consider both the energy conservation and the angular dependence of the particular scattering mechanism chosen. We can determine the final energy $E(\mathbf{k}')$ from

$$E(\mathbf{k}') = E(\mathbf{k}) \pm \hbar\omega \pm \Delta E, \tag{3.6}$$

where E is the energy at the end of the free flight, $\hbar\omega$ is the phonon energy (positive for absorption, negative for emission) and ΔE is the energy difference between valleys. ΔE is non zero for inter valley scattering (positive for transition to lower valley, negative for transition to upper valley). The final energy yields directly the absolute value of the momentum, but the determination of the direction of the momentum requires further generation of random numbers to determine the azimuthal angle φ and polar angle θ according to the angular dependence of the selected scattering mechanism.

For example, in the case of the isotropic character of the scattering, any state $\mathbf{k}'$ after scattering belonging to the energy conserving sphere has the same probability of occurrence (this is a good approximation for acoustic scattering (in a parabolic band) and inter valley scattering). That means the scattering probability to any particular state $\mathbf{k}'$ is

independent of θ and φ, where θ and φ are the polar and azimuthal angles relative to the after-scattering wave vector $\mathbf{k}'$ with respect to the before-scattering wave vector $\mathbf{k}$ (see Figure 3.2).

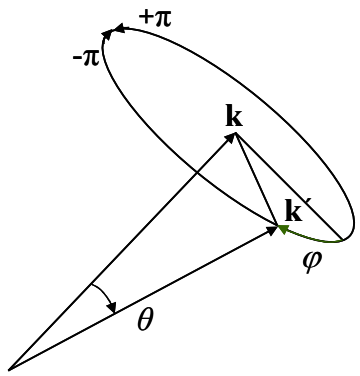

Figure 3.2 Geometry for the determination of the state after scattering.

So the angular dependence of scattering to all final states $\mathbf{k}'$ is

$$P(\theta,\varphi) \propto \sin\theta d\theta d\varphi \ . \tag{3.7}$$

P is the probability that the polar angles of $\mathbf{k}'$ with respect to any convenient directions will be contained in the intervals $d\theta$ and $d\varphi$. The provability to select a point on an element dS of the surface is equal to $dS/4\pi$ (assuming a sphere with radius 1, centered at the space location where the scattering occurs). Thus

$$\frac{dS}{4\pi} = \frac{\sin\theta d\theta d\varphi}{4\pi} = p(\theta,\varphi)d\theta d\varphi\,, \tag{3.8}$$

where $p(\theta,\ \varphi) = \sin\ \theta/4\pi$ is the density of probability. The separate densities of probability $p(\theta)$ and $p(\varphi)$ is given by,

$$p(\theta) = \int_0^{2\pi} p(\theta,\varphi)d\varphi = \frac{\sin\theta}{2},$$

$$p(\varphi) = \int_0^{\pi} p(\theta,\varphi)d\theta = \frac{1}{2\pi}\ , \tag{3.9}$$

because the two angles are independent, i.e., $p(\theta,\ \varphi) = p(\theta)p(\varphi)$. The angles can be obtained from two random numbers uniformly distributed between 0 and 1 as

$$r_1 = \int_0^{\theta} p(\theta')d\theta' = \frac{1-\cos\theta}{2},$$

$$r_2 = \int_0^{\varphi} p(\varphi')d\varphi' = \frac{\varphi}{2\pi}. \tag{3.10}$$

As the scattering randomizes the direction of the electron wave vector, θ and φ can be taken along the direction of the applied electric field **E** rather than of **k** (refer to Appendix A).

Usually, the angle φ after the scattering is chosen by $\varphi = 2\pi r$ using random number r. However, the angle θ depends on the nature of the scattering process, thus one needs to select θ according to the angular dependence $P(\theta)$ (refer to Sec. 2.4) of the scattering mechanism chosen by the direct method or the rejection technique [39]. Figure 3.3 shows angular dependence for screened electron-phonon scattering for the choice of the polar angle for the screened electron-phonon scattering given by

$$p(\cos\theta) = \frac{|\mathbf{k}|^2 + |\mathbf{k}'|^2 + 2|\mathbf{k}||\mathbf{k}'|\cos\theta}{\left[|\mathbf{k}|^2 + |\mathbf{k}'|^2 - 2|\mathbf{k}||\mathbf{k}'|\cos\theta + \beta^2\right]^2}. \tag{3.11}$$

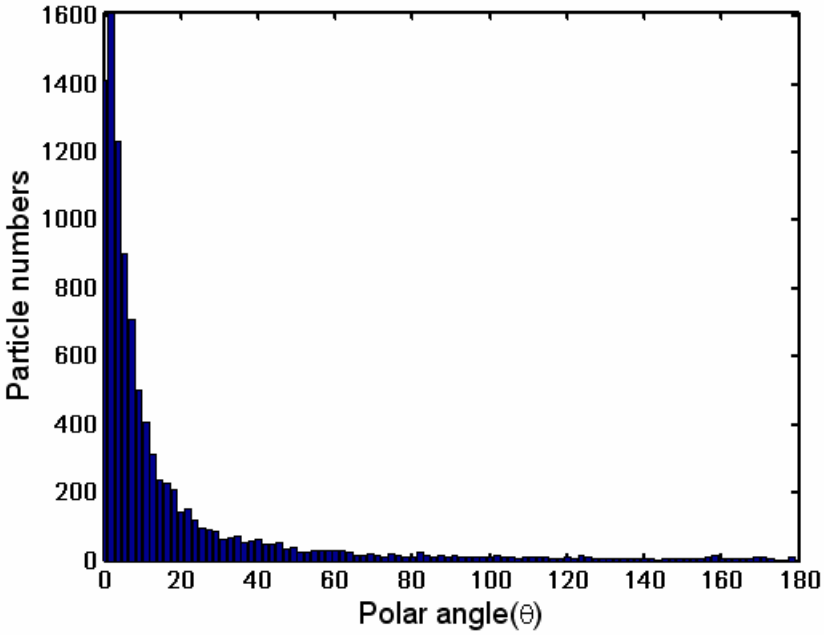

Figure 3.3 Angular dependence for screened electron-phonon scattering.

After the final state is determined, the distribution function can be determined from the trajectory of the particle in **k**-space and a quantity of interest can be calculated from this distribution function.

3.1.4 Ensemble Averaging Schemes

An ensemble Monte Carlo method can be visualized as N independent sequences of events. In Figure 3.4, the ensemble consists of N electrons, and the trajectory of the ith particle in the ensemble is plotted as a function of time. The circles represent scattering events that terminate the free flight times. At the observation time t, the ensemble average of a quantity A over the N particles of the system performed as follows

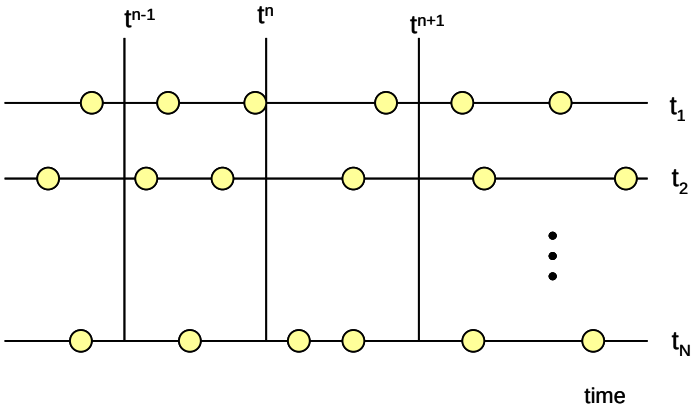

Figure 3.4 Ensemble average scheme: The time axis of the *i*th particle is represented by a straight horizontal line labeled by t_i, open circles indicate scattering events and t^n are observation points in time.

$$\langle A \rangle = \frac{1}{N} \sum_{i=1}^{N} A_i(t_i = t) . \tag{3.12}$$

For example, ensemble average velocity is illustrated schematically in Figure 3.5. Figure 3.5 shows the velocities of the electrons (i=1, 2, …, n) in the ensemble as a function of time during one sampling interval (0, t). The magnitude and direction of the velocities at each scattering event are schematically shown, with solid circles denoting real scatterings and open circles for self-scattering. The number of scattering events n may vary for each electron i in the ensemble. A time average of the velocities **v** over the sampling interval (0, t) is obtained for each electron by

$$\overline{\mathbf{v}}_i = \frac{1}{t_{total}} \sum_{k=1}^{m} \mathbf{v}_m t_m . \tag{3.13}$$

An ensemble average of those time-aveaged velocities at time t is obtained by

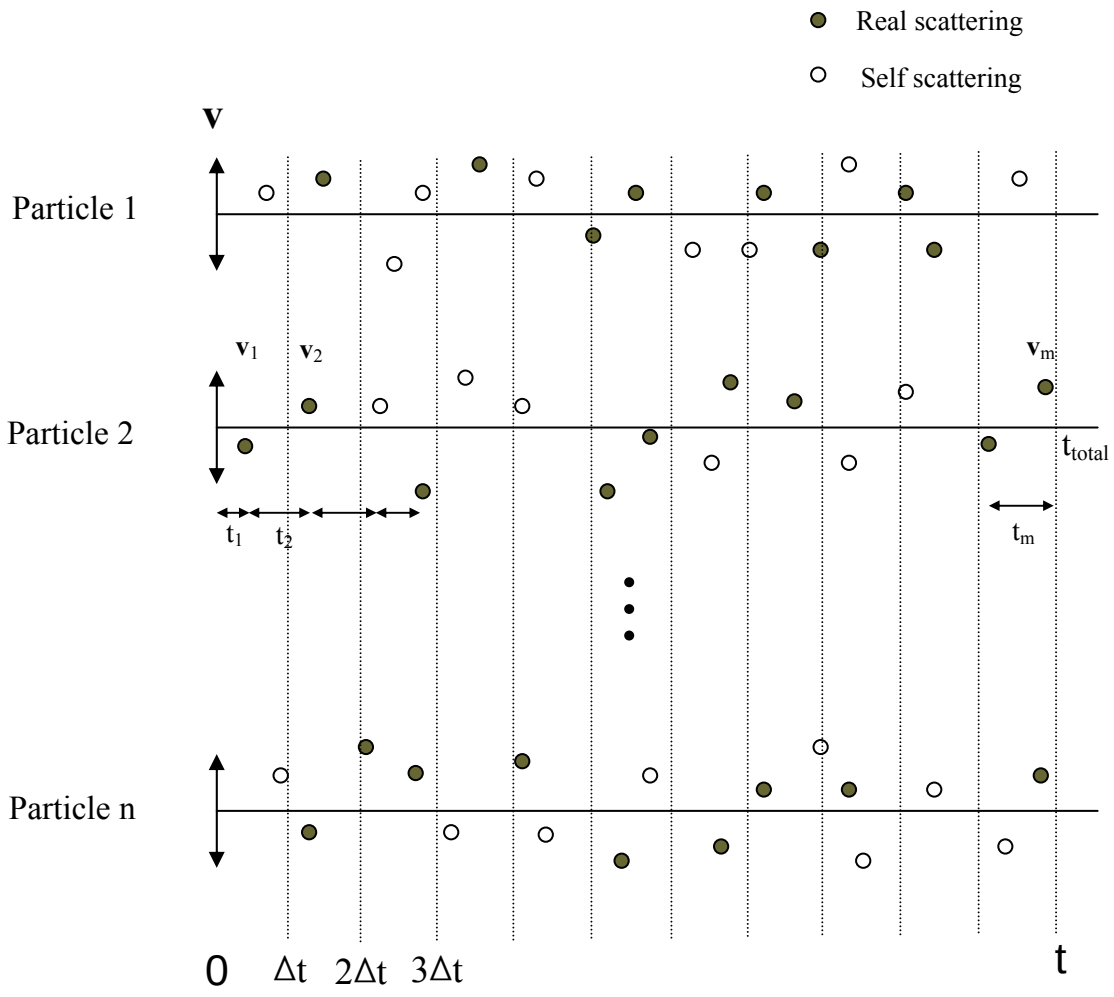

Figure 3.5 Interpretation of the ensemble average velocity.

$$\langle \mathbf{v} \rangle = \frac{1}{n} \sum_{i=1}^{n} \overline{\mathbf{v}_i} \,. \tag{3.14}$$

To obtain a single-valued steady-state velocity at a particular field strength, further averaging over the time in which the transport process becomes stationary is needed

$$\langle \mathbf{v} \rangle = \frac{1}{t_t - t_s} \int_{t_s}^{t_t} v(t) dt \,, \tag{3.15}$$

where t_s is the time when the process becomes stationary and t_t is the total simulation time.

3.2 Device Models

3.2.1 Initial Conditions

Initial conditions are essential parts of the Monte Carlo simulation process in many circumstances, such as small structure devices or nonequillibrium transport process, since Monte Carlo simulation is basically an evolutionary calculation. Initial conditions in Monte Carlo method are carrier distributions in **k-** and **r-**spaces as well as in the time domain. When a steady-state situation is simulated, the time of simulation must be long enough such that the initial conditions of the carrier motion do not influence the final results. On the other hand, when a simulation is made to study a transient phenomenon and a transport process in an inhomogeneous system, the distribution of the initial states of the ensemble for the particular physical situation under investigation must be taken into account, and the initial transient becomes an essential part of the results.

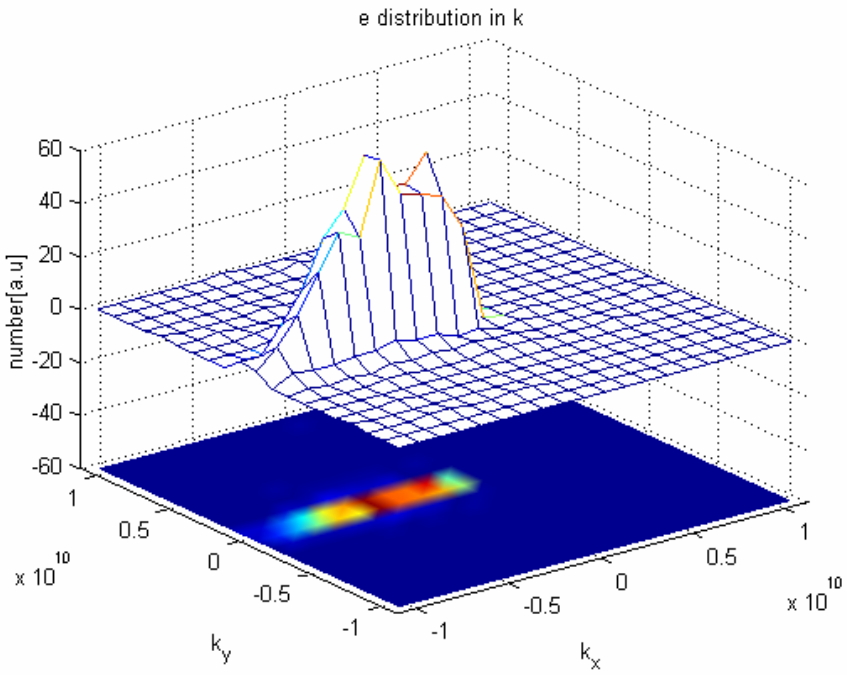

Figure 3.6. (a) The distribution functions of electron in **k**-space. (b) The direction of **k** in *x*-*y* plane. The *x, y*, and *z*-components of the wavevector are calculated using the |**k**|, the azimuthal angle φ and polar angle θ explained in section 3.1.3.

For a initial condition of **k**-space, The Maxwellian distribution which is given by Eq. 3.16 is implemented in Monte Carlo method.

$$f(\mathbf{p}) = \frac{n}{(2\pi m^* k_B T)^{3/2}} \exp(-\frac{\mathbf{p}^2}{2\pi m^* k_B T}), \tag{3.16}$$

where **p** is the carrier momentum.

When photoinjected carriers are simulated, the initial carrier distribution assumes a Gaussian energy distribution at the excess energy E_e with a spread of ΔE (ΔE is related to the pulse width Δt, $\Delta E \Delta t \sim h/2\pi$), the excess energy is related to the wavelength λ of the laser as $E_e = 1.24/\lambda(\text{in } \mu m) - E_g$ in eV. Once the energy distribution is determined the initial moment of the carrier is assumed to be randomized by Eq. 2.32 in Sec. 2.4.

For the initial conditions of **r**-space and time domain, a Gaussian pulse is assumed:

$$f(r) = \frac{1}{\sqrt{2\pi}\sigma} \exp(-r^2 / 2\sigma^2), \tag{3.17}$$

where σ is the standard deviation. For time domain, r is replaced with t.

3.2.2 Bulk Transport Properties in GaAs

The Monte Carlo method is used to examine the transport properties of bulk GaAs such as time evolution of the electron drift velocity, valley occupancies, and steady-state velocity-field characteristics by calculating carrier distribution in **k**-domain and at time t.

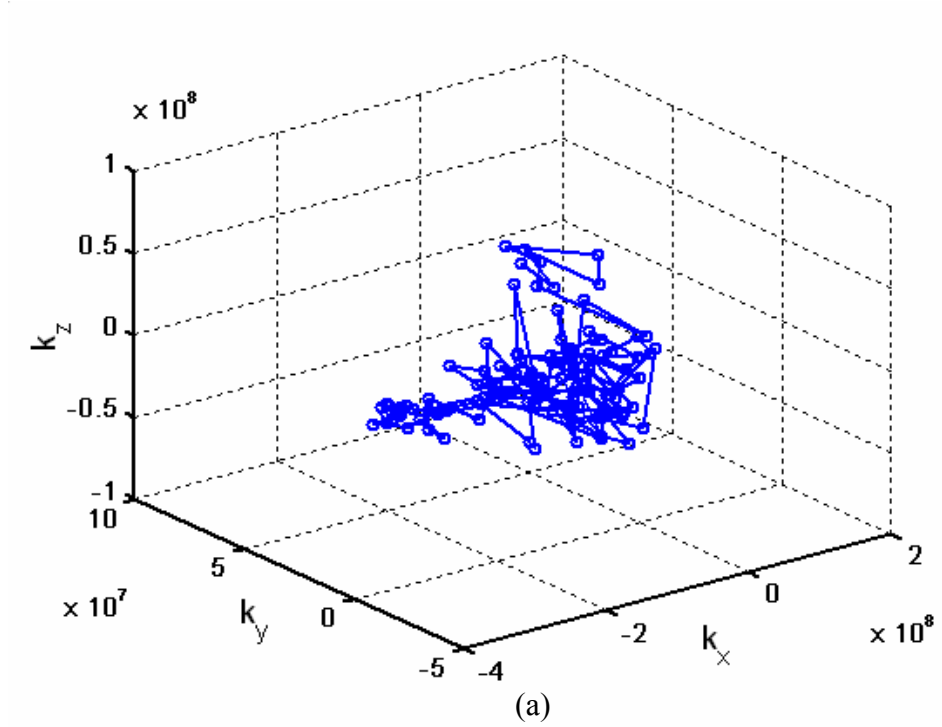

(a)

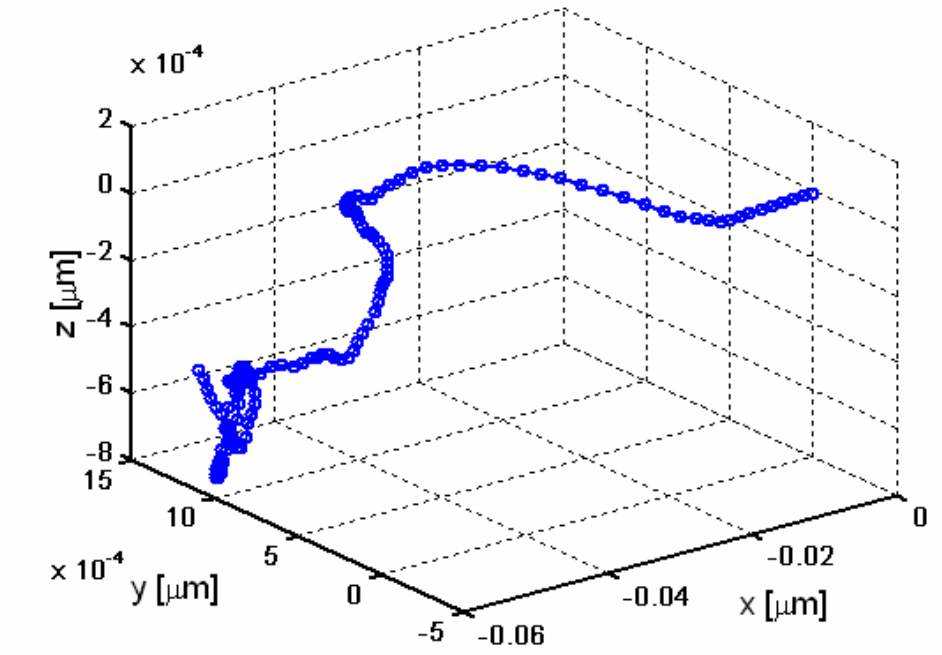

(b)

Figure 3.7 (a) The trajectory of the ensemble electron. (b) The path of the ensemble electron. The electrons are subject to an accelerating force oriented along the positive *x*-direction.

In the Monte-Carlo approach, first we specify the material parameters, the initial energy of the carriers, and the applied field, as well as which scattering mechanisms are active. The scattering mechanisms including various carrier-carrier and screened carrier-phonon interaction are calculated every time step of 1/300 ps depending on the evolving distribution function of the carriers, and then the dynamics of the electrons and holes are investigated using the Monte Carlo method coupled through the electron-hole interaction, which depends on their momentum distribution (see carrier-carrier scattering rates in Sec. 2.4) such as Figure 3.6. We use 10,000 superparticles over a time period of 5 ps, and the applied electric field is varied from 0.5 kV/cm to 20 kV/cm and assumed to be uniform and kept constant within one simulation run. Every estimate is refined with the time step, and then the ensemble averages of interest such as average velocity are computed. Figure 3.7 illustrates the principles of the method by showing the trajectory of an ensemble carrier in **k**-space and real space for1 ps.

3.2.2.1 Steady-State Response

Steady state transport in bulk GaAs is investigated at varing field strengths. The drift velocity-field relationship in bulk GaAs as shown in Figure 3.8(a) is the well known curve containing information on the scattering mechanism responsible for the negative differential mobility observed in GaAs. In the low field regime where the field is less than 4.5 kV/cm, there is a linear response of the system to the external field. But above this point, due to the intervalley scattering mechanisms, electrons start to transfer into upper valleys, as observed from valley occupancy in Figure 3.8(b), in which they slow down

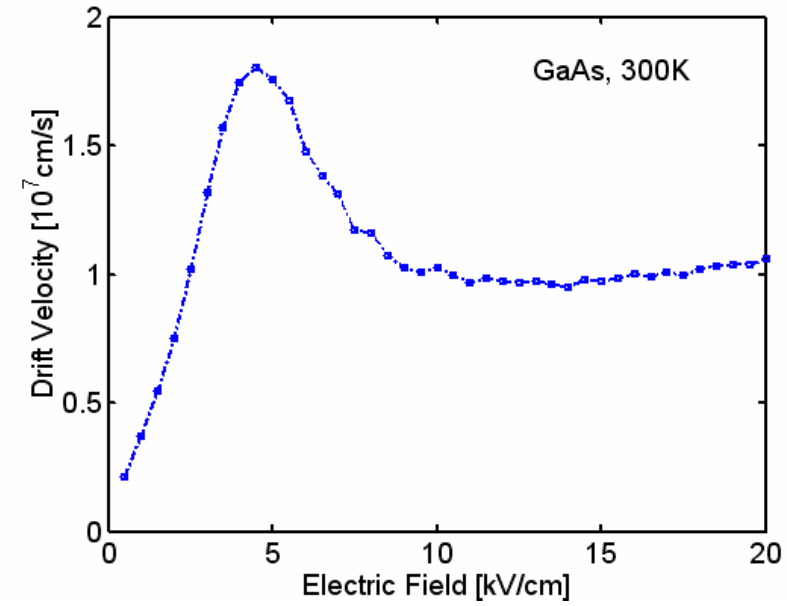

(a)

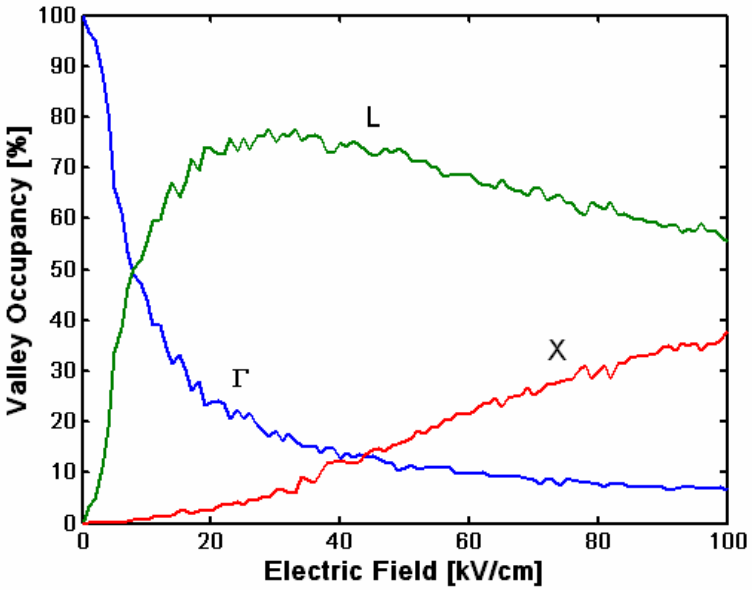

(b)

Figure 3.8 (a) Steady-state velocity vs field characteristic. (b)Valley occupancies vs field in GaAs at 300 K.

due to the much lager effective masses and they remain there as long as the field is greater than the critical value of about 4.5 kV/cm.

3.2.2.2 Transient Response

The electron transient dynamics are shown in Figure 3.9 (a). The substantial velocity overshoot is evident for electric field strengths in excess of 5kV/cm, while there in no overshoot at low fields. This is due to the fact that the energy relaxation time is longer than the momentum relaxation time. i.e., in high-field conditions, the electrons begin to accelerate before dissipating energy to the lattice, and have the possibility of reaching higher velocity values. This field strength around 5kV/cm corresponds to the peak value velocity in the velocity-field plot shown in Figure 3.8(a). We can know that the electric field for the onset of velocity overshoot is also the critical field in the velocity-field characteristics. At higher field, we can see transients take place at shorter times from the transport processes in the initial transients in different valleys showed in Figure 3.9(b). They have a fundamental period of around 1 ps for THz frequency electromagnetic radiation.

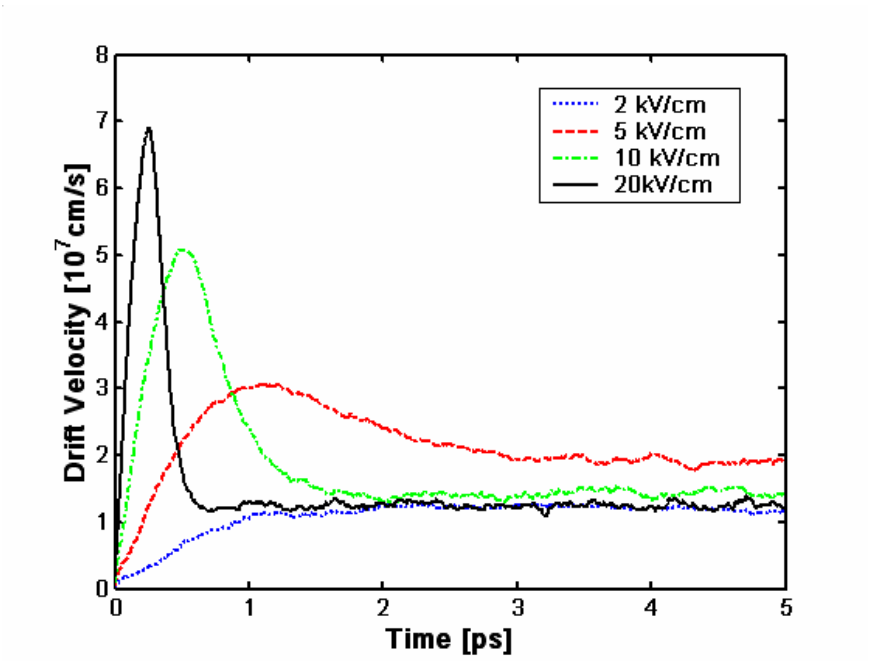

(a)

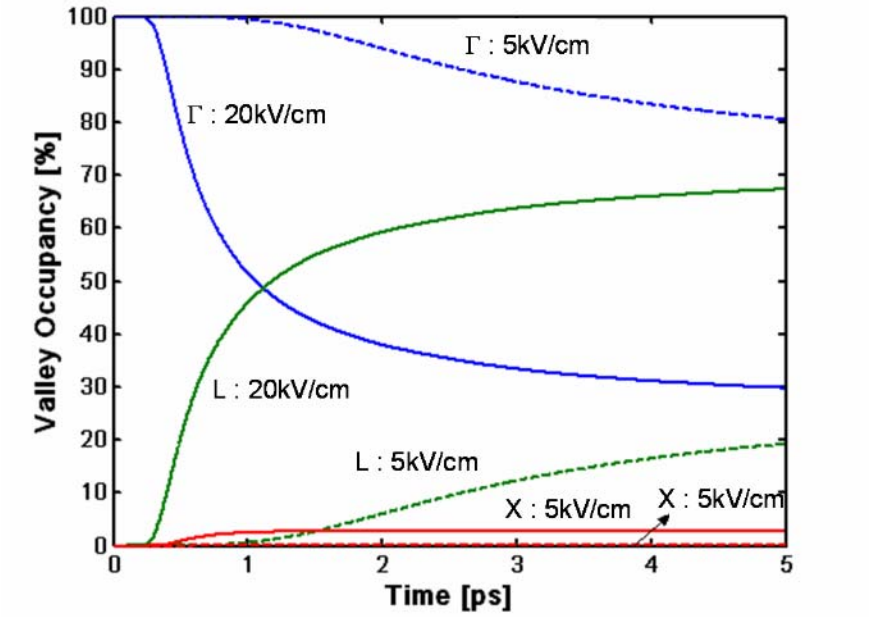

(b)

Figure 3.9 (a) Drift velocity vs time at electric field=2, 5, 10, and 20 kV/cm. (b) Valley occupancies vs time at electric field=5 and 20 kV/cm.

3.3 Self-Consistent Poisson solver

3.3.1 Iteration method

The Poisson equation describes the variation of the potential ϕ due to the local charge density ρ given by

$$\frac{\partial^2 \phi(z)}{\partial z^2} = -\frac{\rho(z)}{\varepsilon}. \tag{3.18}$$

The Poisson equation can be solved by simple iteration method which is well suited for calculation. A portion of a region containing a two-dimensional potential field, divided into squares of side h as shown in Figure 3.10. The potential V_o can be obtained from

$$\frac{\partial^2 V}{\partial x^2} + \frac{\partial^2 V}{\partial y^2} \cong \frac{V_1 + V_2 + V_3 + V_4 - 4V_0}{h^2} = -\frac{\rho}{\varepsilon}. \tag{3.19}$$

where h is the spatial bin width.

The iterative method determines the potential at the corner of every square

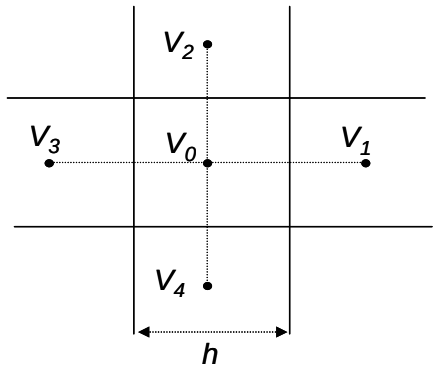

Figure 3. 10 A portion of a region containing a two-dimensional potential field.

subdivision in turn, and then the process is repeated over the entire region as many times as is in necessary until the values no longer change. The iteration is continued until the difference between successive traverses is less than 10^{-5}. The electric field distribution is then obtained from the calculated potential distribution using forward difference formula as

$$E_{field} = (\phi_i - \phi_{i-1})/h\,. \tag{3.20}$$

Figure 3.11 shows the electric field distribution obtained from the electrostatic potential ϕ determined by the Poisson equation self-consistently using the iteration method for 20×100 grid with the left side at a potential of 100 V, the right side at zero potential, and no charge in the interior. One can see an analysis region to avoid the effect of infinitesimal gap (A potential of 50 V, which is the average of 0 and 100 V, is set for boundary condition).

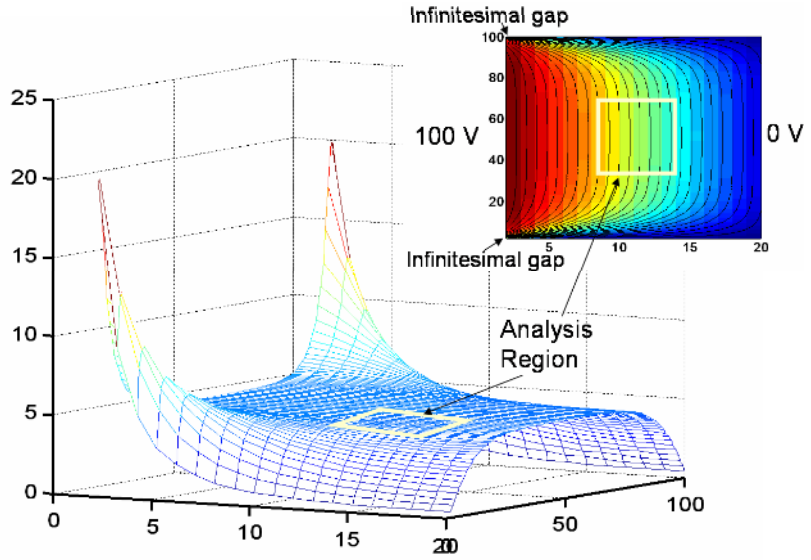

Figure 3. 11 The electric-field distribution for 20×100 grids. One can see analysis region to avoid the effect of infinitesimal gap.

3.2.2 Charge Assignment Schemes

The Monte Carlo method gives the time-dependent solution of the Boltzmann transport equation and the Poisson equation. Because of the discretization scheme in a particle model, each particle in the ensemble represents a certain amount of charge for the real system. During a particle-mesh calculation, those space charges are assigned to the mesh points and represent a cloud of electrons only for the purpose of solving the Poisson's field equation. For all other purposes, each particle has the charge q of the real carriers and represents a classical particle on the Monte Carlo method. A better approximation to the charge assignment can be obtained by the Cloud-in-cell (CIC) scheme [47], which involves the two nearest neighbors as shown in Figure 3.12.

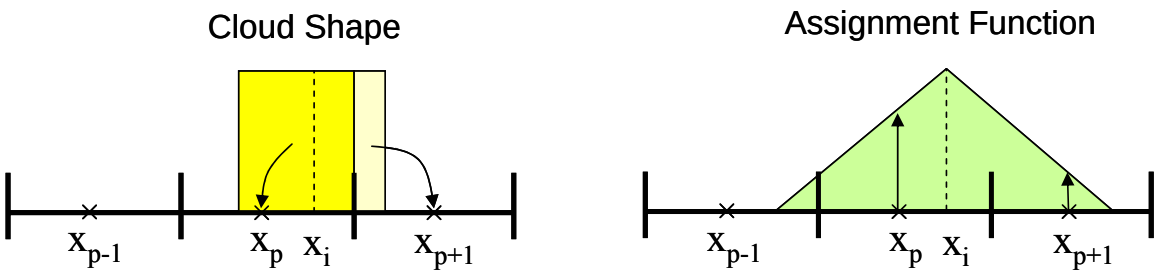

Figure 3. 12 Interpretation of charge assignment in CIC scheme. The assignment function is the convolution of the cloud shape with a top hat.

In the CIC scheme, the cloud shape is represented by a piece-wise constant function that spans the width of the cell. Instead of assigning all the charge of a particle to its nearest grid point, CIC scheme assigns a portion of the charge, which is proportional to the fraction of the cloud in a neighboring cell, to its two nearest grid points. This is

equivalent to using an assignment function of the following Eqs. (3.21) and (3.22). The mesh-defined charge density for an ensemble of N charged particles is given by

$$\rho(x_p) = \frac{q}{V_{cell}} \sum_{i=1}^{N} W(x_i - x_p), \tag{3.21}$$

where W is the assignment function defined by

$$W(r) = \begin{cases} 1\left(1 - \frac{|x|}{h}\right)\left(1 - \frac{|y|}{h}\right) & for \quad |x - x_p| \le h \\ 0 & \text{otherwise} \end{cases}, \tag{3.22}$$

where h is the spatial bin separation. This assignment function is the convolution of the cloud shape in Figure 3.12 with a top hat. Thus, charges are assigned to the four nearest neighbor grid points.

CHAPTER 4

PHOTOEXCITATION AND TERAHERTZ RESPONSE

In the previous chapter, we have detailed the transport theory and the fundamental aspects of the numerical approach techniques. In this chapter, we present our numerical investigations on photoexcitation and THz response in photoconductive GaAs-based THz sources. The main objective of this work is to investigate the interplay of the carrier dynamics and screening, which is the main limitation of THz output power, for optimizing THz generation. In this chapter, we assume that due to the finite conductivity of the electrodes, they do not have time to recharge on ultrafast timescales following photoexcitation, and a holistic view of THz generation is adopted.

In Sec. 4.1, spatially resolved carrier dynamics in photoconductive THz source are investigated. In Sec. 4.2, we detail the Coulomb and radiation parts of the electromagnetic field subsequent to the photoexcited carriers in THz emitter. In Sec. 4.3, the combined effects of large trap-enhanced fields (TEF) near the anode in semi-insulating (SI) photoconductors and enhanced THz emission by spatially nonuniform optical illumination are investigated.

4.1 Spatially Resolved Carrier Dynamics

4.1.1 The Spatial Distribution of Photoexcited Carriers

For higher average carrier densities, as the electrons and holes move apart, a screening field builds up following which this screening affects the spatio-temporal

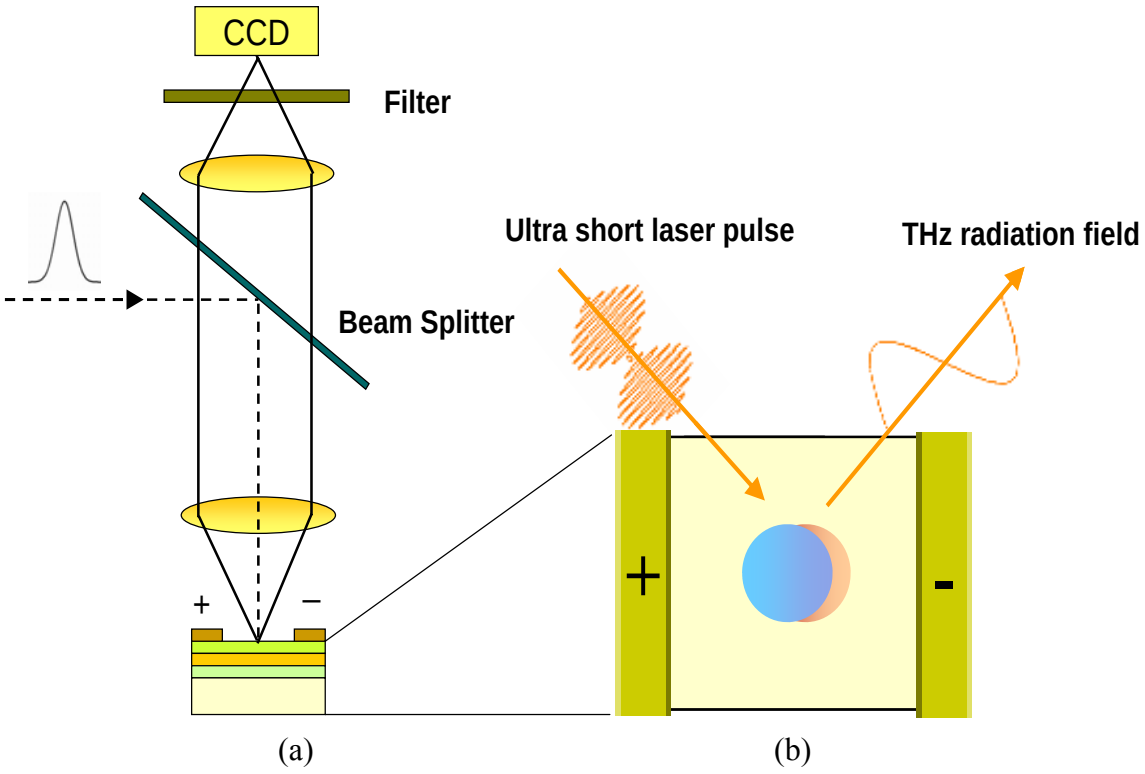

Figure 4.1 (a) Experimental setup [48]. (b) Schematic diagram of electron (left circle) and hole (right circle) distributions in the biased photoconductor after femtosecond laser excitation.

dynamics. We show an experimental setup of spatially resolved measurements [46-48] for understanding the mechanism of the devices in Figure 4.1(a). In this specific case, the luminescence associated with electron-hole recombination was imaged onto a charge coupled device (CCD) camera to study the spatio-dynamics of the photogenerated carrier distributions in a photoconductive switch.

If the optical excitation is assumed to be Gaussian both temporally and spatially, the electron-hole separation can be expected to contribute to the generation of THz radiation depending on different regions of the device since the carrier density decreases from the center of the excitation spot to its edges. Figure 4.2 shows the experimental spatially resolved differential luminescence as the effect of spatial pattern formation of optically excited carriers [48-51]. The differential luminescence pattern indicates the spatial overlap of the electron and hole distributions after excitation. For example, as the

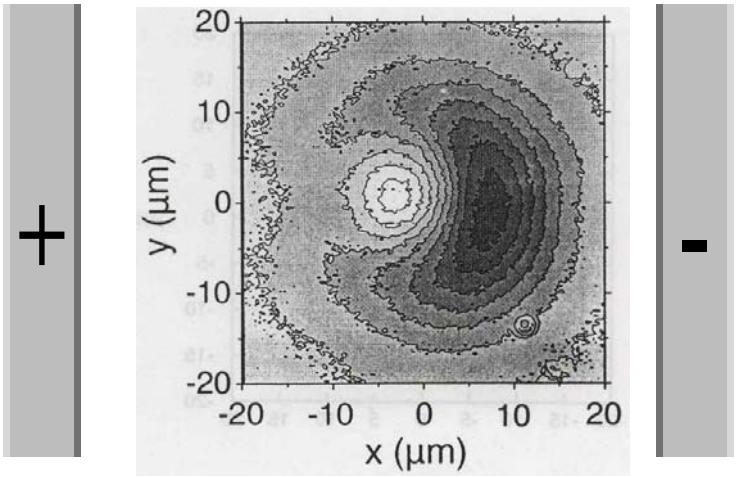

Figure 4. 2 Experimental spatially resolved differential luminescence for a bias field of 4 kV/cm and spatial carrier density of 7×10^{11} cm^{-2}. The dark colors represent stronger normalized luminescence(reduced) at zero bias, the light colors represent stronger normalized luminescence(enhanced) at finite bias and the grey tone in the corners represents the zero level [48,50].

electrons move faster than the holes, the region where the biased luminescence has a stronger normalized contribution than the unbiased case is closer to the anode. One can see the region of reduced luminescence surrounding the region of enhanced luminescence due to the spatial screening variations in the *y*-direction depending on the carrier density; otherwise the dark region does not surround the white region. This means that the density dependence of screening combined with the different spatial distribution of photoexcited carriers leads to substantial spatial variations of the carrier dynamics in photoconductive switches. As a consequence, spatial effects need to be accounted for in the optimization of photoconductor as THz emitters.

4.1.2 The Spatially Patterned Excitation

In the following, we consider a GaAs-based photoconductive source as shown in Figure 4.3. Patterned on top are assumed to be two infinitely long parallel electrodes,

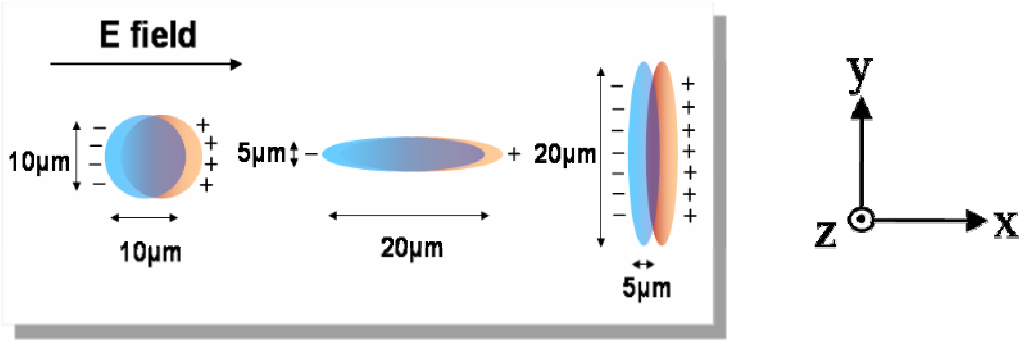

Figure 4.3 Schematic diagram of electron (–, left circle) and hole (+, right circle) distributions in the biased photoconductor after femtosecond laser excitation: (a) a round excitation spot, (b) an elliptical excitation spot with its major axis parallel to the direction of the bias field, (c) an elliptical excitation spot with its major axis perpendicular to the direction of the bias field.

between which is the photoconductive gap. This geometry enables us to approximate the carrier transport as two-dimensional. Various laser spot shapes are incident upon this gap as shown in Figure 4.3 that act as carrier sources within the Monte-Carlo simulation, and the optical excitation is assumed to be Gaussian both temporally and spatially.

The performance of the THz generation depends on the temporal shape of the photoinduced current pulses, and this shape is determined in part by transient velocity overshoot and the screening due to the optically excited electron and hole distributions—space-charge screening as well as dynamic screening associated with the back action of the retarded electromagnetic field [15,48] (the details are discussed in the next section. For the excitation-spot size in Figure 4.3, space-charge screening is dominant due to the relatively small aperture size (spatial spot sizes are ~10 μm)). Most of the THz power is generated during the initial ballistic acceleration of the photoexcited carriers. Thus, in order to describe the spatio-temporal response of electrons on a subpicosecond timescale, we compute the carrier distribution function by solving the Boltzmann transport equation from the Monte-Carlo method as mentioned in previous chapters.

In this Section, we report on our numerical investigations of the generation of THz radiation from photoconductors driven by ultrafast optical pulses with various incident spot shapes through spatially resolved Monte Carlo simulations coupled with a self-consistent Poisson solver. Monte Carlo techniques have been applied recently to understand spatiotemporal aspects of photoconductive THz generation [52-54], while drift diffusion-Poisson simulations of broad-area photoconductors were carried out in Refs. 49 and 51.

4.1.2.1 Approach

In this section, we describe the approach to the detailed Monte Carlo-Possion solver. After excitation by an ultrafast laser pulse, the photoexcited carriers are accelerated to the electrodes by the bias field. The carrier free flight is governed by the classical laws of motion and is terminated after a few femtoseconds at time t_f selected by random from the function $t_f = -\ln r/\Gamma$, where r is random number with a uniform distribution between 0 and 1, and Γ is the total scattering rate. This basic time step is tied to the duration of the carrier free flight between successive scatterings. At the end of each free flight, the electron is scattered to a new state according to the probability of the scattering process determined by a random number *r*. The scattering mechanisms and the final state (the modulus of the momentum and the scattering angle) of a carrier are selected at the end of the flight accounting for acoustic-phonon scattering, ionized-impurity scattering, intervally scattering, carrier-carrier scattering and screened carrier-phonon scattering. We calculate the screening length self-consistently, which affects the scattering rates of the ionized impurity, carrier-carrier, and screened carrier-phonon interactions using the evolving built-in distribution function, and then update the scattering-rate table for each time step. We include the three nonparabolic valleys Γ, L, and X within the conduction-band and a parabolic heavy- and light-hole band. When a photoconductor is excited by high peak-fluence optical pulses, the accelerated motion of the electrons by the bias field results in THz radiation (the holes being heavier play an important though indirect role), but at the same time, as the carriers undergo their spatial dynamics in the bias field, they partially screen out the bias. The origins of the screening consist of the radiation field and instantaneous space charge-screening, which contribute

to the collapse of the total electric field acting on the carriers at high carrier density. In order to consider these screening effects, we obtain the retarded THz electromagnetic field due to the accelerating carriers [55] as well as longitudinal space-charge screening that builds up as electrons and holes move apart in the bias. The Poisson equation [19] describes the variation of the potential ϕ due to the local charge density ρ given in two-dimensions by the discretized form

$$\frac{\phi_{i-1,j}+\phi_{i+1,j}+\phi_{i,j-1}+\phi_{i,j+1}-4\phi_{i,j}}{h^2}=-\rho_{i,j}/\varepsilon\varepsilon_0, \tag{4.1}$$

where h is the spatial grid width, ε is the dielectric constant of the photoconductor, ε_0 is the permittivity of freespace, and ρ can be expressed as

$$\rho_{i,j}=q_{sc}(p_{i,j}-n_{i,j}+N_D-N_A), \tag{4.2}$$

where q_{sc} is the supercharge represents a subpopulation of the carriers in the real device. n and p are electron and hole concentrations, N_D and N_A are donor and acceptor densities, respectively. In a Monte Carlo simulation n and p are obtained from the ensemble average of the charges assigned to the mesh points during the simulation (see Sec. 3.3); thus, for the static screening this ensemble number is counted inside every grid before free flight during the simulation.

4.1.2.2 Transport Properties of Photoexcited Carriers

First, for the transport properties of photoexcited carriers in the bias field, we consider a GaAs-based photoconductor laterally biased at 5 kV/cm and 40 kV/cm excited

by a 75-fs Gaussian-envelope optical pulse spectrally centered at 800 nm with a repetition rate of 76 MHz for peak excited carrier densities $5\times10^{16}cm^{-3}$ and $10^{17}cm^{-3}$. In the Monte-Carlo approach, first we specify the material parameters, the initial energy of the carriers, the optical pulse shape and duration, and the applied field, as well as which scattering mechanisms are active. The various carrier-carrier and screened carrier-phonon interaction are calculated every time step of 1/300 ps depending on the evolving distribution function of the carriers, and then the dynamics of the electrons and holes are investigated using the Monte Carlo method coupled through the electron-hole interaction, which depends on their momentum distribution. We use 14000 superparticles whose distribution is adjusted to be proportional to the temporal and spatial shape of the optical pulse and 2500 gridpoints. Every estimate is refined with the time step and then the ensemble averages of interest such as average velocity are computed.

The transient velocity of the electrons at a photoexcited carrier density level of 5×10^{16} cm^{-3} for an applied field of 5 kV/cm and relative electron occupation of the valleys depending on optical excitation spot shapes are shown in Figure 4.4. From Figure 4.4(b), we can see most electrons are still in the Γ valley during the first few hundred femtoseconds. Thus, the decrease of the drift velocity in Figure 4.4(a) originates primarily from space-charge screening due to the relatively small aperture size (spatial spot sizes are ~10 μm) [15,22,23]. The screening underlying this effect depends on the spatial carrier distribution. We observe a much stronger screening field for a line focus perpendicular to the direction of the bias field In Figure 4.4(a). As the

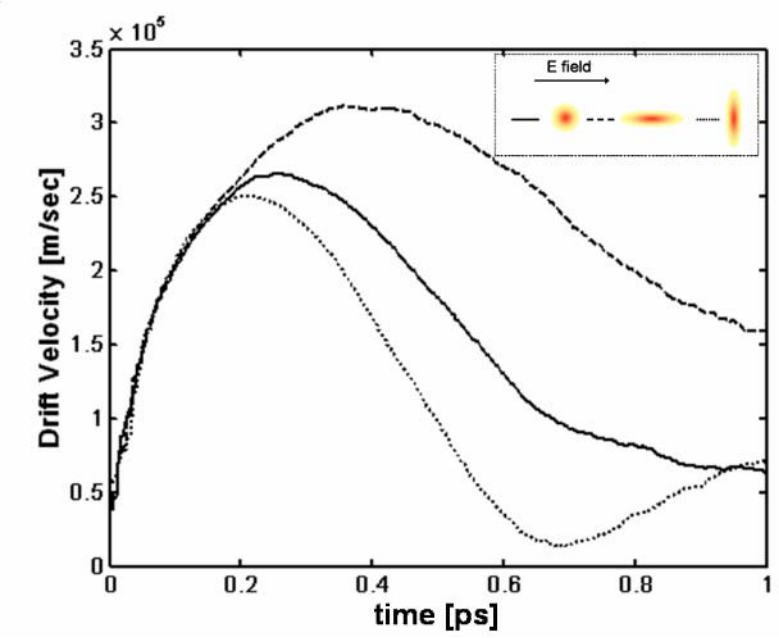

(a)

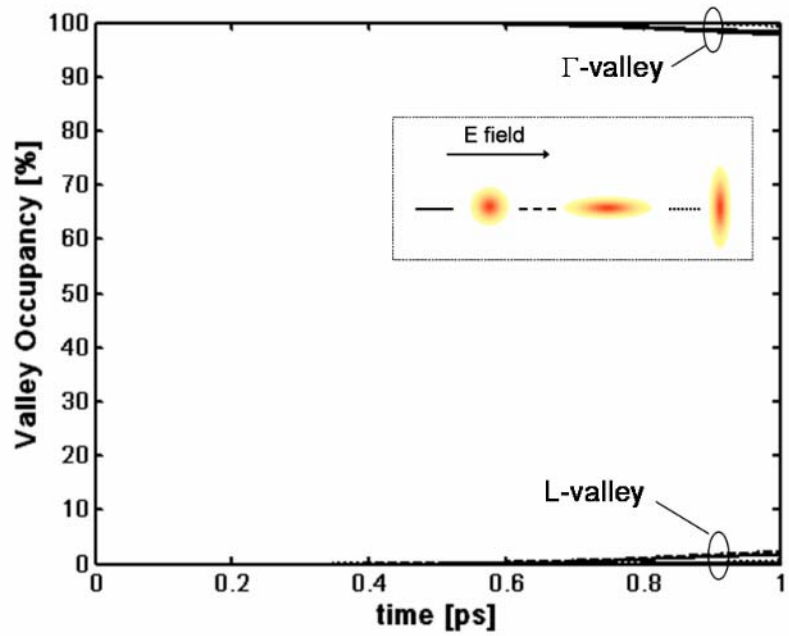

(b)

Figure 4. 4 (a) Drift velocity of photoexcited electrons versus time depending on optical excitation spot shapes. (b) Relative electron occupation of the Γ, L, and X-valleys versus time at 300 K, n=5×10^{16}cm^{-3}, and 5 kV/cm applied bias field.

electrons and holes drift in opposite directions, one obtains larger net positive and negative space charge than for other case as shown in Figure 4.3(c). One sees that the rapid development of the space charge acts as a brake on the electron velocity. In the case when the major axis of the elliptical spot is parallel to the direction of the bias field, however, the screening is much less severe, and thus the electron velocity is able to increase further.

In a high bias field, meanwhile, the transport of the photoexcited electrons is more complicated. The velocity of the electrons as a function of time and valley occupancy with different optical spot shapes are plotted in Figure 4.5 for an applied field of 40 kV/cm at an excitation level of 10^{17} cm^{-3}. For all the optical spot shapes, the excited electrons respond rapidly to the electric field and the velocity increases until a peak value of about 7×10^{5} m/s; however, these velocities decrease in a different fashion due to the transfer of the electrons to the upper valleys and screening [c.f. Figure 4.4(a)] depending on the optical spot shape. With the spot's major axis perpendicular to the direction of the bias field, the fraction of electrons that transfer to the upper valleys is reduced; in addition, this spot shape leads to a rapid reduction of the electron velocity, reaching a minimum at 0.4 ps at which time about 40 % of the electrons are in the upper valleys (L-valley: 38%, X-valley: 2%) as shown in Figure 4.5(b). This phenomenon occurs due to the interplay of transient velocity overshoot and the strong-space charge screening from the larger net positive and negative space charge as shown in Figure 4.3(c). Since this screening field contributes to the collapse of the bias field after the complete generation of photocarriers (~ 75fs FWHM optical pulse duration), the electrons do not acquire

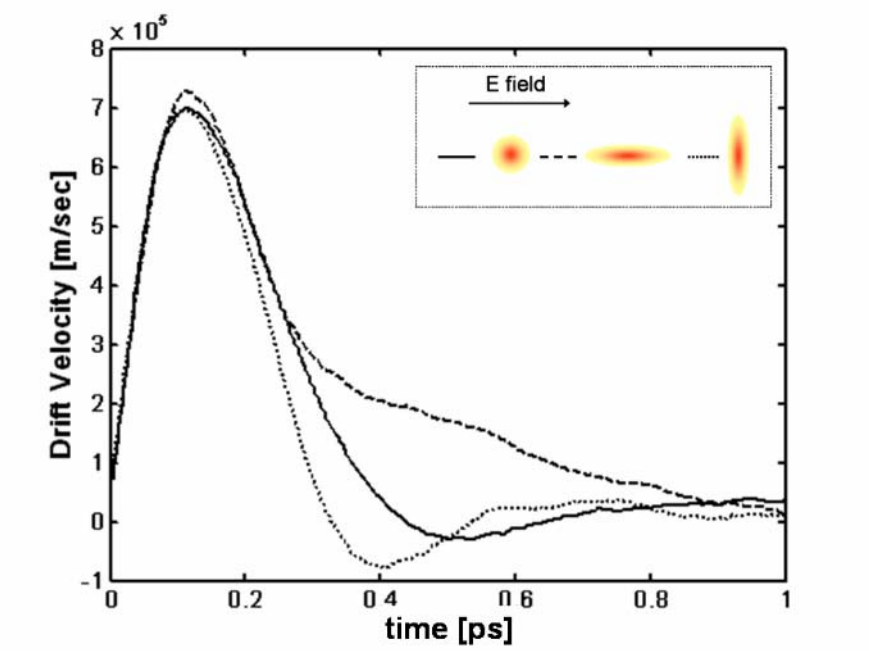

(a)

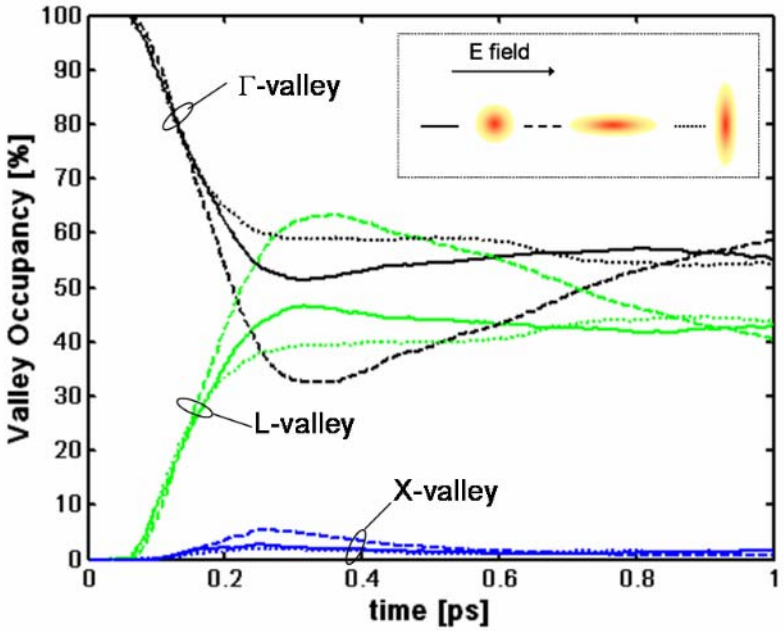

(b)

Figure 4. 5 (a) Drift velocity of photoexcited electrons versus time depending on optical excitation spot shapes (b) Relative electrons occupation of Γ, L, and X-valleys versus time at 300 K, n=10^{17}cm^{-3}, and 40 kV/cm applied bias field.

sufficient energy to access the upper valleys, as a rapid reduction in their velocity due to the strong space-charge screening ensues.

By contrast, with the excitation-spot major axis parallel to the direction of the bias field, the electrons reach a peak velocity and then gradually decrease to a saturation velocity as the electrons gradually transfer to the upper valleys. In this case, space-charge screening is relatively weak, with small net positive and negative space charges developing as in Figure 4.3(b), permitting relatively more carriers to be transferred to the upper valleys (L-valley: 65%, X-valley: 5%).

4.1.2.1 Enhancement of THz Radiation

The difference in the resulting electron velocity and acceleration is manifested in the optimization of THz radiation, since the total power radiated by the accelerated photocarriers is given by [55]

$$P \cong \frac{1}{6\pi\varepsilon_0}\frac{N^2 {q_{sc}}^2 \langle a \rangle^2}{c^3}, \tag{4.3}$$

where N is the number of carriers in the ensemble, and $\langle a \rangle$ are the retarded ensemble averages of the acceleration. Figure 4.6 shows the peak THz power obtained from Eq. (4.3) as a function of photoexcited carrier density for different incident spot shapes excited by a 75 fs optical pulse with a 40 kV/cm applied bias field. If the optical power is increased, the associated increase in the number of photoexcited carriers enhances the screening field, which suppresses the carrier acceleration within the first several hundred femtoseconds. This in turn leads to a saturation of the peak THz power in time domain. For an elliptical excitation spot with its major axis parallel to the direction of the

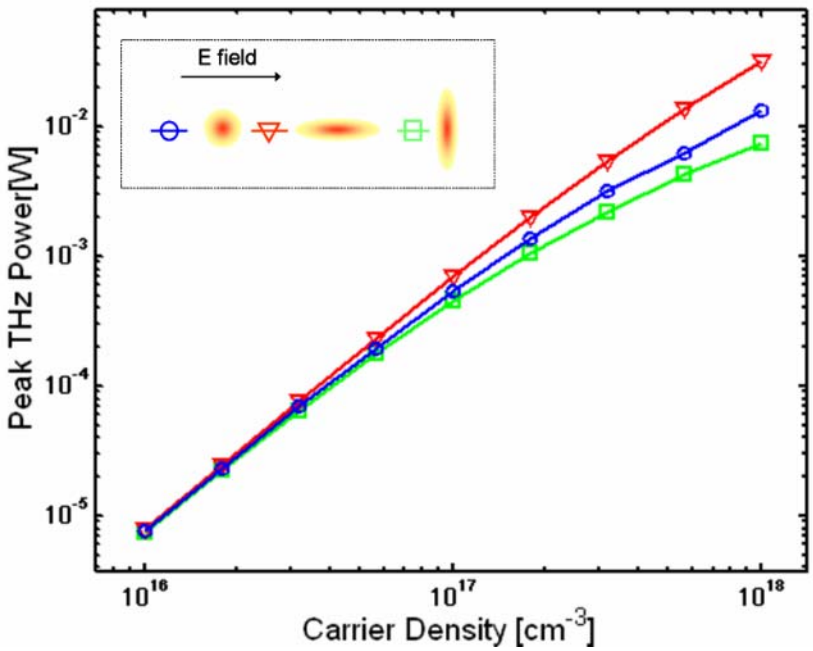

Figure 4. 6 The THz radiation peak power as a function of photoexcited carrier density for different spot shape excited by a 75 fs temporal and spatial Gaussian optical pulse at 40 kV/cm applied bias field.

bias field, however, the instantaneous THz power remains essentially linear with input optical power due to the relatively weak space-charge screening and results in a larger peak power than for the circular spot shape, whereas an elliptical excitation spot with its major axis perpendicular to the direction of the bias field leads to saturation of the peak power due to the strong space charge screening, as seen in Figures 4.4 and 4.6.

In this section, we have fixed the peak excitation density to be the same value in all cases, and have not accounted for the strongly inhomogeneous bias field that is present, for example, near the anode in semi-insulating (SI) GaAs photoconductive THz sources [56]. (Details of SI-GaA are discussed in Sec. 4.3.)

Our simulations demonstrate that considerable control of the emitted THz spectrum can be attained by judiciously choosing the optical excitation spot shape on the

photoconductor, since the carrier dynamics (such as photo-excited carrier drift velocity) that provide the source of the THz radiation are strongly affected by the ensuing space-charge screening. In particular, for a given initial photoexcited carrier density, by employing an elliptical excitation spot with its major axis parallel to the direction of the bias field, one can largely suppress the effects of screening that tend to cause the THz output strength to be saturated [57,58].

4.2 THz Radiation Field from Photoconductive THz Emitter

4.2.1 Retarded THz Radiation Field

When a photoconductor is excited by high peak-fluence optical pulses, the accelerated motion of the carriers by the bias field results in the emission of THz radiation. To explore the THz radiation field associated with the photoexcited carriers, we divide the carrier densities spatially into groups of moving charges, and from these, compute the emitted electric fields. The electric field due to a point charge q moving with velocity **v** and acceleration **a** is given by [55,59,60]

$$\mathbf{E} = \mathbf{E}_v + \mathbf{E}_a = \frac{q}{4\pi\varepsilon}\left(\frac{1}{\left|1-\hat{R}\cdot\mathbf{v}/c\right|^3}\left\{ \frac{(1-v^2/c^2)(\hat{R}-\mathbf{v}/c)}{R^2} + \frac{\hat{R}\times[(\hat{R}-\mathbf{v}/c)\times\mathbf{a}]}{c^2 R} \right\} \right)_{tr}, \qquad (4.4)$$

where ε is the permittivity, c is the speed of light in photoconductor (i.e., in the background dielectric), and **R** is the position vector directed from charge q to the point of observation. **R**, **v**, and **a** are evaluated at the retarded time t_r=t-R/c where t is the present

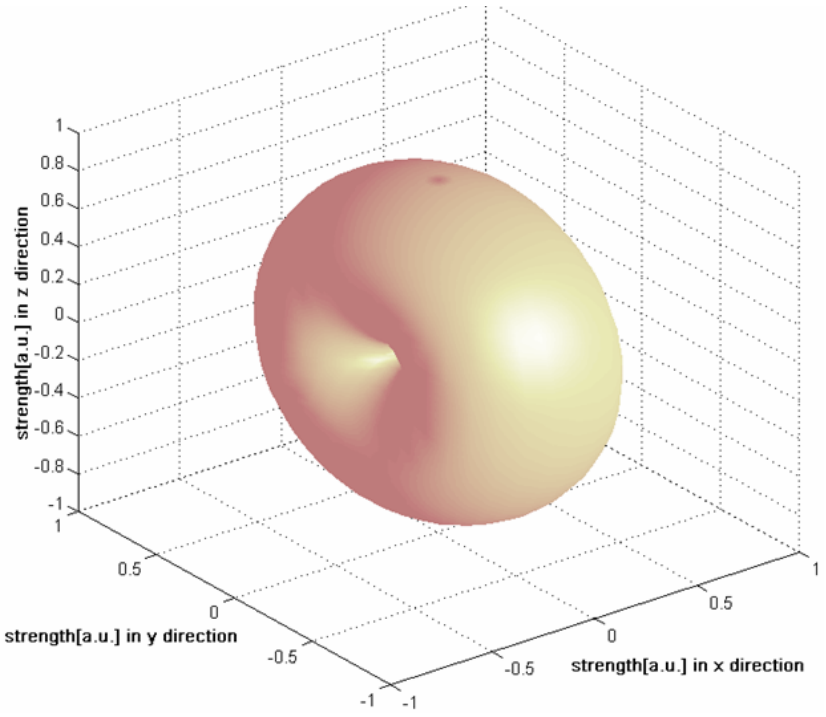

(a)

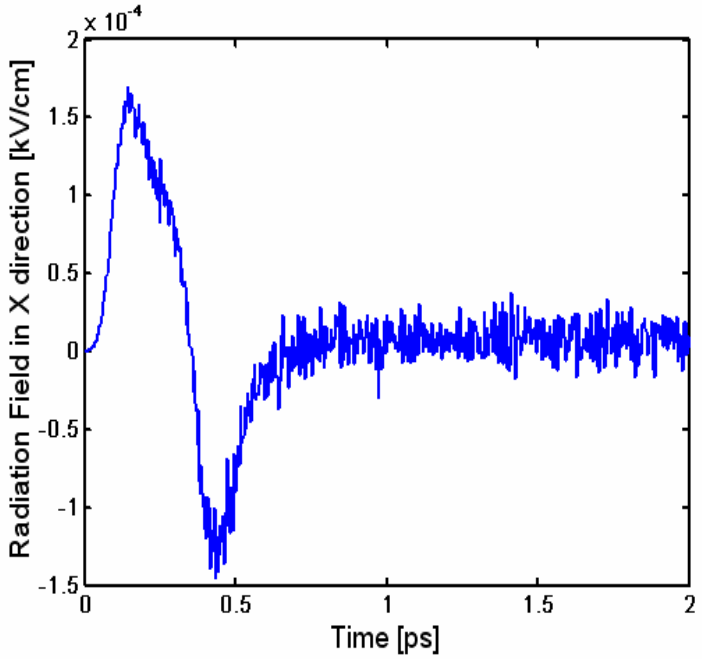

(b)

Figure 4. 7 (a) Far field pattern of THz radiation. (b) THz radiation field vs time.

time for which **E** is evaluated. The magnitude and direction of the electric field at each location is simply the vector sum of the electric-field vectors for each individual charge. In order to obtain the transport properties (**R**, **v**, and **a**) of the photoexcited carriers, we solved the Boltzmann transport equations employing the Monte Carlo method as mentioned in Chpater 3. The electric field in Eq. (4.4) clearly contains the velocity field, $\mathbf{E}_v$ proportional to R^{-2} as well as the acceleration field $\mathbf{E}_a$ proportional to R^{-1}. For the far field as shown in Figure 4.7(a), the distance R can always be made large enough that the velocity field is negligible and the acceleration field predominates and it falls off as R^{-1}. Thus we find that the radiation field is proportional to the acceleration as shown in Figure 4.7(b). Figure 4.7(a) shows a snapshot in time of the far field amplitude pattern, with the familiar omni-directional shape of the electric dipole, since photo-induced electrons and holes make net negative charges and positive charges.

For the total power radiated by the accelerating carriers we consider the Poynting vector for retarded electromagnetic fields. This is the energy per unit time passing through a unit area of a spherical surface surrounding the THz photoconductive source, such as the sphere mentioned above, that is, this is the power density on the sphere at time t. After we integrate the power per unit solid angle in direction **R** over all solid angles, the total power radiated becomes [55]

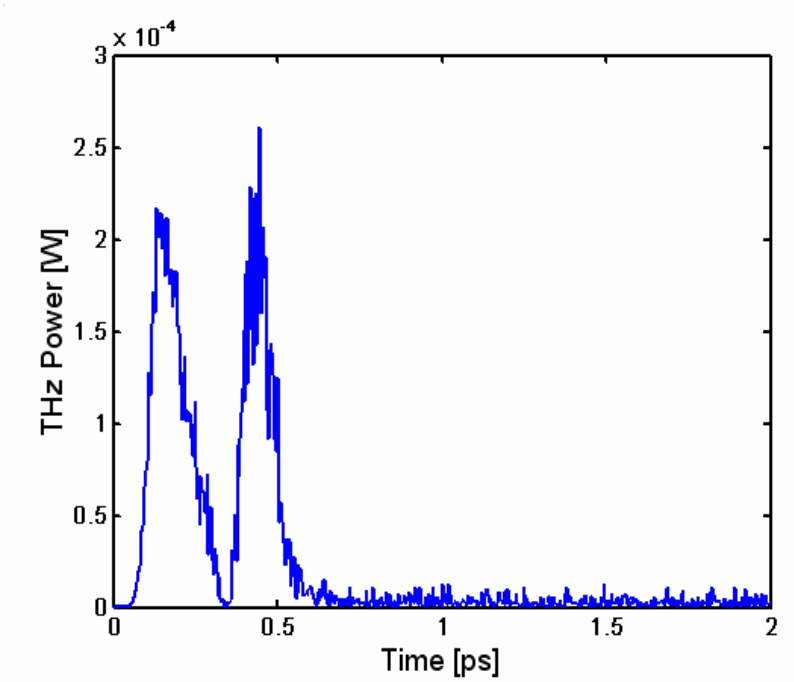

(a)

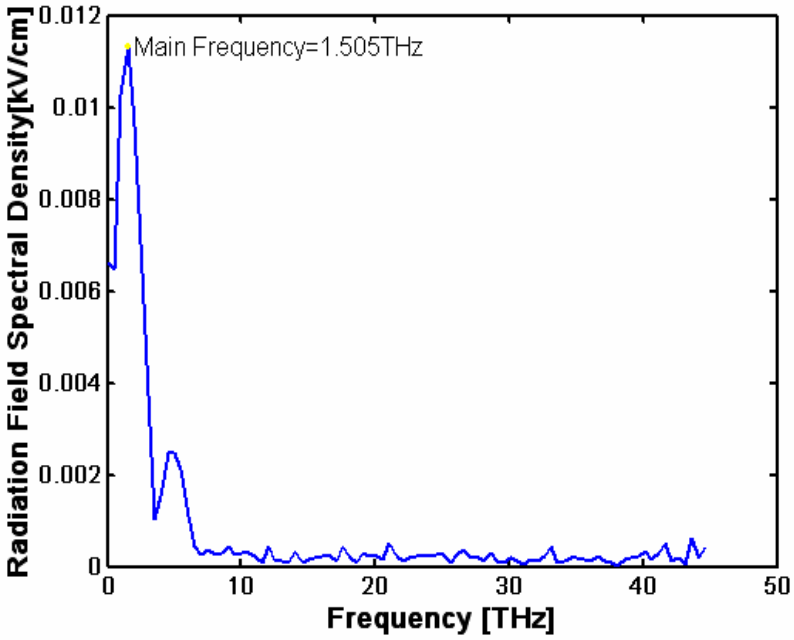

(b)

Figure 4.8 (a) Radiation power vs time. (b) Radiation field spectral density

$$P(t_r) = \frac{(Nq_{sc})^2}{6\pi\varepsilon_0 c^3}\left\{(1-v^2/c^2)^{-2}\left[a^2 + (1-v^2/c^2)^{-1}(\mathbf{v}/c\cdot\mathbf{a})^2\right]\right\}_{t_r}, \quad (4.5)$$

where N is the number of carriers in the ensemble, and v and a are the retarded ensemble averages of the velocity and acceleration respectively. Figure 4.8(a) shows the THz radiation power obtained from Eq. (4.5) as a function of retarded time for $n=5\times10^{17}cm^{-3}$ at 40 kV/cm applied bias field. It is clear that the temporal behavior of the radiated electric field depends directly on the temporal behavior of the velocity and acceleration at an earlier time as we mentioned in transient response from Sec. 3.2,2. Thus, we can see this THz radiation field has 1.5 THz as a main frequency as shown in Figure 4.8(b) by FFT of the THz radiation field in time domain.

4.2.2 The Radiation Field as the Back Action in Large Excitation-Aperture

To improve the performance of photoconductive THz sources due to their typically low THz output power, large excitation-aperture emitters are usually used. However, when a large excitation-aperture photoconductor is excited by strong optical pulses, the THz output strength is saturated. This saturation comes from the screening of the externally applied bias field. In radiation field screening, which is the major source of the saturation for large-aperture photoconductor, the near-field generated at the surface by the transient current cancels out a portion of the bias field. For a large excitation-aperture, where the excitation-spot size well exceeds the center wavelength of the emitted THz transient, radiation effects can be derived from simple electromagnetic boundary conditions [15,29]. Figure 4.9 shows a photoexcited photoconductive emitter with an applied bias.

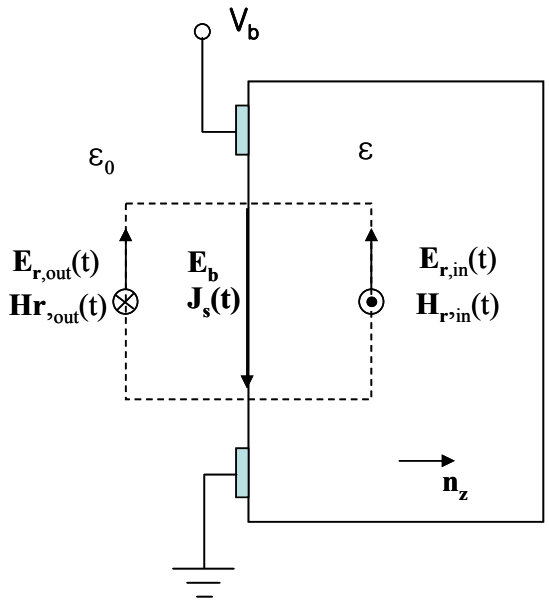

Figure 4. 9 Schematic of a large-aperture photoconductive biased emitter with a voltage V_b.

The electric and magnetic fields around the emitter can be divided into stationary field $\mathbf{E_b}$, and $\mathbf{H_b}$ form the applied bias and transient field $\mathbf{E_r}$, and $\mathbf{H_r}$ from the induced current from optical excitation. When the photoconductor is excited, the surface current $\mathbf{J_s}(t)$ is generated by photoexcited carriers, and the following boundary condition can be derived:

$$\mathbf{E}_{\mathbf{r},in}(t) = \mathbf{E}_{\mathbf{r},out}(t) = \mathbf{E}_{\mathbf{r}}(t),$$

$$\mathbf{J}_{\mathbf{s}}(t) = \mathbf{H}_{\mathbf{r},out}(t) - \mathbf{H}_{\mathbf{r},in}(t). \tag{4.6}$$

When the aperture of the emitter is large compared to the wavelength of the radiation, $\mathbf{H_r}$ can be related to $\mathbf{E_r}$ by

$$\mathbf{H}_{\mathbf{r},in}(t) \times \mathbf{n}_{\mathbf{z}} = \frac{\sqrt{\varepsilon}}{\eta_0} \mathbf{E}_{\mathbf{r},in}(t),$$

$$\mathbf{H}_{\mathbf{r},out}(t)\times\mathbf{n}_{\mathbf{z}}=-\frac{1}{\eta_0}\mathbf{E}_{\mathbf{r},out}(t)\,, \tag{4.7}$$

where η_0 is the intrinsic impedance of free space.

From Eqs. (4.6) and (4.7) the surface current $\mathbf{J_s}$(t) can be represented as a function of the radiated field :

$$\mathbf{J}_{\mathbf{s}}(t)=-\frac{(1+\sqrt{\varepsilon})}{\eta_0}\mathbf{E}_{\mathbf{r}}(t)\,. \tag{4.8}$$

One can see the electric field developed at the surface is opposite to the direction of $\mathbf{J_s}$. from Eq. (4.8). From Ohm's law, the surface current is given by

$$\mathbf{J}_{\mathbf{s}}(t)=\sigma(t)(\mathbf{E}_{\mathbf{b}}+\mathbf{E}_{\mathbf{r}}(t))\,, \tag{4.9}$$

where $\sigma(t)$ is the surface conductivity. From Eqs. (4.8) and (4.9), we get the following equations:

$$\mathbf{J}_{\mathbf{s}}(t)=\frac{\sigma(t)E_b}{1+\dfrac{\sigma(t)\eta_0}{1+\sqrt{\varepsilon}}}\,. \tag{4.10}$$

The magnitude of the induced current is saturated as the optical intensity increases (the surface conductivity increases), The saturation behavior of the photoconducive emitter is governed by Eqs. (4.8) and (4.10), because the near-field is propotional to the surface current and the saturation effect persists as long as there is current. The radiated field can also be expressed as

$$\mathbf{E_r}(t) = -\mathbf{E_b}\frac{\sigma(t)\eta_0}{\sigma(t)\eta_0 + (1+\sqrt{\varepsilon})}. \tag{4.11}$$

As the optical intensity increases, the radiated field is predicted to saturate. This behavior has been observed for both near and far field radiated electric field [15,61].

4.2.3 Coulomb and Radiation Field

In order to enable the development of compact THz systems with high radiation power, we need to consider the overall efficiency with an eye to the limitations due to screening [62] related to excitation-spot size. In addition, one of the unsolved issues in the generation of THz radiation from photoconductors with relative small excitation-apertures is to clarify the relative roles played by the direct Coulomb screening of the bias field by the photogenerated carriers and the radiation screening due to the back action of the THz field on the device itself [63]. When the excitation-spot size is considerably smaller than the center wavelength of the emitted radiation, the boundary conditions as introduced in previous section cannot be used because the electric fields cannot be assumed to be uniform over the excitation aperture boundary. This approach is therefore invalid for photoconductive switches with relatively small gap, which produce highly divergent radiation. Thus, in order to consider the back action of the radiation field on the dynamics of the carriers as well as that due to the static Coulomb field arising from the electron-hole pairs, we report in this section an approach using the retarded electromagnetic field from moving groups of charges introduced in Sec. 4.2.1.

The retarded electromagnetic field of a moving charge of Eq. (4.4) can be split into three terms [59,64,65]:

$$\mathbf{E} = \frac{q}{4\pi\varepsilon}\left[\frac{\hat{R}}{R^2} + \frac{R}{c}\frac{d}{dt}\left(\frac{\hat{R}}{R^2}\right) + \frac{1}{c^2}\frac{\hat{R}\times(\hat{R}\times\mathbf{a})}{R}\right]_{tr=t-R/c},$$

$$\mathbf{E} = \mathbf{E_1} + \mathbf{E_2} + \mathbf{E_3}\,. \tag{4.12}$$

$\mathbf{E_1}$ is the Coulomb field of the charge at its retarded position. It is always present, regardless of whether the electron is in motion. The electric field associated with a stationary charge is entirely in the radial direction as shown in Figure 4.10.

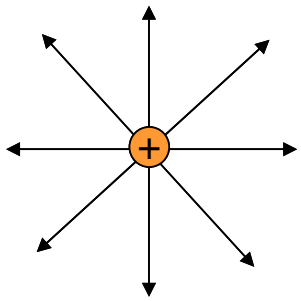

Figure 4. 10 The field lines for a positive charge.

Since a stationary charge will cause no current to flow, there is no magnetic field associated with a stationary charge. Thus it does not radiate electromagnetic waves. Also, the electric field caused by a charge moving with a constant velocity *(a=0)* is entirely normal to the spherical surface and the magnetic field is tangent to the surface as shown in Figure 4.11. So, the Poynting vector $\mathbf{S}=\mathbf{E}\times\mathbf{H}$ is completely confined within the spherical surface. Also, we can think it does not radiate in the radial direction away from the charge. Thus, we can call only $\mathbf{E_3}$ the radiation field.

This $\mathbf{E_3}$ is also the transverse component of the disturbed field. As mentioned, stationary charges and charges moving with a constant velocity do not radiate

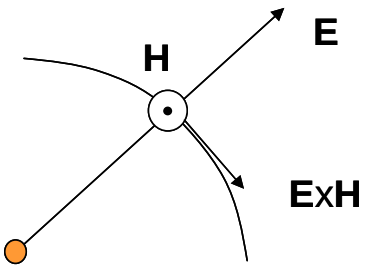

Figure 4. 11 The Poynting vector associated with a charge moving with a constant velocity.

electromagnetic waves and have an electric field that is only radially outward. We expressed it as the Coulomb field in Figure 4.12. These electric field lines in Figure 4.12 must be continuous since they are caused by the same charge. So we can see the resulting disturbance in the field. In this disturbance, there are components of the electric field that are perpendicular to the Coulomb field. These transverse components are responsible for the radiation. We can call the transverse component of the disturbed field the radiation field. Thus, Eq. (4.12) can also be split into two components; the longitudinal field, and the transverse field depending on the direction of field.

We can express $\mathbf{E_2}$, which is the induction field 90 degrese out of phase with the magnetic field, by the term of $(R/c)(d\mathbf{E_1}/dt)$. Thus, we will split the electric field of Eq. (4.4) into two terms, the Coulomb field (the transformed Coulomb field) $\mathbf{E}_c$, and the radiation field $\mathbf{E}_r$ to have an intuitive idea of what this means.

In order to distinguish the Coulomb and radiation components of the THz radiation field, since the maximum drift velocity of the photoexcited carriers is much less than the speed of light, $v/c \ll 1$ ($\mathbf{E_2}$ is fairly small), the electric field of Eq. (4.4) can be conveniently split into two components: the Coulomb field, $\mathbf{E}_c$, and the radiation field $\mathbf{E}_r$ [55,64] as

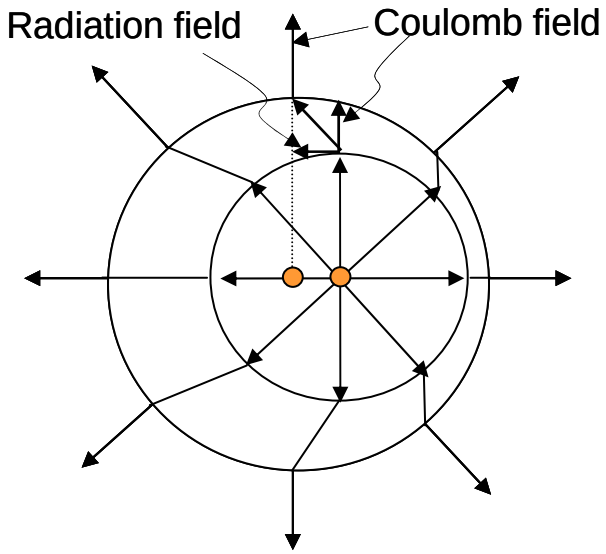

Figure 4. 12 Electromagnetic waves radiated by a charge that is accelerated.

$$\mathbf{E} \cong \mathbf{E}_c + \mathbf{E}_r = \frac{q}{4\pi\varepsilon}\left(\frac{\hat{R}}{R^2}\right)_{t_r} + \frac{q}{4\pi\varepsilon c^2}\left(\frac{\hat{R}\times(\hat{R}\times\mathbf{a})}{R}\right)_{t_r}. \tag{4.13}$$

When the charge is stationary (**v**=*0,* **a**=*0*), we have only the Coulomb field $\mathbf{E}_c$ while the radiation field $\mathbf{E}_r$ is expected to dominate for large values of the acceleration. To include numerically even small effects of the drift velocity in the radiation field $\mathbf{E}_r$ or the Coulomb field $\mathbf{E}_c$, we can subtract the Coulomb field $\mathbf{E}_c$ or the radiation field $\mathbf{E}_r$ from the electric field **E** in Eq. (4.4), respectively [65]. In order to obtain the transport properties (**R**, **v**, and **a**) of the photoexcited carriers, we solved the Boltzmann transport equations employing the Monte-Carlo method mentioned in previous chapters.

4.2.4 Coulomb and radiation screening in photoconductive THz sources

We consider a GaAs-based photoconductive source laterally biased at 40 kV/cm in the *x*-direction excited by a 75-fs FWHM gaussian-envelope optical pulse spectrally centered at 800 nm with a repetition rate of 76 MHz. We use 10^5 superparticles whose distribution is adjusted to be proportional to the temporal and spatial shape of the optical pulse. Patterned on top of the device are assumed to be two infinitely long parallel electrodes, between which is the photoconductive gap with size four times the excitation spot diameter (FWHM). Various excitation spot sizes and levels incident upon this gap were simulated. The optical excitation acts as a carrier source within the Monte-Carlo simulation; the carrier source terms are taken as Gaussian both temporally and spatially to match the optical excitation pulse.

We give simulation results in Figure 4.13 for the Coulomb field profiles and the radiation field induced by accelerating carriers after laser excitation with a 20 μm FWHM spot diameter for a peak carrier density of 10^{17} cm^{-3}. Since the net positive and negative space charges develop as the electrons and holes drift in opposite direction, the electric field induced by this space charge screens the bias field as shown in Figure 4.13(a). For the radiation field due to the accelerating carriers, it is clear from Eq. (4.4) that the temporal behavior of the radiated electric field depends directly on the temporal behavior of the velocity and acceleration at an earlier time. The directional characteristics of the radiation field depend in turn upon the relative orientation of the velocity and the acceleration. Thus, the electric field induced by the accelerating carriers is also in the direction opposite to the bias field as shown in Figure 4.13(b). These Coulomb and radiation fields effectively collapse the bias field driving the carriers and results in the

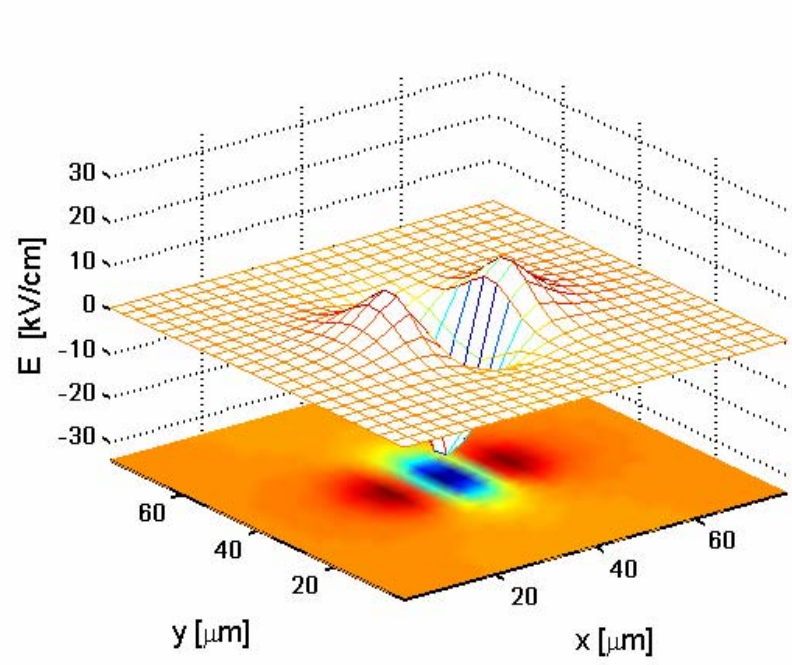

(a)

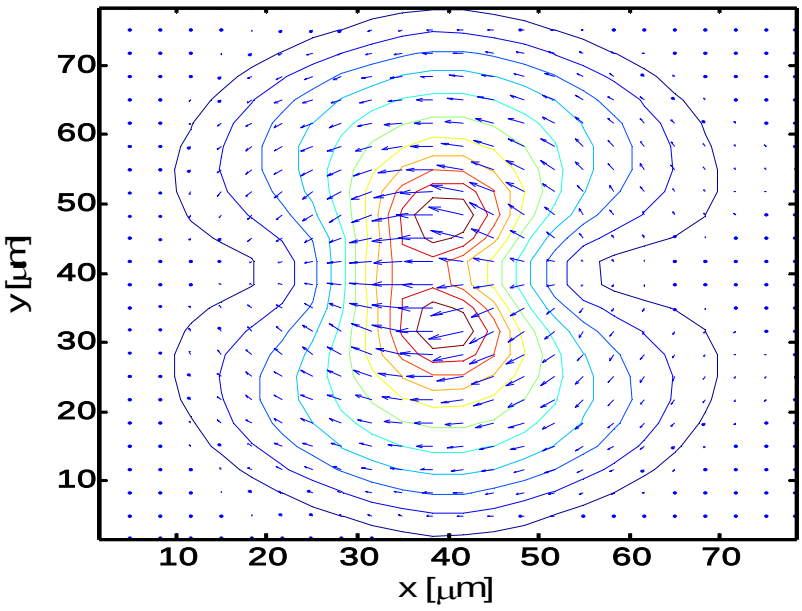

(b)

Figure 4. 13 (a) The Coulomb screening field induced by the space charge. (b) The direction of radiation screening field caused by accelerating charges.

saturation of THz output field strength. The Coulomb screening field near the spot edges is weaker than at the center of the Gaussian laser spot as shown in Figure 4.13(a), since the carrier density decreases toward the edges [48,58]. In Figure 4.13(b), we can see that the radiation field near the edges of the spot away from the its center in *y*-direction is stronger than anywhere else since the carriers near these edges move faster than others because of the weak Coulomb screening field. The peak points of the radiation screening field move to the anode due to the high mobility of the electrons comparing to the holes.

First, to distinguish between the Coulomb contribution that produces space-charge screening and the radiation contribution caused by the acceleration of carriers as a function of excitation aperture size, we continue to consider the GaAs-based photoconductive source biased at 40 kV/cm excited by a 75-fs FWHM Gaussian optical pulse maintaining the peak excited carrier densities $10^{17}cm^{-3}$. (Thus the total optical pulse energy varies with spot size.) Figure 4.14 shows the screening field (the *x*-component of the retarded field) as a function of spot diameter maintaining a given carrier density by adjusting the incident optical power. As the excitation spot size increases, the overlap of the photoexcited electron and holes also increases. Thus, relatively small net positive and negative space charges develop, and the distance between them increases. One can see the Coulomb screening decrease as the excitation spot diameter increases. Meanwhile, for the radiation screening, although the excitation aperture size increases, the radiation field remains essentially constant with excitation spot size due to the same carrier density. One can increase the laser power to obtain high radiation power, because the total power is proportional to the square of the number of photoexcied carriers. If one increases laser

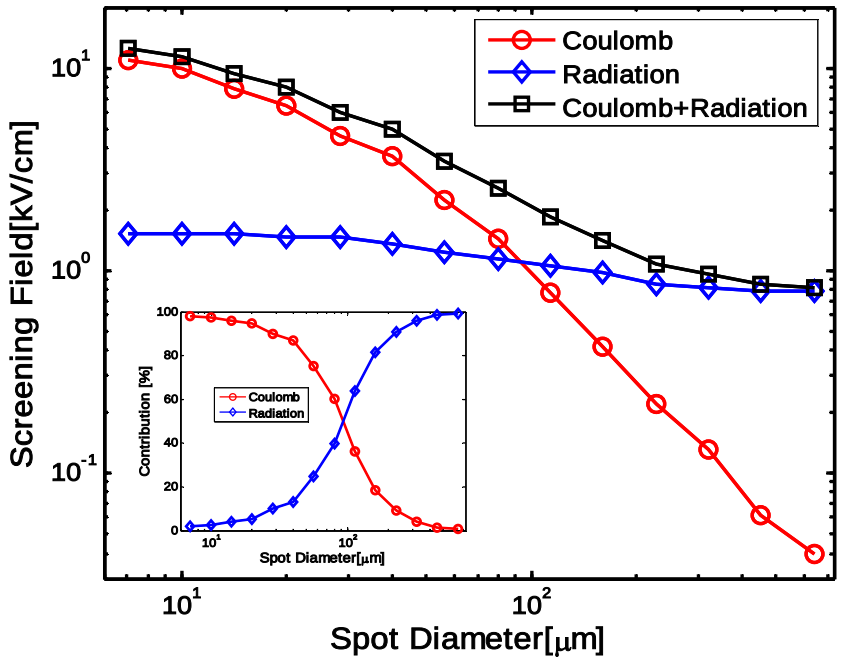

Figure 4. 14 Coulomb and radiation screening field versus excitation spot diameter (FWHM) for a given carrier density 10^{17} cm^{-3}. Inset: Contribution of the Coulomb and radiation field to the screening field versus excitation spot diameter (FWHM).

power and the excitation-spot size for a fixed peak carrier density, then the increased role of radiation screening resulting from the increase in the number of photoexcited carriers does not occur during the THz emission process (1 ps transit across 0.1 mm), as mentioned above. The contributions of Coulomb and radiation screening are shown in the inset of Figure 4.14. One sees the Coulomb screening field is dominant up to an excitation spot size of ~100 μm FWHM, but for larger spot size, the radiation field dominates.

In the typical experiment one has fixed optical power, but can vary the spot size by means of focusing optics. In this case, as the excitation spot size increases, the

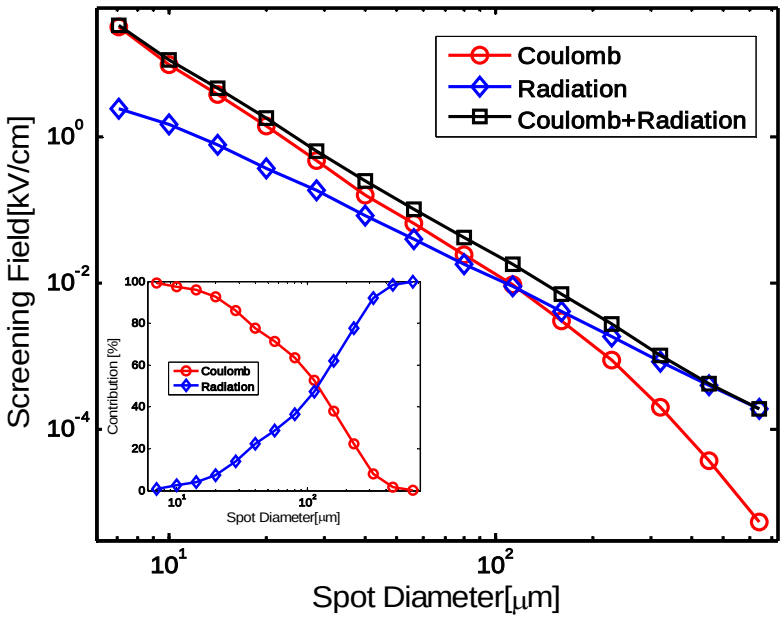

Figure 4. 15 Coulomb and radiation screening field versus excitation spot diameter (FWHM) for a given optical excitation power 5 mW. Inset: Contribution of the Coulomb and radiation field to the screening field versus excitation spot diameter (FWHM).

Coulomb screening field decreases rapidly as shown in Figure 4.15 (compare with Figure 4.14) because the distance between the carriers increases due to the decrease of carrier density. In addition, as the carrier density becomes sparse, the carrier numbers contributing the Coulomb and radiation screening field decrease. As a result, the radiation screening field also decreases as the excitation aperture size increases, as shown in Figure 4.15. The contributions of Coulomb and radiation screening in this case are shown in the inset of Figure 4.15. One sees similar contributions to the screening field in the inset of Figure 4.15 except for the gradual slope resulting from the decrease of both of the Coulomb and radiation fields at the same time. As a result, we find that if the

electromagnetic propagation time across the emitter is longer than the duration of the generated electromagnetic transients (~1ps), then the relative importance of Coulomb and radiation screening clearly depends on the excitation-spot size. From Figures 4.14 and 4.15, one sees that the dominant component of the screening field crosses over at an excitation aperture size with full width at half maximum (FWHM) of ~100 μm for a range of reasonable excitation levels.

4.2.4 Enhancement of the Optical-to-THz Conversion Efficiency

In the absence of screening, as optical excitation increases, the THz radiation power also increases due to the quadratic fluence dependence of the THz radiation power on the number of charges contributing from Eq. (4.5). The THz power also originates from carrier acceleration by the bias field since the THz power is proportional to the square of the acceleration, as shown in Eq. (4.5). Thus for a given excitation level, if we can maintain the external bias field by reducing the screening as we increase the excitation aperture size as in Figure 4.15, we can obtain optimal conversion efficiency from optical to THz radiation as shown in Figure 4.16. One sees the enhancement of the optical-to-THz conversion efficiency defined by the ratio of average THz radiation power and the optical excitation power (5 mW) from 0.024 % to 2.6 % as the excitation spot

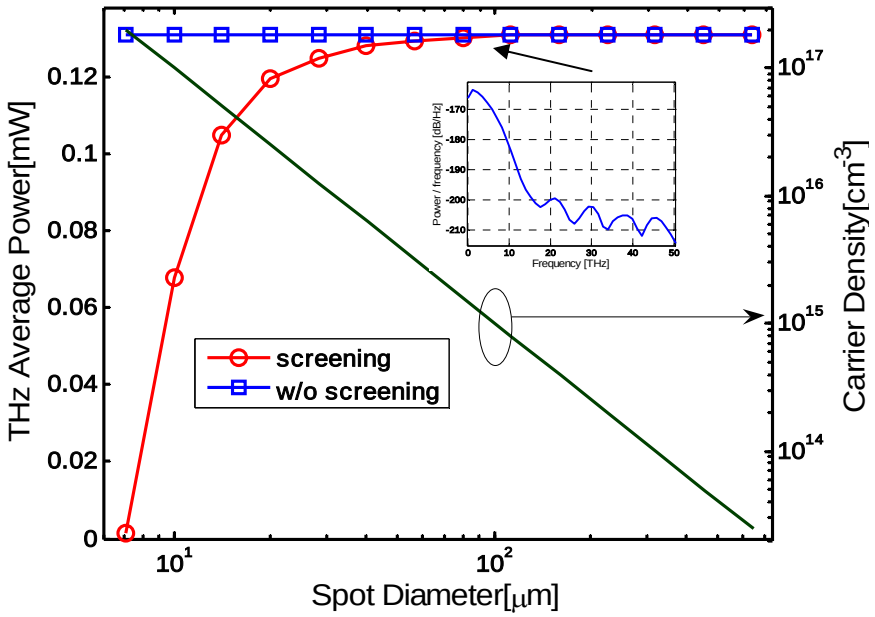

Figure 4. 16 The THz average radiation power as a function of excitation spot diameter (FWHM) for a given optical power 5 mW.

diameter increases from 7 μm FWHM (THz average power: 1.24 μW—within an order of magnitude of the experimental result in Ref. 62) to more than 100 μm FWHM (THz average power, 0.13 mW). We obtain the THz average power from power spectral density (PSD) like the inset of Figure 4.16 by integrating over the frequency range of PSD [66]. For a given optical excitation power (5 mW), the conversion efficiency with excitation spot diameter more than 100 μm FWHM is enhanced by a factor of 100 compared with 7 μm FWHM excitation spot diameter. Thus, we can predict an enhancement of the optical-to-THz conversion efficiency with increasing excitation-spot size [22].

4.3 Trap-Enhanced Fields in Semi-Insulating Photoconductors

Recent work has shown that the THz generation process becomes particularly efficient when the excitation is carried out close to the positively biased electrode (anode) in semi-insulating (SI-) GaAs sources due to trap-enhanced fields (TEF) in proximity of the anode [56,62,67]. This effect manifests itself in the THz generation in the rapid acceleration of the photoexcited carriers within the bias field [68]; since the bias field is largest near the anode, it is important to photogenerate as many of the carriers as possible in the TEF region. Due to the growth in interest in THz technology as well as the widespread deployment of photoconductive sources, the mechanisms responsible for the electric-field behavior and charge compensation in SI-GaAs warrant further elucidation.

An accurate model for the mechanisms underlying and limiting THz generation by optical excitation in SI-GaAs must include a detailed description of the transport of the photocarriers. At the same time, the associated modification of the electric-field distribution under nonuniform illumination near the metal/SI-GaAs contact coupled with the Coulomb and radiation screening of the bias field [22] must all be included to provide a reasonable description of the THz-generation process as well as to overcome the low-output/low-optical-to-THz-conversion-efficiency bottleneck currently facing the field. While an adequate description of these effects is needed to attain the degree of understanding requisite to design better THz sources, the underlying physical mechanisms are not easily accessible by conventional techniques, including current-voltage and capacitance-voltage measurements due to the very low conductivity in SI semiconductors.

In this section, the nonuniform optical excitation of SI-GaAs photoconductive THz sources is investigated via the Monte-Carlo method for the transport properties of the photoexcited carriers. At the same time, the Poisson equation for the space-charge screening and the trap effects together with the three-dimensional Maxwell equations for radiation screening by the emitted THz field are included self-consistently. We show how the combination of illumination geometry, deep traps, and the applied bias field affects and controls the transient response. In Sec. 4.3.1, we review the theory of deep-level traps and obtain the electrostatic properties of the metal/SI-GaAs interface, and subsequently in Sec 4.3.2, investigate the detailed mechanisms responsible for the large TEF near the anode. Section 4.3.3 presents simulation results for the transport properties of photoexcited carriers, illustrating the role of screening and the resulting enhancement or suppression of THz emission depending on excitation geometry.

4.3.1 Electrostatic Properties of SI-GaAs

Semi-insulating GaAs may be produced by a variety of techniques [69-71], but in each case the dominance of at least one deep-level defect or impurity state results. Although several-level defect models have been proposed, SI compensation is in most cases obtained principally through the interplay between only two of the many possible defect levels [72]. For this study, we assume SI-GaAs grown by the liquid encapsulated Czochralski method, which renders SI material through a careful balance between the native-defect deep donors EL2 and the residual shallow acceptor impurities, mainly carbon [73,74]. This deep level can be partially ionized, and the ionization of the deep donors may change with operating conditions, as opposed to a shallow level which is

normally assumed to remain fully ionized. Therefore, in SI material, the deep defect and residual acceptor play the dominant roles in establishing the space-charge density. That is, the occupation of the defect centers and their varying degrees of ionization contribute strongly to the local space-charge density, since they determine the compensation degree together with the residual impurities. These defects and residual impurities are also believed to control the electrical properties of SI-GaAs such as the enhancement of the capture cross section, increasing their ability to capture electrons and consequenctly to alter the space charge [75,76].

In this section we describe the electrostatic properties of SI-GaAs where SI compensation is achieved by a defect (deep donor) EL2, the dominant donor trap located at E_c–0.691eV (E_c is conduction-band edge), commonly found in concentrations of 2×10^{16} cm^{-3}. These deep traps in the form of the EL2 defect compensate the intentional doping of carbon as a shallow acceptor located at E_v+0.026eV (E_v is valance-band edge) in concentrations of $2\times10^{15}cm^{-3}$.

The free-carrier interactions with an electronic defect center are described by the Shockley-Read-Hall (SRH) recombination-rate equation [77],

$$R = \frac{np - n_i^2}{\tau_p(n+n_1) + \tau_n(p+p_1)}, \tag{4.14}$$

where n_i is the intrinsic carrier concentration, n_1 and p_1 are the equilibrium electron and hole concentrations, respectively, n and p are the nonequilibrium carrier concentrations, and τ_p and τ_n are the hole and electron lifetimes. The free-carrier densities n and p both contribute significantly to determining whether a defect center acts as a trap or as a

recombination center. If the defect center lies close to the middle of the band gap, at T = 300 K and a typical density of N_t= 2 × 10^{16}cm^{-3}, the EL2 defect functions as a strong electron trap. That is, the EL2 defect is a relatively poor recombination center because carrier lifetimes are τ_n = 1.6 ns and τ_p =1.5μs according to $1/CN_t$ where C is the capture cross section (C_n = 6.7× 10^{-16} cm^2 for electrons and C_p = 2.0× 10^{-18} cm^2 for holes) and the recombination rate is limited by these lifetimes from Eq. (4.14) [78]. From this SRH equation, we can determine the occupation factor F (the probability that the defect state is occupied) for defect-center occupancy as a function of the electron and hole densities as

$$F(n,p) = \frac{n\tau_p + p_1\tau_n}{\tau_p(n+n_1) + \tau_n(p+p_1)}. \tag{4.15}$$

First, to account properly for the interaction of the defect center's occupation on the local space charge density in SI material, it is necessary to determine the position of the Fermi level to decide whether the defect state is donor- or acceptor-like, since the charge densities of the donor state and the acceptor state are obtained by $+qN_d(1-F)$ and $-qN_aF$, respectively. (q is electron charge, N_d and N_a are densities of states for the donor and acceptor sate, respectively. $(1-F)$ is the probability that the donor state is empty, while F is the probability that the acceptor state is occupied.) Thus, the occupation of the defect centers and their ionization contribute to the local space-charge density. The location of the Fermi level in SI-GaAs can be determined by imposing global charge neutrality. Under equilibrium conditions, the occupation factor F of Eq. (4.15) is a Fermi-Dirac distribution $F_i=1/(1+f_i)$; f_a and f_d are defined below for defect centers as acceptor

and donor states, respectively. f_n and f_p are also defined for electron and hole concentration as

$$f_a = g_a^{-1} \exp[(E_a - E_f)/kT],$$

$$f_d = g_d \exp[(E_f - E_d)/kT],$$

$$f_n = \exp[(E_c - E_f)/kT],$$

$$f_p = \exp[(E_f - E_v)/kT], \tag{4.16}$$

where E_f is the Fermi energy, E_d and E_a are the energy levels of the deep defect center (donor) and shallow acceptor, k is the Boltzmann constant, and T is the temperature; g_a and g_d are the degeneracy factors for the acceptor and donor levels, respectively (g_a = 0.25 and g_d = 0.845 are used in this work).

The ionized donor and acceptor and the electron and hole concentrations are given by,

$$N_d^+ = \frac{N_d}{1+f_d},$$

$$N_a^- = \frac{N_a}{1+f_a},$$

$$n = \frac{N_c}{1+f_n},$$

$$p = \frac{N_v}{1+f_p}, \tag{4.17}$$

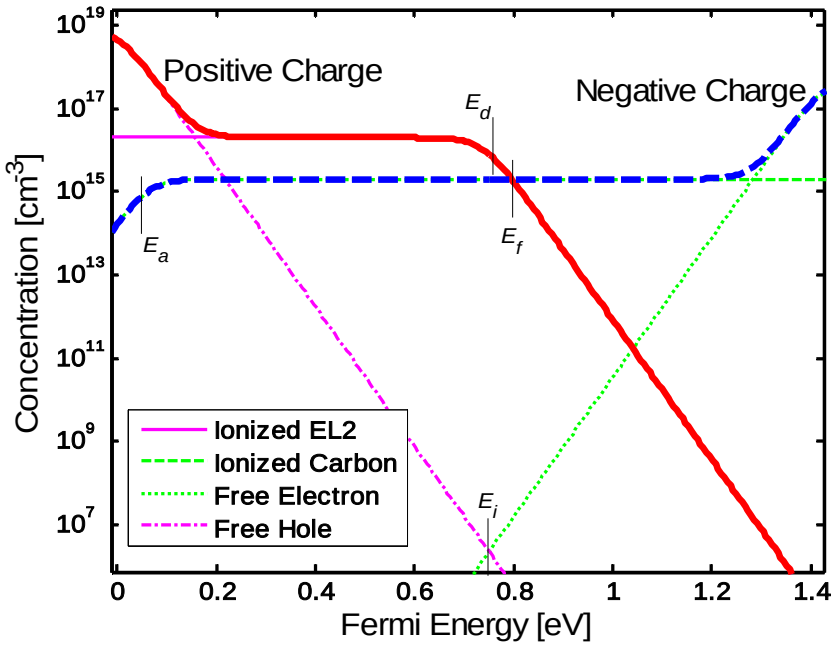

Figure 4. 17 Shockley diagram corresponding to a SI-GaAs with the deep donor EL2 (E_d) and the shallow acceptor carbon (E_a).

where N_c and N_v are the conduction- and valance-band effective densities of states, respectively. The position of the Fermi level E_f can be obtained by setting the charge density to zero,

$$N_d^+ - N_a^- - n + p = 0\,, \tag{4.18}$$

as shown in the Shockley plot of Figure 4.17. Hence, the Fermi level in the SI material is given by Eqs. (4.17) and (4.18) as

$$E_f = E_d - kT \ln g_d + kT \ln\left(\frac{N_d}{N_a} - 1\right). \tag{4.19}$$

Figure 4.17 shows the net positive and negative contributions to the overall space charge as a function of Fermi energy in which the Fermi level is locked to a position slightly above the intrinsic level, which makes this SI-GaAs very slightly *n*-type [78,79].

Now, we derive the principal electrostatic properties of a SI-GaAs based photoconductive THz source, such as the charge-density and electric field profiles due to the space charge for different bias potentials. If we applied different electrode potentials to a photoconductive THz source based on SI-GaAs as shown in Figure 4.18, the contact potential would cause band bending thus leading to a space-charge region, i.e. within the region of band bending, the changing position of the Fermi energy alters the occupation of the donor and acceptor levels so that, Eq. (4.17) becomes

$$N_d^{+}(x) = \frac{N_d}{1 + f_d \exp(q\varphi(x)/kT)},$$

$$N_a^{-}(x) = \frac{N_a}{1 + f_a \exp(-q\varphi(x)/kT)},$$

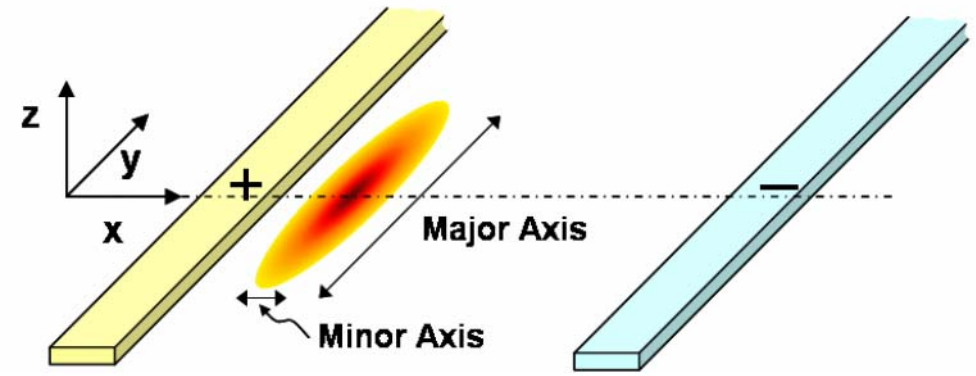

Figure 4. 18 Configuration for various excitation-spot positions along the *x*-direction between the gap and elliptical excitation near the anode.

$$n(x) = \frac{N_c}{1 + f_n \exp(-q\varphi(x)/kT)},$$

$$p(x) = \frac{N_v}{1 + f_p \exp(q\varphi(x)/kT)}. \tag{4.20}$$

The spatial profile of the charge density and the electric-field distribution obtained from the electrostatic potential $\varphi(x)$ for different bias potentials are determined by the Poisson equation self-consistently as

$$\frac{d^2\varphi(x)}{dx^2} = -\frac{q}{\varepsilon_s}\left[N_d{}^+(x) - N_a{}^-(x) - n(x) + p(x)\right], \tag{4.21}$$

where ε_s is the dielectric constant of the photoconductor.

Under conditions of thermal equilibrium, the traditional transport model reduces to the Poisson equation (4.21) where the free-carrier densities and impurity ionization are set by the local value of the Fermi potential to include partial ionization of the defect centers [77,80]. The position of the Fermi energy can be specified in terms of local potentials by defining the electrostatic potential $\varphi(x)$ as the function that contains an arbitrary additive constant as a reference point [81,82]. This potential function $\varphi(x)$ is defined relative to the conduction- and valence-band edges such that it has the position of the intrinsic Fermi level with respect to the band edges. Since the potential is defined as the difference between the Fermi level and the intrinsic level as the reference point, the zero-bias potential $\varphi_0\ (x=0)$ is expressed as

$$\varphi_0 = -\phi_b + (E_c - E_i)\,, \tag{4.22}$$

where ϕ_b is an effective potential barrier height and E_c–E_i is the energy difference between the conduction band and the intrinsic level. The effective barrier height is given by

$$\phi_b = \phi_b{}^0 - \Delta\phi_b\,, \tag{4.23}$$

where $\phi_b{}^0$ is the barrier height under flat-band conditions (ϕ_b = 0.5eV is used in this work) and $\Delta\phi_b$ is the reduction of the barrier height caused by image-force lowering, which is expressed as [77,83]

$$\Delta\phi_b = \sqrt{qE_{\max}/4\pi\varepsilon_s}\,, \tag{4.24}$$

with E_{max} the electric field at the metal-semiconductor junction. For an applied voltage V, the potential $\varphi(x)$ at $x=0$ becomes

$$\varphi(x) = \varphi_0 + V\,. \tag{4.25}$$

We take $\varphi(x=\infty) = 0$ as the reference voltage, and this is maintained constant.

4.3.2 Trap-Enhanced Fields

Figure 4.19 shows the profile of the net charge expressed as $N_{net} = N_d{}^+(x) - N_a{}^-(x) - n(x) + p(x)$ in the region near the forward biased positive contact (anode) of the SI-GaAs for various bias voltages. One sees that positive charge predominates as the reverse bias increases and that negative charge becomes dominant as

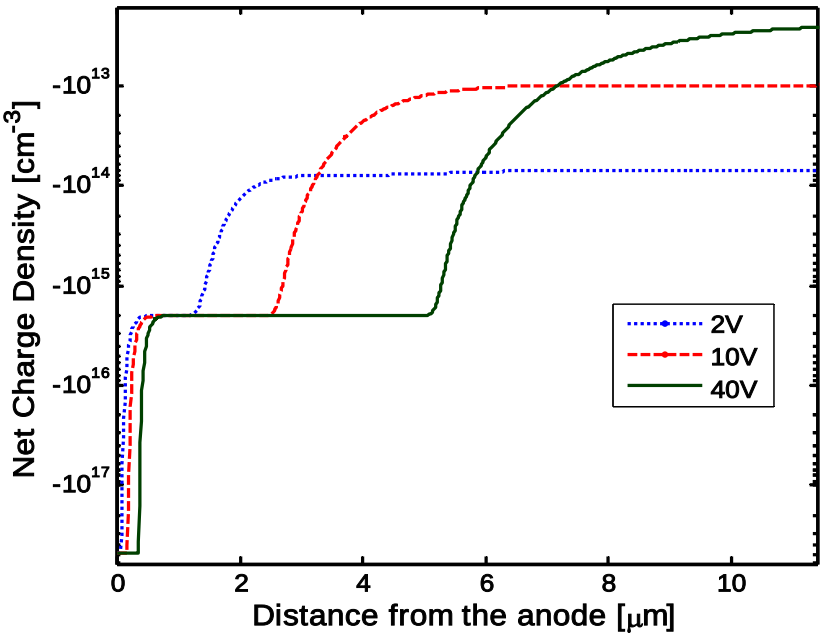

Figure 4. 19 Profile of net charge density near the anode of SI-GaAs for various bias voltages.

forward bias increases from Figure 4.17 and Eq. (4.20), since the Fermi level E_f lies 0.083 eV above the intrinsic level E_i and the deep donor level E_d and the shallow acceptor level E_a lie 0.061 eV and 0.769 eV below E_f, respectively. For low bias voltage $|V|$, with the low values of free carrier concentrations ($\approx 10^7$ cm^{-3}) in SI-GaAs, the net charge N_{net} is dominated by the space charge arising from ionized donors and acceptors $N_d^+ - N_a^-$. For example, at a forward bias V = 2 V, the donor states in the space-charge region cannot be fully ionized, while the acceptor states are fully ionized, which leads to $N_{net} \approx N_a^-$. Due to the almost full occupancy of the EL2 traps (the EL2 defect centers become fully occupied by electrons), that are responsible for compensation of the residual acceptors, the uncompensated ionized acceptors result in a space-charge region that is limited only by the net acceptor concentration, so negative charge appears near the

metal/SI-GaAs contact. When the EL2 defect center becomes fully occupied by electrons within the space-charge region and EL2 is a deep donor, this center becomes relatively charge neutral. Hence, the net space-charge density is set entirely by the residual acceptors (carbon) density.

For large $|V|$, however, the free carriers may contribute significantly to the net charge in an area very close to the metal/SI-GaAs contact (< 1 μm). For forward bias, V = 40 V, the contribution of the free carriers is significant, leading to a larger density of the net negative charge in the region adjacent to the metal/SI-GaAs interface. The width of the space-charge region can also be inferred from Figure 4.19. One sees that the region of free electrons and uncompensated ionized acceptors extends further into the material as the bias voltage increases, thus increasing the extent of the space-charge region.

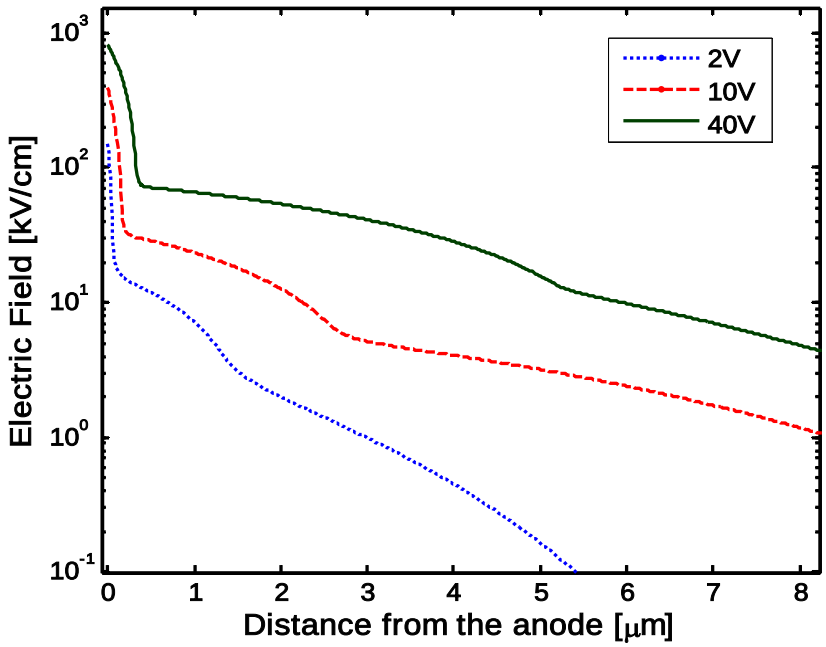

Figure 4. 20 Spatial electric field distribution near the anode of SI-GaAs for different bias voltages.

The spatial electric-field distribution as shown in Figure 4.20 is obtained from Eq. (4.21) for various bias voltages. With the application of increasing bias, the nonuniform charge distribution of Figure 4.19 creates a three-zone electric-field distribution across the device. In the first extremely high-field zone, the electric field decreases dramatically near the metal/SI-GaAs contact since the free electrons cause a large and rapid potential drop. The width of this zone, however, is very small at low applied voltages. (It lies within a few tens of nm from the metal contact). Meanwhile, for high voltages, the electric field (corresponding to the 40 V bias voltage) is 10^3 kV/cm, and this extremely high-field zone lies within 0.4 μm of the metal contact. The second highest field region, where most of the applied bias potential drop occurs, since the uncompensated ionized acceptors cause most of the applied bias potential to drop, the electric field near the anode decreases rapidly with a slope approximately equal to qN_a^-/ε_s. We can see that these large fields at the anode extend further from the metal/SI-GaAs interface with increasing bias (for 40 V, the large field in the second high-field region extends more than 5 μm from the anode). At the end of this region, the electric field decreases less rapidly as the space charge is negligible beyond this point.

These large fields in the first and second zone near the anode are known as the trap-enhanced electric field (TEF) [56]. It is due to the rapid potential drop experienced by free carriers (for high bias voltage) and the uncompensated ionized acceptors resulting from the full occupancy of the EL2 trap which is responsible for compensation of the residual acceptors. The TEF is responsible for the dramatically enhanced THz electrical response for localized excitation near the anode of a SI-GaAs based photoconductor.

4.3.3 Efficient THz Generation by Spatially Broadened Excitation

When the biased photoconductor with the TEF is illuminated by a femtosecond optical pulse to generate THz radiation, we need to incorporate the transport equations into the Poisson equation (4.21) for nonequilibrium conditions. To consider properly the SI photoconductor following photoexcitation, it is absolutely necessary to include the occupation factors' dependence on both charge-carrier densities, including the photoexcited excess carriers as expressed in Eq. (4.15), as well as the recombination-rate effect due to the defect center as expressed in Eq. (4.14). We note, however, that the fraction of carriers that recombine is very small compared with the photoexcited carrier density within the duration of the THz pulse (not greater than ~1 ps). (The recombination density of electron-hole pairs in 1 ps is ~10^{11} cm^{-3} given by $R \times 1ps \approx \partial p / \tau_p \times 1p$ in the case of a photoexcited carrier density of 10^{17} cm^{-3} [77].) Therefore, Eq. (4.21) becomes

$$\frac{d^2\varphi(x)}{dx^2} = -\frac{q}{\varepsilon_s}\Big[N_d[1 - F\{n(x) + \delta n(x), p(x) + \delta p(x)\}] - N_a[F\{n(x) + \delta n(x), p(x) + \delta p(x)\}] - n(x) - \delta n(x) + p(x) + \delta p(x)\Big]. \tag{4.26}$$

This fully accounts for the variation in the defect center occupancy which is induced by changes in the local carrier densities due to the introduction of the photocarriers and the interaction with the local space-charge density obtained by solving the Boltzmann equations. To consider this photoexcited carrier contribution and to obtain the transport properties, we solved the Boltzmann equations employing the Monte Carlo method mentioned in previous chapters. If the photocarriers are accelerated to the electrode by the established electric field as show in Figure 4.20, these photoexcited excess carriers

change the charge and potential distribution. The change of the potential affects the carrier density through Eqs. (4.20) and (4.26), and changes the local electric field through the spatial derivative of potential. This redistribution of the field affects the movement of the photocarriers self-consistently. [The actual solution of Eq. (4.26) is numerically calculated in this work by an iteration method until the difference between successive values is less than 10^{-5}.]

To investigate the excitation-position and shape dependence of the THz emission in the presence of the large TEF's near the metal/SI-GaAs contact, we consider a SI-GaAs based photoconductive source laterally biased at 80 kV/cm in the *x*-direction excited by a 75-fs full width at half maximum (FWHM) Gaussian-envelope optical pulse spectrally centered at 800 nm with a repetition rate of 76 MHz. We use 10^5 super particles whose distribution is adjusted to be proportional to the temporal and spatial

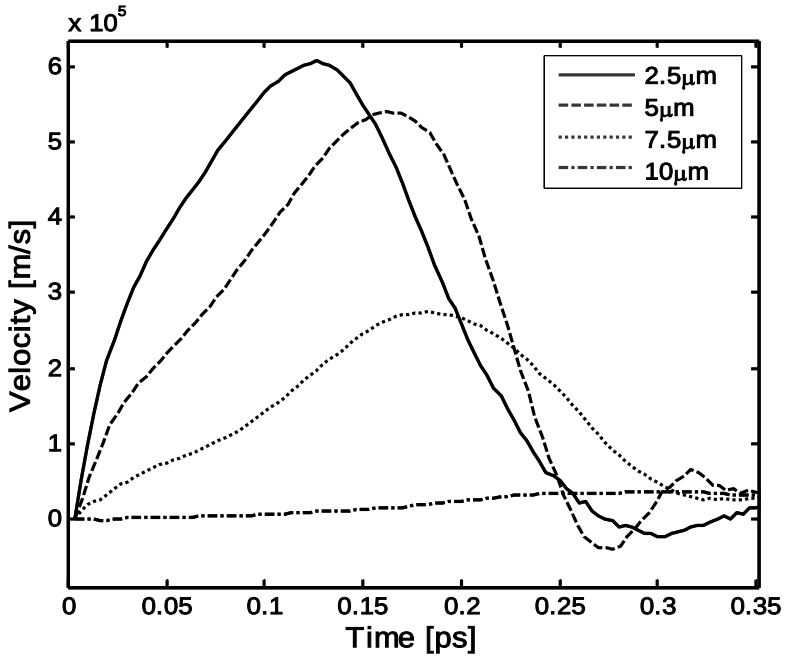

Figure 4. 21 Transient velocity of the photoexcited electrons for various excitation-spot positions with respect to the anode in SI-GaAs.

shape of the optical pulse. Patterned on top of the device are assumed to be two infinitely long parallel electrodes, between which lies the photoconductive gap of 50 μm. A round Gaussian excitation spot with a 5 μm FWHM diameter (in the intensity) for a peak carrier density of 4×10^{17} cm^{-3} is incident along the *x*-direction upon this gap.

The transient velocity of the photoexcited electrons is shown in Figure 4.21 for various excitation-spot positions. One sees that the excited electrons respond rapidly to the established electric field in Figure 4.21, i.e., as the excitation spot center is moved nearer to the anode, velocity overshoot becomes increasingly important due to the transfer of the electrons to lower effective-mass upper valleys as well as photocarrier screening of the bias field.

The performance of the THz generation depends on the temporal shape of the photoinduced current pulses, and this shape is determined in part by transient velocity overshoot, as shown in Figure 4.21, while the screening is due to the optically excited electron and hole distributions. That is, since this acceleration of mobile charge is responsible for the generation of the THz radiation field, the photoexcited carriers within the large TEF near the anode produce a dramatic field-enhanced transient response of the THz radiation.

To explore the THz radiation field propagation, the screening associated with the photoexcited carriers is calculated from the retarded field due to these moving charges (refer to Sec. 4.2). Figure 4.22 shows the THz signal strength given by Eq. (4.4) as viewed at an observation point 200 μm above the device, as a function of the position of the focused illumination with a 5 μm FWHM round spot and a peak carrier density of 4×10^{17} cm^{-3} incident along the *x*-direction between the gap. One sees that illumination near

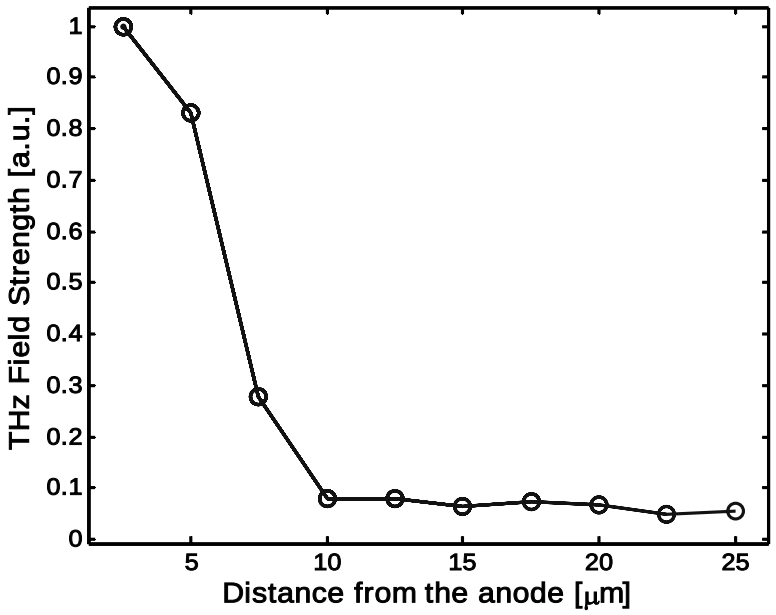

Figure 4. 22 THz radiation field strength as a function of excitation-spot position along the *x*-direction in Figure 4.18.

the anode (2.5 μm) results in radiation several tens of times stronger than when illuminating the center of device (25 μm). This variation in THz emission is entirely attributed to the nonuniform TEF, because the accelerated motion of the photoexcited carriers by the field results in the THz radiation.

When a photoconductor is excited by high peak-fluence optical pulses, the accelerated motion of the photocarriers by the bias field results in the emission of THz radiation, but at the same time, as the carriers undergo their spatial dynamics in the bias field, they partially screen out that bias. The origins of the screening consist of the radiation field and the space-charge field, which contribute to the collapse of the total electric field acting on the carriers at high carrier density [15,48,58]. In order to explore the screening associated with the photoexcited carriers in the large TEF and the

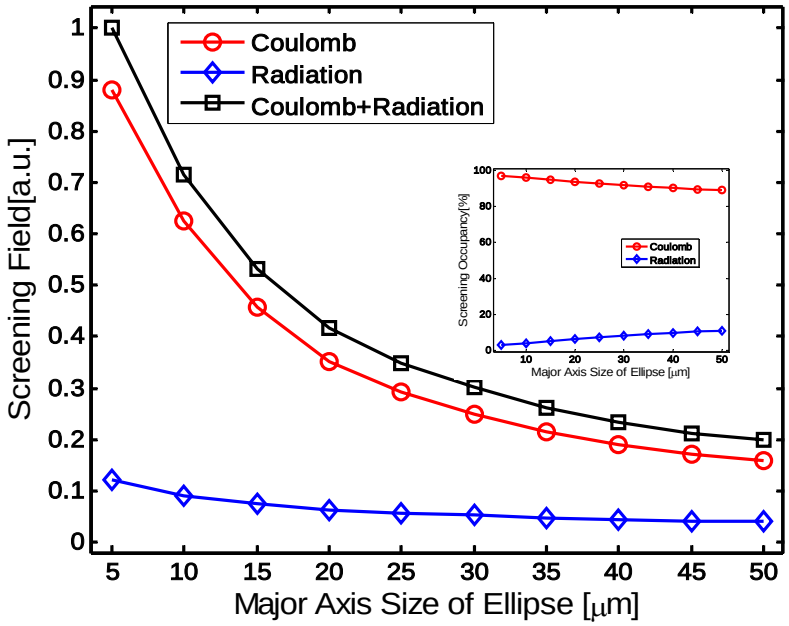

Figure 4. 23 Coulomb and radiation screening field as a function of major-axis size (the *y*-direction) of elliptical excitation-spot in Figure 4.18. Inset: Contribution of the Coulomb and radiation field to the screening field as a function of major-axis size of elliptical excitation-spot

contributions of the Coulomb and radiation components of the field, the electric fields of Eqs. (4.4) and (4.13) are used (see Sec. 4.2).

Figure 4.23 shows the screening field calculated by Eq. (4.13) (the *x*-component of the retarded field) as a function of major-axis size (the *y*-direction) of elliptical excitation-spot in the schematic of device as shown in Figure 4.18, when an elliptical excitation spot with minor axis 5 μm FWHM and major axis 5 – 50 μm for a fixed optical power 5 mW impinges on the device 3 μm from the anode to exploit the large TEF.

As the length of the major axis of the excitation spot increases, one can see that Coulomb screening falls rapidly as shown in Figure 4.23, because the distance between the carriers increases with decreasing carrier density. In addition, as the carrier

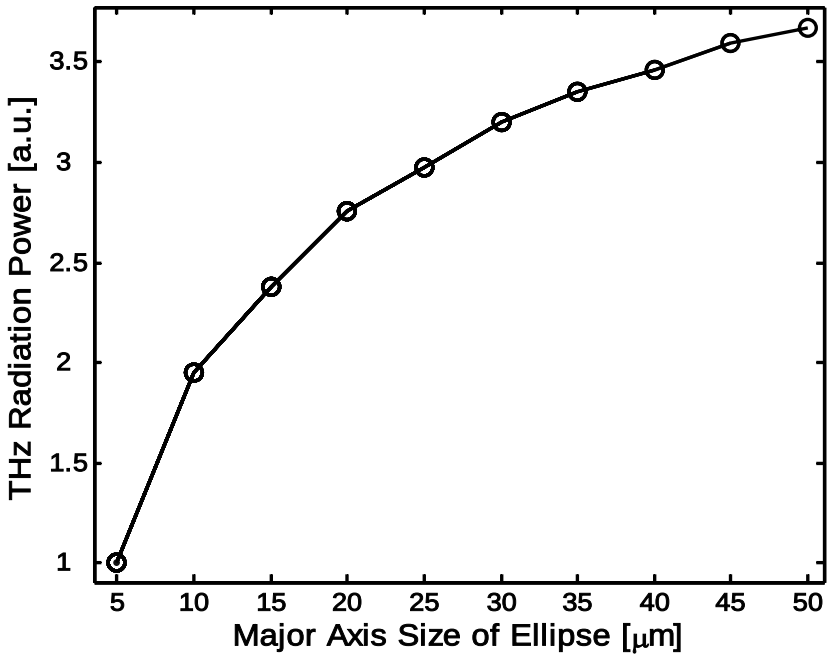

Figure 4. 24 THz radiation power as a function of major-axis size (the *y*-direction) of elliptical excitation-spot in Figure 4.18.

distribution becomes sparse, the carrier numbers contributing the Coulomb and radiation screening field decrease. As a result, the radiation screening field also decreases as the length of the major axis increases, as shown in Figure 4.23. The contributions of Coulomb and radiation screening are shown in the inset of Figure 4.23. One sees that the Coulomb screening field is dominant due to the relatively small excitation aperture size [22].

Although the energy released in the emitted THz pulse ultimately originates from the incoming laser pulse (roughly proportional to the number of photocarriers), the energy transfer from these photocarriers to the radiated THz pulse is mediated by the partial or complete discharge of the electrodes. Therefore, the radiated THz energy is limited by the electrostatic energy stored (product of the total charge of the photocarriers

and the bias potential), and the THz radiation power (radiated electric-field amplitude) should saturate as the total stored electrostatic energy is released since energy supplied by the voltage source can be negligible during the THz emission process (< 1ps). The THz radiation power has a quadratic dependence on the number of charges contributing and also this radiation power is proportional to the square of the acceleration [55], as shown in Eq. (4.3), Thus, for a given excitation level, if we can maintain the large TEF by reducing the screening as we increase the excitation area (aperture) by increasing the major axis of the excitation spot near the anode (Figure 4.18), we expect to improve the THz radiation power originating from the rapid acceleration of the photoexcited carriers by the large TEF, as shown in Figure 4.24. As a result, efficient THz generation is obtained by reducing the impact of the screening effects, which are the main factors underlying the saturation of the THz radiation power, by exploiting an elliptical excitation aperture as eccentric as possible with the major axis parallel to the anode and lying to the maximum extent within the large TEF region that occurs within ~5 μm of the anode [62,84].

CHAPTER 5

CONCLUSION

The main goal of this dissertation involved the study of carrier dynamics in GaAs-based photoconductive THz sources using Monte Carlo techniques to optimize the emitted THz transients. This goal was achieved by the development of a self-consistent Monte Carlo-Poisson solver for the spatio-temporal carrier transport properties. We also obtained self-consistently the screening contributions to the THz radiation associated with the Coulomb and radiation fields by incorporating the three-dimensional Maxwell equations into the solver. In addition, the enhancement of THz emission by a large trap-enhance fields (TEF) near the anode in semi-insulating (SI) photoconductors was investigated.

In this dissertation, we have detailed the theoretical framework necessary for implementing the acoustic-phonon, ionized-impurity, intervalley, carrier-carrier (electron-electron, electron-hole, and hole-hole), and screened carrier-phonon scattering in the Monte Carlo method using the three nonparabolic valleys Γ, L, and X within the conduction band and the warped heavy- and light-hole valence bands. Furthermore, we have presented the basic ingredients, numerical algorithms and device models in Monte Carlo-Poisson solver.

Our focus has been on the interplay of the carrier dynamics and screening, which is the main factor underlying the saturation of the THz radiation power and how to choose the optical excitation conditions for optimizing THz generation. We have presented the first systematic exploration of the effects of varying the excitation

conditions to extract the maximum THz spectral power density in the frequency range of interest fully considering the effect of spatial carrier distributions and the presence of the subsidiary valleys in the band structure at the same time. While some empirical evidence of such an effect was hinted at Refs. 85 and 86, no systematic study has been carried out to date. Thus the contributions of this dissertation can be summarized as follows.

We have shown that the transport properties of the photoexcited carriers in photoconductive THz sources depend markedly on the initial spatial distribution of those carriers, and that by judicious choice of the optical excitation spot shape, one can obtain an enhancement of the THz peak power by employing an elliptical excitation-spot with its major axis parallel to the direction of the bias field since for a given photoexcited carrier density, this excitation-spot shape suppresses saturation at high optical fluence due to space-charge screening. The THz radiation in the far field is proportional to the time derivative of the current density, i.e. the emitted THz transient depends crucially on the carrier drift velocity. Since the carrier dynamics are the source of the THz radiation and are strongly affected by the ensuing space-charge screening, the effects of spatial patterned excitation can be used in order to obtain the temporal velocity profile to produce the desired THz transient.

We have distinguish the screening contributions due to the Coulomb and radiation parts of the electromagnetic field acting back on the carrier dynamics within the first picosecond subsequent to the ultrafast photogeneration of electron-hole pairs in photoconductive THz sources. We have identified which of the Coulomb and radiation fields is dominant with varying excitation aperture sizes, and have found that these screening effects may be the main factor underlying radiation power saturation. We have

found for a range of reasonable excitation levels an excitation spot diameter of ~100 μm (full width at half maximum) as the crossover point beyond which radiation effects dominate screening. In addition, we have predicted an enhancement of the optical-to-THz conversion efficiency with increasing excitation-aperture for a given optical excitation power compared with what would be expected based on screening.

We have elucidated in detail the key mechanisms responsible for the trap-enhanced fields (TEF) near the anode of SI photoconductors using a self-consistent Poisson solver where the free-carrier densities and impurity ionization are set by the local value of the Fermi potential to include partial ionization of the defect centers. Moreover, when the biased photoconductor in which the TEF is established is illuminated by a femtosecond optical pulse, we have considered the occupation-factor effects depending on both electron and hole densities together with the excess carrier densities due to the photoexcitation. We have also accounted for the transport of these photocarriers. From the results of the simulations, we have shown the dramatic enhancement of the THz transient response with photoexcitation in the TEF region near the anode of a SI-GaAs photoconductive THz source. In addition, we have obtained the contributions of the Coulomb and radiation screening to the TEF, and have found that both these screening fields decrease as the excitation aperture increases. Thus, for a given optical excitation power, we predict that enhancement of THz radiation power can be obtained using a maximally broadened excitation aperture in the TEF area elongated along the anode due to the reduction in the Coulomb and radiation screening of the TEF.

APPENDIX A

COORDINATE TRANSFORMATION

In a full three dimensional simulation in **k**-space, the polar angle θ between **k**′ and **k**, and the magnitude of **k** are determined from momentum conservation, and energy conservation, respectively. Then, the final state with respect to the fixed direction, where we assume k_x is parallel to the direction of the bias field **E**, is obtained by the following coordinate transformation [39]

$$k_x' = k'(\cos\theta\cos\alpha_1 - \sin\theta\cos\varphi\sin\beta\cos\alpha_3 + \sin\theta\sin\varphi\cos\beta),$$

$$k_y' = k'(\cos\theta\cos\alpha_2 - \sin\theta\cos\varphi\cos\beta\cos\alpha_3 - \sin\theta\sin\varphi\sin\beta),$$

$$k_z' = k'(\cos\theta\cos\alpha_3 + \sin\theta\cos\varphi\sin\alpha_3), \qquad \text{(A. 1)}$$

where $\alpha_1=\cos^{-1}(k_x/k)$, $\alpha_2=\cos^{-1}(k_y/k)$, $\alpha_3=\cos^{-1}(k_z/k)$, and $\beta=\tan^{-1}(k_x/k_y)$ as shown in Figure A.1. The azimuthal angle $\varphi = 2\pi r$, where r is random number between 0 and 1.

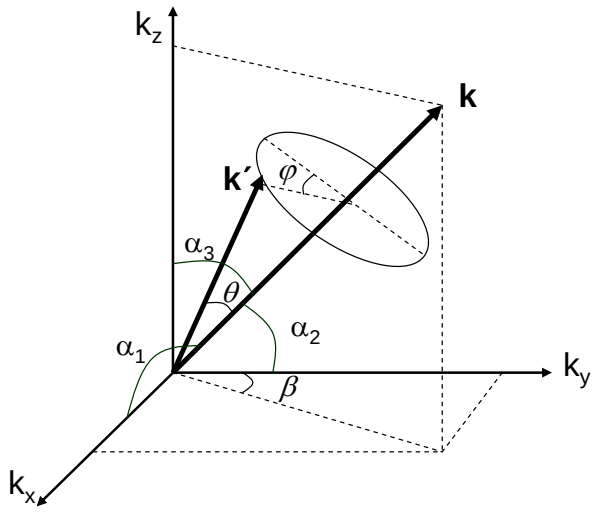

Figure A. 1 The geometry for the determination of the state after scattering for anisotropic processes.

REFERENCES

[1] D. R. Grischkowsky, "Optoelectronic characterization of transmission lines and waveguides by terahertz time-domain spectroscopy," *IEEE J. Sel. Top. Quantum Electron.*, vol. 6, pp. 1122–1135, 2000.

[2] M. Nagel, C. Meyer, H.-M. Heiliger, T. Dekorsy, H. Kurz, R. Hey, and K. Ploog, "Optical second-harmonic probe for ultra-high frequency on-chip interconnects with benzocyclobutene," *Appl. Phys. Lett.,* vol. 72, pp. 1018-1020, 1998.

[3] B. B. Hu and M. C. Nuss, "Imaging with terahertz waves,' *Opt. Lett*., vol. 20, pp. 1716-1718, 1995.

[4] D. M. Mittleman, M. Gupta, R. Neelamani, R. G. Baraniuk, J. V. Rudd, and M. Koch, "Recent advances in terahertz imaging," *Appl. Phys.,* vol. B68, pp. 1085-1094, 1999.

[5] R. H. Woodward, B. Cole, V. P. Wallace, D. D. Arnone, E. H. Linfield, and M. Pepper, "Terahertz pulse imaging in reflection geometry of human skin cander tissue," *Phys. Med., Biol.* vol. 47, pp. 3853-3863, 2002.

[6] M. Nagel, P. Haring Bolivar, M. Bruchersifer, and H. Kurz, "Integrated THz technology for label-free genetic diagnostics," *Appl. Phys. Lett.,* vol. 80, pp. 154-156, 2002.

[7] J. Shan, A. Nahata, and T. F. Heinz, "Terahertz time-domain spectroscopy based on nonlinear optics," *J. Nonlinear Opt. Phys. Mater.,* vol. 11, pp. 31-48, 2002.

[8] Q. Wu and X.-C. Zhang, "Ultrafast electro-optic field sensors," *Appl. Phys. Lett*., vol. 68, pp. 1604–1606, 1996.

[9] P. C. M. Planken and H. J. Bakker, "Towards time-resolve THz imaging," *Appl. Phys. A*, vol. 78, pp. 465–469, 2004.

[10] Y. C. Shen, P. C. Upadhyar, E. H. Linfield, H. E. Beere, and A. G. Davies, "Ultrabroadband terahertz radiation from low-temperature-grown GaAs photoconductive emitters," *Appl. Phys. Lett.,* vol. 83, pp. 3177-3179, 2003.

[11] P. R. Smith, D. H. Auston, and M. C. Nuss, "Subpicosecond photoconducting dipole antennas," *IEEE J. Quantum Electron.,* vol. 24, pp. 255-260, 1988.

[12] D. H. Auston, "Picosecond optoelectronic switching and gating in silicon," *Appl. Phys. Lett.,* vol. 26, pp. 101-103, 1975.

[13] G. Mourou, C. V. Stancampiano, A. Antonetti, and A. Orszag, "Picosecond microwave pulses generated with a subpicosecond laser-driven semiconductor switch," *Appl. Phys. Lett.*, vol. 39, pp. 295-296, 1981.

[14] X.-C. Zhang, B. B. Hu, J. T. Darrow, and D. H. Auston, "Generation of femtosecond electromagnetic pulses from semiconductor surfaces," *Appl. Phys. Lett.*, vol. 56, pp. 1011-1013, 1990.

[15] J. T. Darrow, X.-C. Zhang, D. H. Auston, and J. D. Morse, "Saturation properties of large-aperture photoconducting antennas," *IEEE J. Quantum Electron.*, vol. 28, pp. 1607–1616, 1992.

[16] Y. Cai, I. Brener, J. Lopata, J. Wynn, L. Pfeiffer, and J. Federici, "Design and performance of singular electric field terahertz photoconducting antennas," *Appl. Phys. Lett*., vol. 71, pp. 2076–2078, 1997.

[17] G. Zhao, R. N. Schouten, N. van der Valk, W. Th. Wenckebach, and P. C. M. Planken, "Design and performance of a THz emission and detection setup based on a semi-insulating GaAs emitter," *Rev. Sci. Instrum.*, vol. 73, pp. 1715–1719, 2002.

[18] Dae Sin Kim and D. S. Citrin, "The effects of spatially patterned excitation in THz generation from photoconductive sources," *Optical Terahertz Science and Technology* (OTST, Orando, Florida, USA), March, 2005.

[19] G. Rodriguez and A. J. Taylor, "Screening of the bias field in terahertz generation from photoconductors," *Opt. Lett.*, vol. 21, pp. 1046–1048, 1996.

[20] J. E. Pederson, V. G. Lyssenko, J. M. Hvam, P. U. Jepsen, S. R. Keiding, C. B. Sorensen, and P. E. Lindelof, "Ultrafast local field dynamics in photoconductibe THz antennas," *Appl. Phys. Lett.,* vol. 62, pp. 1265-1267, 1993.

[21] W. Sha, J.-K. Rhee, T. B. Norris, and W. J. Schaff, "Transient carrier and field dynamics in quantum-well parallel transport: From the ballistic to the quasiequilibrium regim," *IEEE J. Quantum Electron.,* vol. 28, pp. 2445-2455, 1992.

[22] Dae Sin Kim and D. S. Citrin, "Coulomb and radiation screening in photoconductive terahertz sources," *Appl. Phys. Lett*., vol. 88, pp. 16117, 2006.

[23] S.-G. Park, A. M. Weiner, M. R. Melloch, C. W. Siders, J. L. W. Siders and A. J. Taylor, "High-power narrow-band terahertz generation using large-aperture photoconductors," *IEEE J. Quantum Electron.,* vol. 35, pp. 1257-1268, 1999.

[24] N. M. Froberg, B. B. Hu, X.-C. Zhang, and D. H. Auston, "Terahertz radiation from a photoconducting antenna," *IEEE J. Quantum Electron.,* vol. 28, pp. 2291-2301, 1992.

[25] J. F. Holzman, F. E. Vermeulen, and A. Y. Elezzabi, "Frozen wave generation of bandwidth-tunable two-cycle THz radiation," *J. Opt. Soc. Am. B,* vol. 17, pp. 1457-1463, 2000.

[26] D. Krokel, D. Grischkowsky, and M. B. Ketchen, "Subpicosecond electrical pulse generation using photoconductive switches with long carrier lifetimes," *Appl. Phys. Lett.,* vol. 54, pp. 1046-1048, 1989.

[27] N. Katzenellenbogen and D. Grischkowsky, "Efficient generation of 380fs pulse of THz radiation by ultrafast laser pulse excitation of a biased metal-semiconductor interface," *Appl. Phys. Lett*., vol. 58, pp. 222-224, 1991.

[28] Y. Liu, S.-G. Park, and A. M. Weiner, "Enhancement of narrow-band terahertz radiation from photoconducting antennas by optical pulse shaping," *Opt. Lett.,* vol. 21, pp. 1762-1764, 1996.

[29] P. K. Benicewicz, J. P. Roberts, and A. J. Taylor, "Scaling of terahertz radiation from large-aperture biased photoconductors," *J. Opt. Soc. Am. B,* vol. 11, pp.2533-2546, 1994.

[30] G. Rodriguez, S. R. Caceres, and A. J. Taylor, "Modeling of terahertz radiation from biased photoconductors: transient velocity effects," *Opt. Lett.,* vol. 19, pp. 1994-1996, 1994.

[31] T. Dekorsy, T. Pfeifer, W. Kutt, and H. Kurz, "Subpicosecond carrier transport in GaAs surface-space-charge fields," *Phys. Rev. B,* vol. 47, pp. 3842-3849, 1993.

[32] P. U. Jepsen, F. H. Jacobsen, and S. R. Keiding, "Generation and detection of terahertz pulses from biased semiconductor antennas," *J. Opt. Soc. Am. B,* vol. 13, pp. 2424-2436, 1996.

[33] J. G. Ruch, "Electron dynamics in short channel field effect transistors," *IEEE Trans. Electron Devices*, vol. ED-19, pp. 652-654, 1972.

[34] M. S. Shur and L. F. Eastman, "Ballistic transport in semiconductors at low temperature for low-power high speed logic," *IEEE Trans. Electron Devices*, vol. ED-26, pp. 1677-1683, 1983.

[35] M. C. Nuss, D. H. Auston, and F. Capasso, "Direct subpicosecond measurement of carrier mobility of photoexcited electrons in Gallium Arsenide," *Phys. Rev. Lett.*, vol. 58, pp. 2355-2358, 1987.

[36] C. V. Shank, R. L. Fork, B. I. Greene, F. K. Reinhart, and R. A. Logan, "Picosecond nonequilibrium carrier transport in GaAs," *Appl. Phys. Lett.*, vol. 38, pp. 104-105, 1981.

[37] D. K. Ferry, *Semiconductors*, New York: Macmillan, 1991.

[38] K. F. Brennan, The physics of semiconductors with applications to optoelectronic devices, Cambridge: Cambridge University Press, 1999.

[39] C. Jacoboni and L. Reggiani, "The Monte Carlo method for the solution of charge transport in semiconductors with applications to covalent materials," *Rev. Mod. Phys.,* vol. 55, pp. 645-705, 1983.

[40] W. Fawcett, A. D. Boardman, and S. Swain, "Monte Carlo determination of electron transport properties in Gallium Arsenide," *J. Phys. Chem. Solids,* vol. 31, pp. 1963-1990, 1970.

[41] N. Nintunze, and M. A. Osman, "Hole drift velocity in the warped band model of GaAs," *Semicond. Sci. Technol.,* vol. 10, pp. 11-17, 1995.

[42] M. T. Portella, J.-Y. Bigot, R. W. Schoenlein, J. E. Cunningham, and C. B. Shank, "k-space carrier dynamics in GaAs," *Appl. Phys. Lett.,* vol. 60, pp. 2123-2125, 1992.

[43] T. Brudevoll, T. A. Fjeldly, J. Baek, and M. S. Shur, "Scattering rates for holes near the valence-band edge in semiconductors," *J. Appl. Phys.,* vol. 67, pp. 7373-7382, 1990.

[44] J. D. Wiley, " Polar mobility of holes in III-V compounds," *Phys. Rev.*, vol. B4, pp.2485-2493, 1971.

[45] J. G. Rush and W. Fawcett, "Temperature dependence of the transport properties of Gallium Arsenide determined by a Monte Carlo Method," *J. Appl. Phys.,* vol. 41, pp. 3843–3849, 1970.

[46] M. A. Osman and D. K. Ferry, "Monte Carlo investigation of the electron-hole interaction effects on the ultrafast relaxation of hot photoexcited carriers in GaAs," *Phys. Rev. B*, vol. 36, pp. 6018–6032, 1987.

[47] C. K. Birdsall and D. Fuss, "Clouds-in-Clouds, Clouds-in-Cells physics for many-body plasma simulation," *J. Comput. Phys*., vol. 3, pp. 494-511, 1969.

[48] M. Bieler, G. Hein, K. Pierz, and U. Siengner, "Spatial pattern formation of optically excited carriers in photoconductive switches," *Appl. Phys. Lett.*, vol. 77, pp. 1002–1004, 2000.

[49] M. Bieler, G. Hein, K. Pierz, U. Siegner, M. Koch, M. W. Feise and D. S. Citrin, "Spatial pattern formation of optically excited carriers in photoconductive THz antennas," *Proceedings of the THz 2000 Conference*, Darmstadt Germany, 2000.

[50] M. Koch, M. Bieler, G. Hein, K. Pirez, and U. Siegner, "Photoconductive switches: The role of spatial effects in carrier dynamics," *Phys. Stat. Sol. B,* vol. 221, pp. 429-433, 2000.

[51] M. W. Feise, D. S. Citrin, M. Bieler, M. Koch, G. Hein, K. Pierz U. Siegner, and M. Koch, "Spatially resolved current dynamics in photoconductive switches," *Optics and Photonics Series(TOPS),* vol. 49, pp. 134-138, 2001.

[52] J. Lloyd-Hughes, E. Castro-Camus, M. D. Fraser, C. Jagadish, and M. B. Johnston, "Carrier dynamics in ion-implanted GaAs studied by simulation and observation of terahertz emission," *Phys. Rev. B,* vol. 70, pp.235330, 2004.

[53] M. B. Johnston, D. M. Whittaker, A. Corchia, A. G. Davies, and E. H. Linfield, "Simulation of terahertz generation at semiconductor surfaces," *Phys. Rev. B,* vol. 65, pp. 165301, 2002.

[54] V. L. Malevich, "Monte Carlo simulation of THz-pulse generation from semiconductor surface," *Semicondi. Sci. Technol*., vol. 17, pp. 551-556, 2002.

[55] G. S. Smith, *An Introduction to Classical Electromagnetic Radiation*. Cambridge, U.K.: Cambridge University Press, 1990.

[56] S. E. Ralph and D. Grischkowsky, "Trap-enhanced electric fields in semi-insulators: The role of electrical and optical carrier injection," *Appl. Phys. Lett.*, vol. 59, pp. 1972–1974, 1991.

[57] Dae Sin Kim and D. S. Citrin, "The transport of photoexcited electrons in photoconductive THz sources with spatially patterned excitation," *Conference on Lasers and Electro-Optics* (CLEO, Baltimore, Maryland, USA), May, 2005.

[58] Dae Sin Kim and D. S. Citrin, "Enhancement of terahertz radiation from photoconductors by elliptically focused excitation," *Appl. Phys. Lett.*, vol. 87, pp. 61108, 2005.

[59] J. D. Jackson, *Classical Electrodynamics,* 3rd ed., New York: Wiley, 1999.

[60] G. S. Smith, "Teaching antenna radiation from a time-domain perspective," *Am. J. Phys.,* vol. 69, pp. 288-300, 2000.

[61] J. T. Darrow, X. -C. Zhang, and D. H. Auston, "Power scaling of larg-aperture photoconducting antennas," *Appl. Phys. Lett.*, vol. 58, pp. 25-27, 1991.

[62] J. H. Kim, A. Polley, and S. E. Ralph, "Efficient photoconductive terahertz source using line excitation," *Opt. Lett.*, vol. 30, pp. 2490–2492, 2005.

[63] B. B. Hu, E. A. De Souza, W. H. Knox, J. E. Cunningham, and M. C. Nuss, "Identifying the distinct phases of carrier transport in semiconductors with 10 fs resolution," *Phys. Rev. Lett.,* vol. 74, pp. 1689-1692, 1995.

[64] W. E. Baylis, *Electrodynamics A Modern Geometric Approach.* Boston, MA: Birkhauser, 1999.

[65] A. R. Janah, T. Padmanabhan, and T. P. Singh, "On Feynman's formula for the electromagnetic field of an arbitrarily moving charge," *Am. J. Phys.*, vol. 56, pp. 1036-1038, 1988.

[66] J. G. Proakis, D. G. Manolakis, *Digital Signal Processing Principles, Algorithms, and Applications*, 3rd ed., New Jersey: Prentice-Hall, 1996.

[67] U. D. Keil and D. R. Dykaar, "Ultrafast pulse generation in photoconductive switches," *IEEE J. Quantum Electron.*, vol. 32, pp. 1664–1671, 1996.

[68] P. K. Benicewicz, J. P. Roberts, and A. J. Taylor, "Scaling of terahertz radiation from large-aperture biased photoconductors," *J. Opt. Soc. Am. B*, vol. 11, pp. 2533-2546, 1994.

[69] N. G. Ainslie, S. E. Blum, and J. F. Woods, "On the preparation of high purity gallium arsenide," J. Appl. Phys., vol. 33, pp. 2391–2393, 1961.

[70] G. R. Cronin and R. W. Haisty, "The preparation of semi-insulating gallium arsenide by chromium doping," *J. Electrochem. Soc.*, vol. 111, pp. 874–877, 1964.

[71] J. B. Mullin, R. J. Heritage, C. H. Holliday, and B. W. Straughan, "Liquid encapsulation crystal pulling at high pressures," *J. Cryst. Growth*, vol. 3-4, pp. 281–285, 1968.

[72] C. H. Gooch, C. Hilsum, and B. R. Holeman, "Properties of semi-insulating GaAs," *J. Appl. Phys.*, vol. 32, pp. 2069–2073, 1961.

[73] G. M. Martin, J. P. Farges, G. Jacob, J. P. Hallais, and G. Poiblaud, "Compensation mechanisms in GaAs," *J. Appl. Phys.*, vol. 64, pp. R65–R91, 1988.

[74] J. C. Bourgoin, H. J. von Bardeleben, and D. Stievenard, "Native defects in gallium arsenide," *J. Appl. Phys.*, vol. 51, pp. 2840–2852, 1980.

[75] D. S. McGregor, R. A. Rojeski, G. F. Knoll, F. L. Terry, Jr., J. East, and Y. Eisen, "Evidence for field enhanced electron capture by EL2 centers in semi-insulating GaAs and the effect on GaAs radiation detectors," *J. Appl. Phys.*, vol. 75, pp. 7910–7915, 1994.

[76] L. L. Bonilla, P. J. Hernando, and M. Kindelan, "Determination of EL2 capture and emission coefficients in semi-insulating n-GaAs," *Appl. Phys. Lett*., vol. 74, pp. 988–990, 1999.

[77] K. F. Brennan, *The Physics of Semiconductors with Applications to Optoelectronic Devices*. Cambridge, U.K.: Cambridge University Press, 1999.

[78] R. B. Darling, "Electrostatic and Current transport properties of n^+/semi-insulating GaAs junctions," *J. Appl. Phys.*, vol. 74, pp. 4571–4589, 1993.

[79] T. P. Chen, Y. C. Liu, S. Fung, and C. D. Beling, "Interfacial Fermi level and surface band bending in Ni/semi-insulating GaAs Contact," *J. Appl. Phys.*, vol. 78, pp. 4796–4798, 1995.

[80] D. C. Look, *Electrical Characterization of GaAs Materials and Devices.* New York: Wiley, 1989.

[81] J. P. McKelvey, *Solid State and Semiconductor Physics*. Malabar, FL: R. E. Krieger publishing co., 1984.

[82] H. Hjelmgren, "Numerical modeling of hot electrons in n-GaAs Schottky-barrier diodes," *IEEE Trans. Electron Devices*, vol. 37, pp. 1228–1234, 1990.

[83] S. M. Sze, *Physics of Semiconductor Devices*, 2nd ed. New York: Wiley, 1981.

[84] Dae Sin Kim and D. S. Citrin, "Efficient THz generation using trap-enhanced fields in semi-insulating photoconductors by spatially broadened excitation," *IEEE J. Quantum Electron.*, 2006 (submitted).

[85] M. T. Reitien, D. Grischkowsky, and R. A. Cheville, "Properties of surface waves determined via bistatic terahertz impulse ranging," *Appl. Phys. Lett.,* vol. 78, pp. 1146-1148, 2001.

[86] S. R. Andrews, A. Armitage, P. G. Huggard, and A. Hussain, "Optimization of photoconducting receivers for THz spectroscopy," *Phys. Med. Biol.,* vol. 47, pp. 3705-3710, 2002.